Contributions to the study of two-dimensional spatial coherence as part of the development of a low-frequency synthetic aperture sonar

Fabien Novella

COLLEGES BRETAGNE LOIRE — SCIENCES POUR L'INGENIEUR ET LE NUMERIQUE

ENSTA BRETAGNE

THESE DE DOCTORAT DE

L'ECOLE NATIONALE SUPERIEURE
DE TECHNIQUES AVANCEES BRETAGNE

ECOLE DOCTORALE N° 648
Sciences pour l'Ingénieur et le Numérique
Spécialité : *Signal Image Vision*

Par

Fabien NOVELLA

Contributions to the study of two-dimensional spatial coherence as part of the development of a low-frequency synthetic aperture sonar.

Thèse présentée et soutenue à ENSTA Bretagne (Brest), le 24 juin 2024
Unité de recherche : Lab-STICC UMR 6285
Thèse N° :

Rapporteurs avant soutenance :

Cornel IOANA	Maître de Conférences HDR, Grenoble INP
Yvan PETILLOT	Professeur, Université Heriot-Watt, Edimbourg (UK)

Composition du Jury :

Président :	Ali KHENCHAF	Professeur des Universités, ENSTA Bretagne)
Examinateurs :	Vincent MYERS	Senior Scientist, DRDC, Halifax (NS, Canada)
	Michel LEGRIS	Enseignant Chercheur, ENSTA Bretagne
	Yan PAILHAS	Senior Scientist, NATO STO CMRE, La Spezia (Italie)
Dir. de thèse :	Isabelle QUIDU	Maître de Conférences HDR, ENSTA Bretagne

Invité(s)

Gilles LE CHENADEC	Enseignant Chercheur, ENSTA Bretagne
Alain HETET	Ingénieur en Chef des Etudes et Techniques de l'Armement, DGA

Contents

List of Figures

List of Tables

Chapter 1

Introduction and thesis overview

Sonars, an acronym for "SOund Navigation And Ranging", are devices used in many fields, including maritime navigation, military defence, scientific research, underwater mapping, natural resources research and environmental monitoring. The importance of sonar lies in its ability to operate in environments where electromagnetic waves propagation is severely limited, including in the visual spectrum, such as the ocean depths and murky waters. By using sound waves that propagate through water, sonars can provide valuable information about the topography of the seabed, the presence of underwater obstacles, the location of moving targets such as ships or submarines, and the detection of marine ecosystems and natural resources.

Sonar performance and the notion of coherence of the acoustic wave they use are closely linked. The coherence of a wave refers to the ability of this wave to maintain a constant phase relationship over a certain distance in space. Coherence is therefore closely linked to the ability of signals acquired at different points in a wave field to interfere constructively or destructively with each other. If signals acquired at positions far apart from each other retain their ability to interfere constructively and destructively with each other, then the wavefield is said to have a long coherence. In the sonar field there is a correspondence between the distance in the insonification direction (range direction) and time. Therefore, 3D coherence is often qualified as spatio-temporal coherence as it deals with both:

- **temporal coherence**, i.e. correlation of a wave field with a delayed version of itself sensed at the same point of space;
- **spatial coherence**, i.e. correlation of a wave field sensed at two positions of space but without time delay between them.

In the context of imaging sonars, to obtain high spatial resolution in a synthetic

aperture sonar (SAS) image, it is necessary for the acoustic waves to retain their spatial coherence on the alongtrack direction and over the synthetic range. If the waves lose their spatial coherence, the spatial resolution as well as the contrast of the final image will deteriorate. Moreover in order to produced well focused SAS image, it is necessary to estimate accurately the motion of the sonar. To do so Displaced Phase Center (DPC) methods exploit spatio-temporal coherence of the backscattered field. For interferometric synthetic aperture, high spatial coherence on the vertical direction is required. Indeed interferometry is a technique that relies on interference between signals sensed on two vertically separated antenna in order to extract information about the geometry of acquisition and in particular the determination of the direction of arrival (DoA) of the sonar wave required to estimate bathymetry, for example. Interferometry requires waves to interfere coherently over a certain distance in vertical direction. If the waves lose their spatial coherence over this distance, it becomes difficult or even impossible to obtain accurate information from the interference.

Spatio-temporal coherence is therefore a central concept in sonar, affecting spatial resolution, DoA estimation by interferometric methods, signal processing such as DPC, and the performance of advanced techniques such as aperture synthesis. The hardware of the sonar system, signal processing parameters, changing environmental conditions and external disturbances all affect the spatio-temporal coherence of the backscattered acoustic field exploited by sonars. Understanding these effects and maintaining high spatio-temporal coherence is therefore essential to define and exploit the full potential of sonar systems in a range of marine applications.

The purpose of this dissertation is to develop a model for spatial coherence of an acoustic field scattered from a seafloor in oblique incidence. To do so, existing models developed for the down-looking have been extended to be compatible with the side-looking geometry. This model takes account a range of processes: transducer apertures, propagation losses, seafloor scattering function, and temporal windowing. One of the major assumptions of this spatial coherence model is that it is based on signals received at two points in space but without any delay in relation to each other. In a down looking geometry, this is equivalent to being in a far field with sensors located in a plane parallel to the seafloor. On the other hand, side-looking acquisition geometry does not allow us to comply with this assumption and geometric decorrelations (mismatch footprint and stretching) occur. These phenomena are not taken into account by the modelling introduced here, which is why numerical modelling of the signals is proposed.

The document is divided into four chapters. In chapter 2, the study is placed in the context of mine countermeasures, for which low-frequency synthetic aperture sonars are currently being developed. Here, aperture synthesis, already widely used for high-frequency sonars (typically between 150 kHz and 300 kHz), is supplemented by the use of lower frequency signals (typically around 15kHz). The use of this frequency band should make it possible to detect buried objects and classify them by analysing the structure of the target's elastic response. In chapter two the notion of coherence is introduced. Then, the Van Cittert Zernike (VCZ) theorem is presented. This theorem, developed in the field of optics relates spatial coherence to the energy distribution of an incoherent source. This theorem was subsequently extended to acoustics, a field in which sources (transmitters) are coherent. This extension proposes to focus on the acoustic field reflected by an incoherent scattering medium, a classic situation in acoustics. This section also covers applications of spatial coherence in sonar field, and in particular micronavigation SAS. In chapter three, an analytical model of spatial coherence is proposed. This analytical model is divided into two acquisition geometries. The first geometry is vertical (down looking). A discussion is conducted on the assumptions under which the VCZ theorem in its 'optical' or 'acoustic' formulation is verified. This modelling is then extended to the oblique geometry (side looking). In chapter three, numerical study of coherence is proposed. First, the analytical model is solved numerically in order to extend the analysis of the previous chapter to different environmental conditions (influence of the nature of the seafloor), different acquisition acquisition devices (different apertures) and different time windows over which coherence is estimated. However, in side looking geometry, coherence remains highly dependent on geometric decorrelations (stretching and mismatch footprint in particular) induced by the observation geometry. In order to introduce these phenomena into the study, the signals were modelled numerically using the point-based scattering model. Using the simulated signals simulated in this way, coherences are estimated before and after compensation for geometric geometric phenomena.

The following publications were directly supported by this research:

- Fabien Novella, Yan Pailhas, Isabelle Quidu, Gilles Le Chenadec. (2020). Low Frequency SAS: Spatial Coherence Study. Proceedings of Meetings on Acoustics. 40. 070016. 10.1121/2.0001320.

- Fabien Novella, Yan Pailhas, Gilles Le Chenadec, Isabelle Quidu, Michel Legris. (2021) Low Frequency SAS: Influence of multipaths on Spatial Coherence. 6th Underwater Acoustics Conference & Exhibition, Virtual meeting, United States.

pp.070032, 10.1121/2.0001503. hal-03519906

Chapter 2

Context and fundamental principles

In this chapter, we would like to place the study of spatial coherence carried out in this document in the context of the use of synthetic aperture sonars and, more generally, their use in mine countermeasures. To do so, in a section 2.1, generalities about imaging sonar are introduced. Unlike conventional sidescan sonars, whose frequency depends mainly on the range and resolution required, SAS systems allow to produce images of the seabed with range-independent and frequency-independent resolution. Operating principles and challengsr of SAS processing are presented in section 2.2. Then in section 2.3, the principles and challenges of mine warfare are introduced. High frequency SAS systems are increasingly used in the mine countermeasure domain as they can produce images of the seabed with very high contrasts between target echoes, projected shadows and the surrounding seabed. These image characteristics are used by mine countermeasures operators or by automatic recognition algorithms to distinguish a threat (a mine, for example) from a rock on the seabed. However, these HF SAS systems suffer from two major limitations: firstly, they are completely ineffective on buried objects, and secondly, their performance drops when the objects are partially buried or when the seabed is studded with rocks of a size and shape compatible with a mine (cluttered environment). To deal with this issue low-frequency SAS systems are currently being developed. Section 2.3 includes a review on buried detection methods.

2.1 Sonar imaging generalities

The marine environment is a medium in which electromagnetic waves propagate rather poorly. Indeed, even in very good conditions, it is difficult to see more than 30m underwater in natural light. On the contrary, acoustic waves are much less absorbed

by seawater and propagate over much greater distances. This is why acoustics has a wide range of applications in the underwater field, such as communication, speed measurement, distance measurement, or imaging of the seabed and objects [Lurton, 2002]. For these last two applications, active sonars are widely used tools. In general, whether for bathymetric or imaging sonars, the operating principle of active sonars is the same:

- The system emits an acoustic signal of finite duration in a given direction;
- The acoustic wave propagates at a given speed and interacts with the seafloor;
- A part of the reflected signal is directed to a receiving antenna which records, amplifies, and processes this part of the backscattered signal according to the intended application;
- Knowing the speed of sound in water (measured, for example, by an external sensor) it is possible to calculate the distance from the measured time of flight of the signal. Besides, the strength of the signal can be used to characterize the seafloor or a target.

Depending on the application, several criteria are used to qualify sonar performance. Generally speaking, in an imaging context, one seeks to work (detect, for example) on small contacts at great distances to maximise the coverage rate and thus minimize the time spent in operation, which is generally very expensive. In order to quantify performances, two metrics are of particular interest: resolution and maximum operating range. These two points are developed below.

2.1.1 Resolution

Let's first introduce the notion of resolution. Resolution is the ability of a system to differentiate between two echoes that are close to each other. Sonar images are generally bi-dimensional and so, two types of resolutions are to be differentiated: the range resolution (related to across-track resolution) and the along-track resolution.

Range Resolution

The range resolution reflects the ability of a sonar system to discriminate between two echoes in the direction of propagation. This point is illustrated in Figure 2.1. In this figure, the range resolution is noted ρ_R. Distance between points C and B is lower than the range resolution ρ_R. Thus, they can not be discriminated. On the

contrary, the distance between points B and A is larger than the range resolution ρ_R so they can be discriminated.

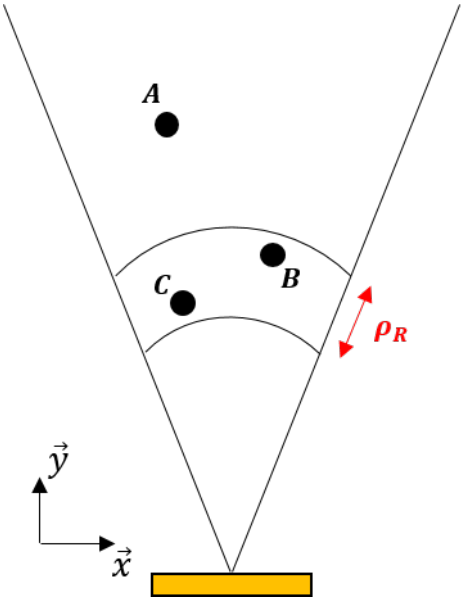

Figure 2.1: Illustration of the range resolution. Distance between points C and B is lower than range resolution ρ_R; thus, they can not be discriminated. On the contrary, the distance between points B and A is larger than the range resolution, so they can be discriminated.

This resolution depends on the emitted signal and the associated processings. In the case of the emission of a chirp, the emitted signal can be written as:

$$s_e(t) = \Pi_T(t) e^{j(2\pi f_0 t + \pi \frac{B}{T} t^2)} \tag{2.1}$$

where $\Pi_T(t)$ is the T length rectangular function, B the bandwith and f_0 the central frequency. After reflection by a point target located at a distance $d_0 = \frac{ct_0}{2}$, the received signal s_0 corresponds to the transmitted signal delayed by a time t_0 and attenuated by a factor A:

$$s_{t_0}(t) = A\Pi_T(t - t_0) e^{j(2\pi f_0 (t-t_0) t + \pi \frac{B}{T} (t-t_0)^2)} \tag{2.2}$$

Pulse compression consists in an matched filtering, i.e., in correlating the transmission signal with the received signal. If we note $s_M(t)$ the signal after pulse compression we have:

$$s_M(t) = \int_{-\infty}^{+\infty} s_e^*(\tau) s_0(t + \tau) d\tau \tag{2.3}$$

Before pulse compression, the signal envelope of s_0 has a length T and, therefore, a distance resolution $\rho_r = \frac{cT}{2}$. After pulse compression, the envelope of the filtered signal s_M as a length of about $\frac{1}{B}$ and therefore a range resolution $\rho_r = \frac{c}{2B}$. Figure 2.2 illustrates this gain in resolution. Figure 2.2(a) shows the emitted chirp $s_e(t)$, and the one received after reflection on a punctual target at a distance $d_0 = \frac{ct_0}{2}$ with $t_0 = 75ms$ (no attenuation is considered here). Figure 2.2(b) shows the received signal after pulse compression $s_M(t)$. One can notice that the arrival time at $75ms$ is detectable. In Figure 2.2(c), a signal backscattered by two point targets located at distances d_1 and d_2 such that $d_1 = \frac{ct_1}{2}$ and $d_2 = \frac{ct_2}{2}$ with $t_1 = 75ms$ and $t_2 = 80ms$ is represented. It can be noted that on the raw signal, these two contributions are not discernible: the range resolution before pulse compression is not sufficient. The match-filtered signal is represented in Figure 2.2(d). The gain in resolution allows us to distinguish the two distinct echoes.

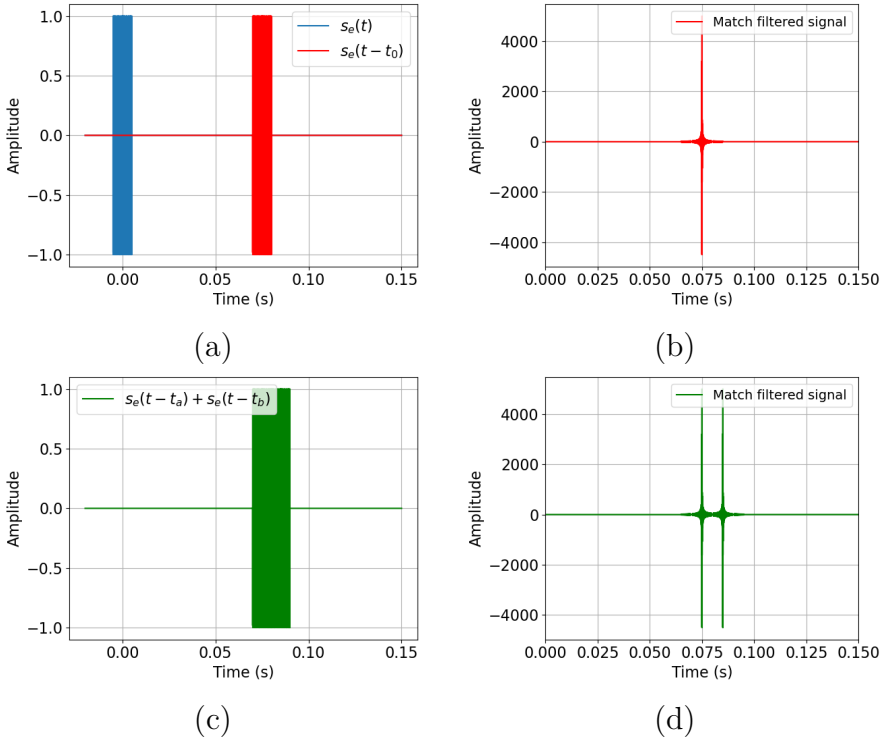

Figure 2.2: Illustration of the gain in resolution thanks to the pulse compression technique. (a) $s_e(t)$ is represented in blue and $s_e(t - t_0)$ with $t_0 = 75ms$ in red. (b) match-filtered received signal (c) $s_e(t)$ is represented in blue and $s_0(t) + s_1(t)$ with $t_0 = 75ms$ and $t_1 = 85ms$ in red. (d) match-filtered received signal

Along-track resolution

The along-track resolution reflects the ability of a system to discriminate between two echoes in the along-track direction. This resolution is related to the apertures of the transmitting and receiving antennas. The beam aperture of an antenna corresponds to an angle whose value is a function of the frequency of the emmited signal and the size (physical aperture) of the antenna. One can show the order of magnitude of the angular aperture of a linear antenna (noted θ_e) of length L at a frequency f_0 is given by [Lurton, 2002]:

$$\theta_e \approx 50.7\frac{\lambda}{L} = 50.7\frac{c}{Lf_0}$$

Projected at a given distance, this beam aperture has an extent called 'beam footprint', representing the antenna's discrimination capabilities defining the along-track resolution. Therefore, the minimum distance between two points so that they are discernible, is a function of the angle of aperture and the oblique distance at which are located these two points. That is illustrated in Figure 2.3. This figure represents a transmission beam with an angular aperture θ_e and a reception beam with an angular aperture θ_r. At range R_2, the beam footprint ρ_2 is larger than those at range R_1. To summarize, increasing frequency and antenna length allows to decrease beam footprint extent and so to improve along-track resolution. For a fixed frequency and antenna length, the extent of the beam footprint extent increases with the range and so the resolution deteriorates. Depending on the application, these parameters must be carefully selected in order to maximize efficiency and reduce employment constraints.

2.1.2 Maximum operating range

This parameter reflects the ability of the system to carry out the task for which it is intended at a given distance. We generally seek to maximize this distance to have the highest possible coverage rates and thus reduce mission time, which is generally very expensive. As we saw in section 2.1.1, we may be tempted to increase the frequency of the sonar to leverage interesting resolutions even at large distances. However, in practice, this is impossible because the propagation of a sound wave in water is attenuated, and this attenuation depends on the wave's frequency. As a first approximation, it is possible to assume that the absorption is proportional to the square of the wave's frequency, i.e., the higher the frequency of the acoustic wave, the more the energy of the latter will be absorbed. As a consequence, this tend to limit its maximum range. Depending on the missions for which they are intended, the frequencies and antenna lengths of the sonars are fixed. If the coverage is prioritized,

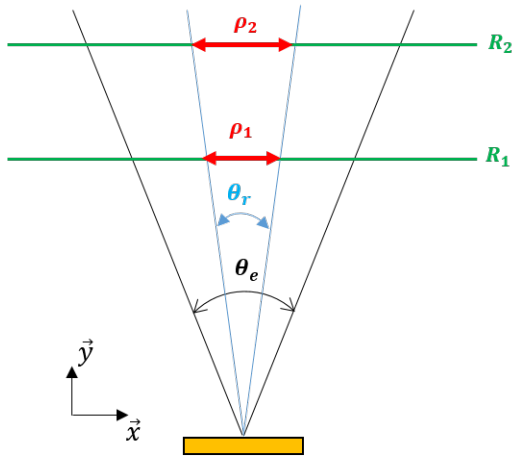

Figure 2.3: Illustration of the along-track resolution. θ_e corresponds to the angular aperture of the transmission beam, and θ_r corresponds to the angular aperture of the reception beam (oriented in a given direction)

it is necessary to decrease the frequency to increase the range at the expense of the resolution unless the antenna length is significantly increased. On the contrary, if the capacity to detect small structures is privileged, it will be necessary to increase the frequency, which will necessarily decrease the maximum reachable range and thus the coverage. This trade-off frequency/range/antenna size has led to the development of many imaging systems. The size and operating frequency of a system have been to be defined according to the application.

The principle of the synthetic antenna presented in the following paragraph makes it possible to circumvent this limitation by combining successive transmissions at different positions of the sonar so that the configuration is equivalent to that of a large virtual antenna. This processing enables us to obtain imaging systems whose resolution is theoretically independent of frequency and independent of range.

2.2 SAS principles

Synthetic aperture radar (SAR) was first developed in the 1950s. The first satellite equipped with a synthetic aperture radar was launched in 1978. The first studies in synthetic aperture sonar (SAS) date back to the 1970s with several patents [Walsh, 1969][Gilmour, 1978][Spiess and Anderson, 1983] and the first reference arti-

cles on the subject [Cutrona, 1975][Cutrona, 1977]. The complexity and instability of the marine environment made it difficult to develop these systems and the first operational prototypes appeared in the 90s.

The main goal of SAS processing is to improve the along-track resolution. For this purpose, a synthetic array is processed by coherently integrating signals sensed over multiple and successive pings. This integration makes it possible to take advantage of the displacement of the physical antenna to form a virtual antenna that is larger than the physical antenna The along-track resolution is so improved. This principle is illustrated in Figure 2.4.

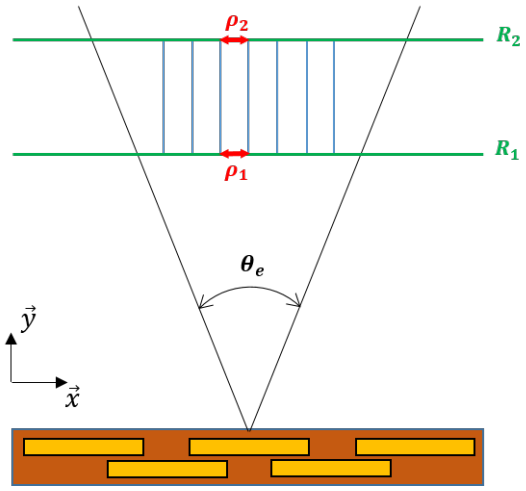

Figure 2.4: Illustration of the SAS along-track resolution. the combination of successive pings at different positions of the sonar allows to form a larger synthetic antenna allowing a constant resolution over the swath ($\rho_1 = \rho_2$).

It is legitimate to ask what is the maximum size of the synthetic antenna that can be formed. As illustrated in Figure 2.4, this maximum size is limited by the field of view of combined emission/reception directivity. If the receivers are assumed to be punctual, the angular aperture of combined transmission and reception is reduced to the angular aperture of the transmitter (θ_e on Figure 2.4), and so the smaller the transmit antenna, the larger its angular aperture and the larger the synthetic antenna that can be formed. As we will see in section 2.2.3, the theoretical resolution becomes range independent as the field of view increases with range and thus allow to form larger synthetic apertures. Similarly the theoretical resolution becomes frequency independent as the field of view increases while frequency decreases and thus allow to

form larger synthetic apertures [Hansen, 2011]. These two results (independence of resolution in frequency and range) have raised hopes of developing imaging sonars with a high coverage rate (long range by lowering the operating frequency) and small footprint (small physical antennas). However, as we will show in the rest of this section, the constraints of the underwater environment and the constraints on the use of SAS sonars have reduced these hopes.

In this section we first present the Phase Centre Approximation (PCA) which forms the basis of the SAS processing. We then present the difficulties induced by this processing in order to highlight the dimensioning characteristics of SAS sonars.

2.2.1 Phase center approximation

The displacement of the entire acquisition device (transmission and reception) required for aperture synthesis makes the acquisition geometry bistatic. The notion of phase center approximation (PCA) gives an equivalent monostatic configuration. Let's consider the case of a transmitter (Tx) and a receiver (R_x) positioned at two distinct points in space as illustrated on figure 2.5. It can be shown that the signal received at R_x, which would have been transmitted by Tx and reflected by F_0 and its neighbourhood, is equivalent to a signal which would have been transmitted and received at point PCA_0. The point PCA_0 is positioned on the bisector of the angle $\widehat{T_xF_0R_x}$ at a distance from F_0 such as:

$$||PCA_0F_0|| = \frac{||TxF_0|| + ||F_0Rx||}{2} \tag{2.4}$$

It must be noticed that the position of the equivalent phase centre PCA depends on the focal point F. This is illustrated in the figure 2.5, where two different focal points (F_0 and F_1) are shown. It can be noticed that PCA_1 is slightly ahead of the point PCA_0. These variations are minor compared to the wavelength and it is a valid approximation to consider that the PCA point is in the middle of the segment $[TxRx]$.

Based on this principle a physical antenna can be turned into an equivalent phase centre antenna. As illustrated on figure 2.6, let's consider an antenna with a transmission element (in red) and seven reception elements (in blue). Each element is separated by a distance δ and the total length of the physical array is L. According to the PCA, as stated above, the transmission of a ping and the simultaneous reception on all the reception centres of the physical antenna is equivalent to the successive transmission/reception on the different phase centres of the PCA antenna. This PCA

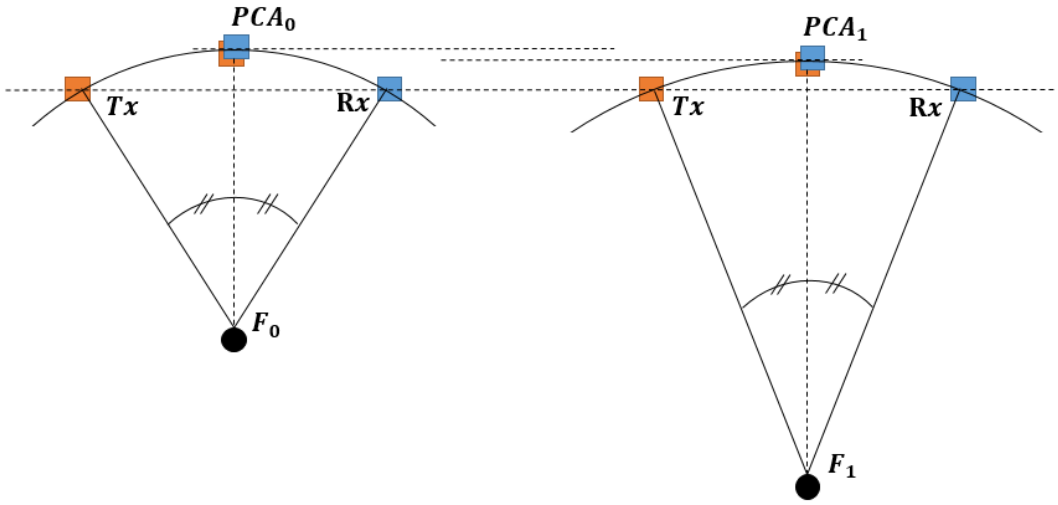

Figure 2.5: Diagram illustrating the geometry of the phase centre approximation for two distinct focal points

antenna has a length

$$L' = \frac{L}{2} \tag{2.5}$$

and inter-sensor distance of

$$\delta' = \frac{\delta}{2} \tag{2.6}$$

2.2.2 Challenges in SAS sonar

Although the theory of SAS dates back to the 1970s, it was not until the 1990s that we saw the first operational SAS. This was due to a number of issues that had to be resolved. The main ones are presented below.

Navigation estimation

That is probably one of the main issue to process SAS images. In fact, in order for each element of a receiving antenna to contribute to the gain in image resolution, the relative element position errors along the synthetic antenna must be less than $\frac{\lambda}{4}$. In practice, it has been noticed that with errors of $\frac{\lambda}{4}$ the deterioration in image

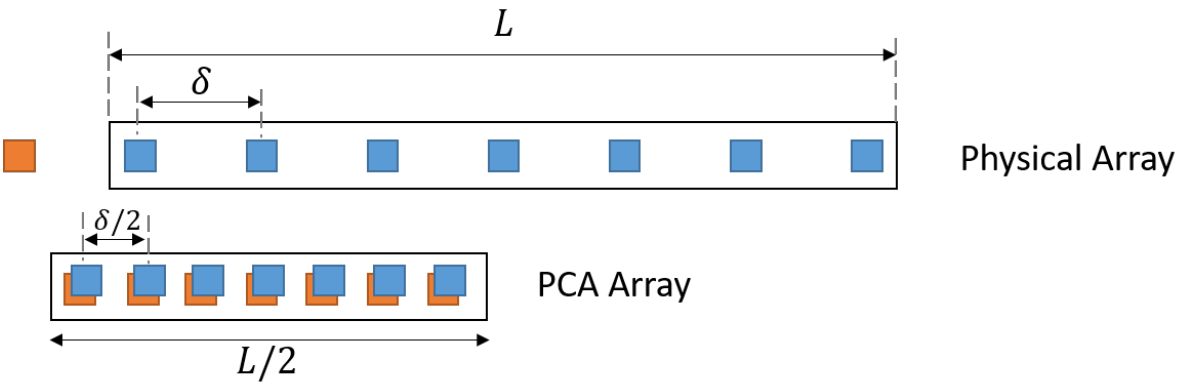

Figure 2.6: Diagram illustrating the equivalence principle between a physical antenna and a phase centre antenna. A physical array of length L with Rx elements spaced by a distance δ is equivalent to a PCA array of length $L/2$ with Tx/Rx sensors spaced by a distance $\delta/2$

quality is already noticeable, which is why constraints of the order of $\frac{\lambda}{8}$ or even $\frac{\lambda}{16}$ are advocated [Carrara et al., 1995]. For a sonar operating at$200kHz$ and a $\frac{\lambda}{8}$ constraint that means a maximum error of $0.9mm$ cumulated over the integration length. That can not been achieved by a classical DVL aided INS system. To deal with this issue one solution (known as micronavigation) aims at estimating antenna displacement from the signals sensed by the various elements of the receiving antenna during several successive pings. The general idea is that if you transmit with a transmitter-receiver pair at the same position but at different times, you receive the same signal. In the case where the positions of the two phase centers are slightly different, in the case of a displacement between two pings, we can observe decreases in correlation level (longitudinal displacement), or a delay (transverse displacement). The Displaced Phase Center Antenna (DPCA) method introduced at the beginning of 90s [Pinto et al., 1997] uses the micronavigation principle to estimate the sonar displacement between two successive pings. Its principle is illustrated in figure 2.7. Let's consider a phase-center antenna as illustrated on figure 2.6. If, between two sonar pings, the antenna has not moved by more than half the length of the PCA antenna (i.e. a quarter of the physical antenna), then at least half the phase centers overlap and it is possible to estimate the correlation of the different signals and to estimate a displacement that is sufficiently accurate to form the synthetic antenna. **DPCA method is based on the notion of spatial coherence that is the purpose of this manuscript**. This notion will be discussed in more details in the following chapter after the introduction of the notion of spatial coherence.

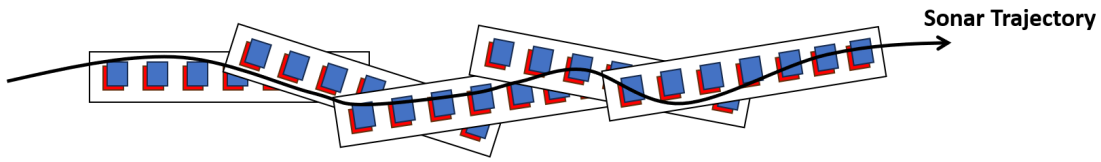

Figure 2.7: Illustration of a sonar trajectory with redundancy between phase centers.

Navigation stability

The principle of aperture synthesis is based on the generation of a virtual linear antenna of long length by moving a smaller physical antenna on a linear trajectory at uniform speed. In practice, this ideal geometry is impossible to achieved due to carrier navigational instabilities. These instabilities can have a significant impact on SAS processing. As long as the instabilities are moderate, they result in irregular sampling of the virtual antenna, which needs to be estimated in order to perform coherent integration (see part 2.2.2). However, greater instabilities can lead to non overlapped phase centers between two successive pings which makes impossible to estimate the micronavigation and can even lead to gaps in the virtual antenna with significant impacts on the quality of the imagery. For example crabbing (when the heading is not aligned with the track) is known to be a challenging issue in SAS processing [Callow, 2010]. A high degree of stability of the antenna is therefore required. The development of SAS sonars has therefore been dependent on advances in this field, in particular the development of AUVs (underwater UAVs).

Ocean environment

In order to perform SAS processing, sound speed has to be accurately estimated. Vertical variations of sound speed (sound velocity depends on depth) as well as horizontal and temporal variations can have significant effects on SAS images [Ji et al., 2019] [Hansen et al., 2007]. The vertical celerity profile can be measured using a celerity profiler or extrapolated from measurements taken at vehicle level, provided that the vehicle is travelling below the thermocline. Horizontal and temporal variations, are much more difficult to measure or to predict (particularly in estuaries where freshwater and sea water mix) and to take into account, and can lead to artefacts in the images. [Hansen et al., 2014].

In shallow water multipaths, are also known to be a major limitation of SAS imaging [Pinto et al., 2004].

2.2.3 Key characteristics quantities of SAS

Range resolution

As stated above, performing pulse compression, range resolution is unchanged from classical sidescan sonars and is function of bandwidth B:

$$\rho_R = \frac{c}{2B} \tag{2.7}$$

Along-track resolution

In the case of SAS, the theoretical longitudinal resolution that can be achieved depends on the maximum size of the synthetic antenna that can be formed. It has been shown that if the receivers are assumed to be punctual this maximum size is limited by the angular aperture of the transmitter θ_e. Indeed, if we wish to focus at a point P_1 located at a distance R_1, the only phase centres that can be used are those that have recorded information from P_1. According to notations on figure 2.8(a), the maximum length of the synthetic aperture that can be achieved at a distance R_1 is written L'_1 and,

$$L'_1 = 2R_1 \sin\left(\frac{\theta_e}{2}\right) \tag{2.8}$$

such a PCA antenna would have an angular resolution

$$\theta_1 \approx 0.88\frac{\lambda}{2L'_1} \tag{2.9}$$

where λ is the wavelength. The $\frac{1}{2}$ factor takes into account the fact that this is a PCA antenna.
Thus at this range, the along-track resolution is

$$\begin{aligned}
\rho_1 &\approx R_1 \cdot \theta_1 \\
&\approx 0.88R_1\frac{\lambda}{L'_1} \\
&\approx 0.88R_1\frac{\lambda}{2}\left(\frac{1}{2R_1\sin\left(\frac{\theta_e}{2}\right)}\right) \\
&\approx 0.88R_1\frac{\lambda}{2}\left(\frac{L_e}{0.88R_1\lambda}\right) \\
&\approx \frac{L_e}{2}
\end{aligned} \tag{2.10}$$

where L_e is the aperture of the transmit antenna that would have produced an angular aperture θ_e. Equation (2.10) shows that the theoretical longitudinal resolution achievable by a SAS is half the size of the transmitter aperture. It should be noted that this resolution is no longer dependent on frequency or range. Although contradictory to the discussion about the physical antenna in paragraph 2.1.1, these two points can be illustrated by the length of the synthetic antenna that can be reached. This is illustrated on figure 2.8. On figure 2.8(a), two focal points (P_1 and P_2) at two different distances are illustrated. For the same given transmit aperture θ_e, the antenna excursion to form the synthetic antenna is shorter for point P_1 than for point P_2 and thus the loss in resolution due to the greater distance is compensated for by the formation of a larger synthetic antenna. Similarly, in the case of a lower frequency, for the same transmitter size, a larger aperture and thus a larger synthetic antenna can be obtained. Again, the loss in resolution due to a lower frequency is compensated by the possibility of forming a larger synthetic antenna. This is illustrated in Figure 2.8(b).

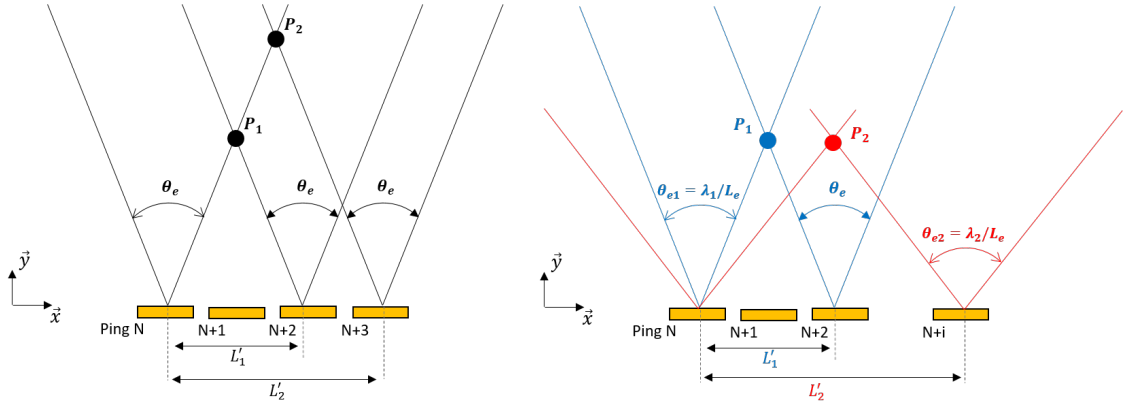

Figure 2.8: (a) Range independent along-track resolution. At the range of P_2, the same aperture θ_e allows to form a synthetic antenna of length L'_2 which is larger than those than can be formed at the range of P_1 (L'_1) (b) Frequency independent along-track resolution. A point P_2 can be insonified by a a fix length L_e Tx antenna with a wavelength λ_2 during a longer interval than a point P_1 wich would be insonified by the same Tx antenna but with wavelength λ_1 ($\lambda_1 < \lambda_2$)

Maximum range

The two results just mentioned (range-independent resolution and frequency-independent resolution) enable to create a sonar capable of detecting small objects at large distances. In fact, unlike sidescan sonars whose design is the result of a compromise between range, antenna size and frequency, SAS offers frequency-independent resolution, enabling the latter to be set for reasons other than resolution. It is therefore natural to want to lower the frequency in order to reduce propagation losses and thus maintain a good signal-to-noise ratio even at great distances. However, the coherent integration length must be longer at low frequencies than at high frequencies in order to achieve a given resolution. This integration time may be difficult to achieve because environmental variability tends to limit the maximum range achievable by SAS. Furthermore, as mentioned previously, in order to form the SAS image, it is necessary to estimate the antenna's movements by the micronavigation method (see part 2.2.2). However, the implementation of such a method requires that the sonar has not moved by more than half the phase center antenna length between two pings. It therefore appears that for long distances (i.e. for long inter-ping times), it is necessary either to increase the receiving antenna size, or to reduce the speed. Thus, the maximum range at which aperture synthesis can be achieved is closely linked to the size of the receiving antenna and the speed of the carrier.

Coverage rate

As expressed above, maximum range and the forward speed of the carrier are linked by the size of the receiving antenna. Let's consider a SAS system with a reception antenna of length L and so a PCA array of length $L_{PCA} = \frac{L}{2}$. To reach and form a SAS image at distance R_{max}, we have seen that the carrier must not have move forward more than half a PCA antenna during the duration $t_{max} = \frac{2R_{max}}{c}$. Thus, noting v_{max} the maximum speed that can be reached by the carrier:

$$v_{max} < \frac{0.5 \cdot L_{PCA}}{t_{max}} = \frac{L \cdot c}{8 \cdot R_{max}} \tag{2.11}$$

Considering now a carrier moving at height z above a flat bottom. The swath of the sonar at maximum range R_{max} is $S = 2\sqrt{R_{max}^2 - z^2}$. Note that the factor 2 is only valid in the case of a dual-edge sonar. The coverage rate $\dot{S}$, i.e area covered in one hour, can be estimated by:

$$\dot{S} = 3600 \cdot S \cdot v_{max} \tag{2.12}$$

Note the criterion of a half a PCA antenna length overlaps is very restrictive and that in practice higher speeds are achieved by performing the DPC on antenna overlaps of less than half a PCA antenna length.
Figure 2.9(a) shows the maximum achievable speed v_{max} for different ranges and different antenna lengths. Figure 2.9(b) shows the coverage rate $\dot{S}$ for different ranges and different antenna lengths.

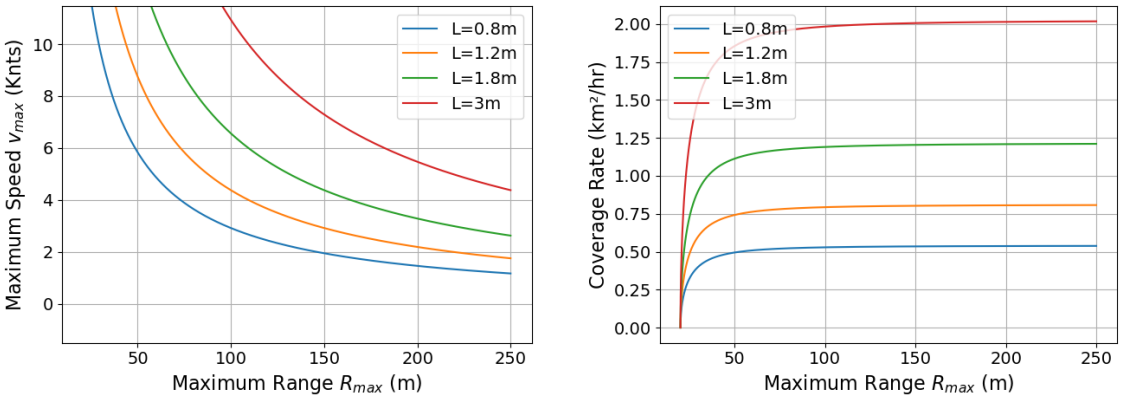

(a) (b)

Figure 2.9: (a) Maximum achievable speed for different ranges and different antenna lengths (b) Coverage rate for different ranges and different antenna lengths)

2.3 Uses of SAS: the mine warfare example

The aforementioned properties of SAS systems show that SAS are particularly suitable for all applications requiring very high resolutions and high coverage rates. Examples include underwater archeology, environmental monitoring, etc. Nevertheless, due to the complexity of these systems and even if they tend to be democratised, they remain of a very confidential use. One of the major uses is in the fight against underwater mines.

2.3.1 Mine warfare context

The conflicts of the late 19th century marked the emergence of a new weapon in the naval field: the sea mine. Defined as an explosive device immersed in water with the aim of destroying or damaging a ship, its use was intended to restrict the navigational

capabilities of a fleet and thus compete for control of the seas. In this regard, two types of mining can be defined:

- **Protective mining**: Protective mining takes place in territorial waters. It consists for a nation in laying mines in particular areas of its territorial waters to make navigation difficult or impossible for enemy forces. The objective may be to force these forces to use passages in which they are vulnerable or to deny them an access. This type of strategy can be used to protect a military or civilian port, and to prevent the landing of enemy forces.

- **Offensive mining**: Offensive mining takes place in enemy waters. The aim was to restrict or even prohibit the movement of an enemy fleet, to block its ports and sea routes. Offensive mining is one of the most effective weapons for blocking enemy naval forces. Its objectives are quite similar to those pursued by the Royal Navy in its port blockade operations. However, where blockades required large numbers of ships and exceptional sea endurance (22 months for Nelson at Toulon in 1804), the deployment of a mine barrier achieves the same objective without the need to mobilise entire fleets.

Sea mines were used extensively during both world wars. One of the most significant offensive mines was laid during the First World War, when the Allies laid over 70,000 mines between Norway and Scotland to prevent German submarines from leaving the North Sea. In total, an estimated 160,000 mines were laid by the Allies and 50,000 by the enemy. The losses were nearly 600 allied and neutral merchant ships and France lost at least 216 warships (including the battleship Le Bouvet, which cost the lives of 648 sailors). The majority of the mines used during World War I were contact mines. This type of mine is detonated by impact with the hull of a ship. As there must be contact with a ship, it is necessary that the mine itself, which contains, in a generally spherical envelope, the charge and the firing mechanism, floats. But as it must not be visible on the surface of the sea and must not drift, it is anchored, i.e. held at a sinker by a rope, so that it is kept between two waters at the appropriate depth. It was also during the First World War that the first mine countermeasures systems appeared. These systems, called mechanical minesweepers, consisted of towing one or more cables by ship to hook and cut the mine ropes. Once the rope is cut, the mine rises to the surface where it can then be counter-mined.

During the World War II, over 700,000 mines were laid on the european seafloor. At the beginning of the war, the Germans began to use a new type of mine, the magnetic mine, which marked a turning point in the history of these devices, since it opened the era of influence mines. These mines are laid on the seabed and are triggered

when a ship passes by the perception of a change in the ambient magnetic field. These mines cannot be mechanically dredged, so magnetic dredges were developed. The aim of these devices is to reproduce the magnetic signature of a ship in order to detonate these mines. Subsequently, the influences to which the mines are susceptible have diversified. In addition to the magnetic, they are also equipped with acoustic and vacuum sensors that are sensitive to both the radiated noise of the ship and the change in hydrostatic pressure caused by the passage of a ship. These are known as multi-influence mines. The sweeping of these mines proves to be all the more complex because intelligent firings (such as counters) are imagined in order to let a part of a convoy pass before being triggered.

Since the end of World War II, the use of bottom mines has become more widespread and despite advances in mine countermeasures, ships continue to be exposed. Examples include the USS Samuel B. Roberts damaged by an Iranian contact mine in 1987 in the Persian Gulf. Despite employing a mine warfare force of minesweepers, mine hunters and disposal teams, the USS Tripoli and USS Princeton were blown up in 1991 while supporting Desert Storm operation.

As expressed above, minesweeping seems hardly compatible with a multi-influence threat equipped with intelligent firings. In the late 1960s, the concept of mine action was born. In contrast to minesweeping, which aims to detonate threats, this concept now aims to identify the threat and then remove it. Mine warfare operations are then carried out in four stages described above:

- **Detection**: Collection of all sonar echoes whose size, shape and intensity can be compared to that of a mine. This phase produces MILECs (MIne Like Echoes);
- **Classification**: Sorting MILECs into two classes: those that may come from a mine (MILCO for MIne Like COntact) or those that do not appear to come from a mine (NoMILCO);
- **Identification**: Inspection of MILCO contacts to verify that it is a mine. If the identification is positive, the object is designated as a MINE otherwise it is designated as a NOMBO (NO Mine Bottom Object). Identification is very often carried out by optical means (camera mounted on an ROV or divers);
- **Neutralisation**: Mine disposal, by destruction, defusing or removal of the threat.

The first two phases of operations (Detection and Classification) are conducted using sonar systems. These sonars, whether frontal or lateral, aim to detect objects

resembling mines from other objects that may be present on the seabed. As sonar technologies have become more and more powerful, stealth mines have been developed. These mines are characterised by coatings or shapes designed to reduce their sonar echo (MANTA, ROCKAN) or shapes that make their discrimination against rocks very complicated (PDM). The following paragraph presents how SAS have become valuable tools to carry out these detection/classification phases with a high level of performance.

2.3.2 Detection-Classification and the use of HF SAS sonar

In minewarfare domain in France, two use case coexist: the surveillance concept and the hunting concept:

- **Surveillance concept**: This use case is implemented in domestic ports in order to protect against a possible offensive mining operation. These operations are carried out using sidescan sonars (DUBM44 type) operated from sonar tug boats. These operations consist in regularly imaging the same area (maritime route, harbour entrance, ...) and detecting at each new passage the objects which were not present on the previous sonar band. In this concept, each new object is suspect and must be identified. This use case is often referred as change detection. It is obvious that to be effective, sonar surveys must be carried out regularly and that the reference band (state 0) must not already contain any threats.

- **Hunting concept**: This use case is implemented wherever the Navy does not have reference sonar bands for change detection. Historically, in this concept, the detection and classification phases are conducted from surface vessels equipped with frontal sonars.

Historically conducted from surface vessels equipped with frontal sonar, the warfare of the world's major navies has undergone a major transformation in recent years. This transformation is mainly driven by the use of unmanned vehicle such as Autonomous Underwater Vehicles (AUV) or Unmanned Surface Vehicle (USV) and SAS systems. The classification of contacts by high-frequency imaging is based on two main criteria: the description of the echo and the associated shadow. The principle of echo and shadow formation is shown in figure 2.10(a). On this figure several phases contributing to the formation of a side-scan sonar time signal can be noticed:

- Phase A: the acoustic wave is propagating through water column. The amplitude of the return signal is low and mainly due to volumic reverberation of the water column;
- Phase B and E: the acoustic wave is backscatterd by the seafloor. The amplitude of the return signal is mainly due to seafloor reverberation;
- Phase C: the acoustic wave hit an obstacle (e.g. Target). The amplitude of the return signal is high and mainly due to the specular echo on the target;
- Phase D: the acoustic wave propagation is blocked by the obstacle and does not reach the bottom. The return signal then shows a zone of very low amplitude, corresponding to a shadow on the image. Note that once compensated for the acquisition geometry, the size and shape of this shadow is linked to the shape and height of the obstruction, and is therefore an important source of information for the classification of mine warfare objects.

SAS images of canonical targets are shown in the figures 2.10(b) and (c). The amplitude is represented in shades of grey, where white represents a high level of backscatter and black a low level. Figure 2.10(b) is a SAS image of a sphere. The white part corresponds to the echo. The spatial resolution achieved thanks to SAS processing allows to estimate the diameter of the sphere. Moreover, the key point that characterizes this target as a sphere is its ellipsoidal shadow. Figure 2.10(c) is a SAS image of a cylinder. Here too, the size of the cylinder can be estimated thanks to the high resolution provided by SAS processing, and the shadow is characteristic of the object's height and shape.

The mine warfare operator's task of detecting and classifying potential suspicious contacts is long and tedious. For this reason, a number of automatic detection/-classification algorithms have been developed in recent years. Depending on the application, two types of algorithms are developed: automatic detection/classification algorithms (for the hunting concept) and automatic change detection algorithms (for the surveillance concept).

Automatic Target Recognition - ATR

As expressed previously, detection and classification processes are tedious and time consuming. Moreover since a human is involved in analysing these images, fatigue and stress could lead to misclassification errors. This is why computer-aided detection and classification has become a very active field of research. The term automatic target recognition (ATR) is used to describe the various algorithms designed to

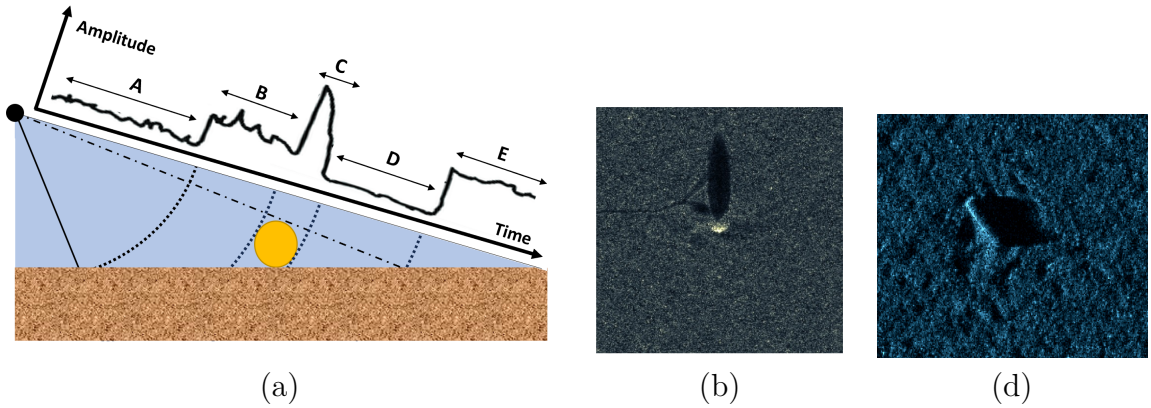

(a) (b) (d)

Figure 2.10: (a) Diagram of the different phases contributing to the formation of a side-scan sonar time signal (b) SAS image of a sphere (©TDMS) (c) SAS image of a cylinder (©TDMS)

help the operator in his task of detection, classification or both. Two major types of detection and classification algorithm can be found in literature: rules based algorithm and machine learning techniques. Rules based algorithm are based on classical image processing aiming at extracting classifying features. This features have to be carrefully hand-crafted previously in order to perform accurate classification [Barngrover et al., 2014]. The main features are mostly based on size of the echo of a contact and the outline of the shadow projected onto the seafloor. Theoretical knowledge of the shape of the mines being sought can be used to build up a database of desired shadow shapes. The automatic shadows extracted from the sonar images are compared with this database and, if the correlation is above a predefined threshold, a positive classification is generated [Florin et al., 2003]. The criteria necessary for the performance of such an algorithm are, firstly, the creation of a bank of realistic and exhaustive masks and, secondly, target images with sufficient resolution and contrast between the shadow and the seafloor reverberation to enable the shadow contour to be extracted as faithfully as possible [Myers and Pinto, 2007].

The rise of algorithms based on the principle of deep learning has also benefited of automatic target classification algorithms based on sonar images. An exhaustive review can be found on [Neupane and Seok, 2020]. Deep learning algorithms need a large amount of data and the lack of data representative of the diversity of threats in the variety of environments potentially encountered results in a real limitation to the performance of these algorithms. Nevertheless, databases are beginning to be set up

and training a deep convolutionnal neural networks (CNN) allows to achieve impressive performances compared to a traditional rules-based classifier[Williams, 2016]. In order to speed up the creation of datasets for training neural networks, sustained efforts are being made to improve the realism of synthetic sonar data generated by a simulator capable of massively producing labelled images [Mari et al., 2022].

Because of a lack of efficiency, or because of a prevailing principle of responsibility, ATRs are not yet responsible for classification, but only for notifying to an operator about a potential target. Consequently, the operator is responsible for making the final decision regarding classification. In this context, we need to consider what information the operator expects and how much confidence he will have in the algorithm. In the case of a rule-based algorithm whose decision can be explained by the predefined rules, the operator can use the same decision criteria to confirm or invalidate the classification. However, in the case of deep learning algorithms where the decision is not (or is less) explainable, the question deserves to be studied. It is in this context that the explicability of neural networks (xAI) was exploited. They aim at studying the possibility of informing the operator in charge of classification of the criteria which led an ATR deep learning to classify or not a contact [Richard, 2022].

Automatic change detection

Automatic change detection refers to all the techniques that aim to detect automatically new objects or structures in a newly acquired dataset that were not present in the reference dataset [Gendron et al., 2009]. Three main procedures exist :

- Automatic detection of change based on an ATR (ATR-CD). The idea here is to use a hunting ATR as described below independently on the two datasets and to associate the detections between the two. The contacts that would appear on the second dataset and that would not be associated with any detection in the first dataset are then considered as changes[Coiras et al., 2008][Nicolas et al., 2019];

- Automatic detection of change based on an incoherent image comparison (ICD). The images are compared pixel by pixel in an incoherent way, i.e. without phase information. The resulting 'difference' image can then be used to identify areas where there are changes[Midtgaard et al., 2011][Quidu, 2012];

- Automatic change detection based on a coherent image comparison (CCD). Here too, the comparison is made pixel by pixel, but in a coherent way, i.e. taking into account both the amplitude and the phase of the pixels. Changes are then detected by a drop in coherence between the two images or by a difference in phase[Myers et al., 2013][Quidu et al., 2012].

The method ATR-CD has many limitations. It is highly dependent on the performance of the ATR used, and it is often necessary to make assumptions about the size or shape of the objects we are looking for in order to achieve an acceptable false alarm rate (see previous paragraph). In addition, in very cluttered environments where there are many contacts, the contact association phase can generate errors. ICD and CCD methods are not dependent on the performance of an ATR. However, a key point for CCD algorithms is that the images must be coregistered with a high degree of accuracy [Myers et al., 2017].

2.3.3 Low frequency sonars use in a mine warfare context

Resolution and ease of image interpretation are the reasons why navies are using high-frequency sonar (>100kHz) for mine detection and classification operations. However, these devices suffer from two major limitations:

- Acoustic waves at considered frequencies do not penetrate sediments. As a result, the devices are completely ineffective at detecting buried objects. In the case of semi-buried objects, classification performance is also limited. We saw earlier that the shadow projected by an object on the seabed in a sonar image is much used by operators in their classification task. This projected shadow provides information about the height and shape of the contact. However, if the contact is partially buried, the projected shadow is reduced, which can mislead operators or classification algorithms.

- High-frequency systems enable operators to carry out their classification task by exploiting the echo and shadow information of a target, which describes its size and shape. This process is very effective on certain types of target (cylindrical targets, for example), whose size is imposing and whose shape is characteristic of a manufactured object. On the other hand, for smaller targets or targets with a random shape similar to that of a rock, high-frequency systems are less effective. In other words, a high-frequency system cannot tell the difference between a mine and a rock of the same shape.

Reducing the frequency of mine-hunting systems should make it possible to overcome these two limitations.

Buried object detection

As expressed previously high frequency sidescan sonars produce high-resolution images whose almost 'photographic' quality makes them easy to interpret by an operator.

However, since acoustic wave does not penetrate into the sediment at these frequencies, such systems cannot be used for the detection of buried objects.

Non-acoustic methods have been proposed to address the need to detect buried objects, but for the moment these methods have not performed satisfactorily. This include methods based on the use of a several magnetometers forming a gradiometer [Salem et al., 2005] [Munschy et al., 2007] [Czipott and Iwanowski, 1997]. The use of a gradiometer makes it possible to measure the gradient components of ferromagnetic objects and with appropriate processing, such as inversion, makes it possible to estimate the range, bearing and magnetic moment of the target of interest. However this type of system suffers from two major limitations. Firstly, they are only effective on targets with large masses of ferromagnetic material (steel, for example), but are completely ineffective on other types of material such as aluminium or the composite materials commonly used in certain types of mine. In addition, the detection ranges of this type of system are very small (around ten metres for targets weighting several hundred kilograms of steel), which means that the systems have very low coverage rates. To deal with the limitations of magnetometers, which passively detect only ferromagnetic objects, electromagnetic systems use active detection, sending out an electromagnetic pulse. This pulse then magnetizes conductive objects (including non-ferrous objects), whose magnetic signature is then picked up by the reception device [Han et al., 2019]. Operational tests have demonstrated its ability to detect LMBs (*Luftwaffe Mine Bomb*, a german aluminium bombs from the World War II) [map,]. Here again, however, the system's short detection range and cumbersome size make it difficult to use operationally in a mine warfare context. To complete the list of non-acoustic methods for detecting buried objects, we can mention the use of Ground Penetrating Radar (GPR). But rather than using magnetism for detection it uses radio waves as in a regular radar system. Its operating principle is similar to that of an active electromagnetic detection device as mentioned above, except that a GPR uses radio waves. These devices are used to detect buried landmines [Andrews et al., 1999] [Schreiber et al., 2016] , but with the exception of shallow bodies of fresh water [Fediuk et al., 2022], it is impossible to exploit them due to the conductivity of seawater, which severely limits the propagation of electromagnetic waves.

In the field of acoustic sensors, a number of developments are underway to develop a buried object detection system whose performance (in particular the coverage rate) and implementation would be compatible with operational use. Sub bottom profilers (SBP) are effective tools to visualize sedimentary layers. Their low frequency (of the

order of a few kilohertz) enables them to penetrate sedimentary strata up to several tens of metres deep [Lurton, 2002]. They have been used successfully to search for buried spatially extended features such as shipwrecks [Winton, 2023], pipelines or cables [Guerrero et al., 2021]. However, as their name implies, they are profilers, i.e. they only take a measurement directly above the device and therefore do not provide a swath necessary to detect and localize small object over large areas. In the case of SBPs with a large beamwidth, a kind of coverage can be obtained by exploiting the size of the beam's footprint on the seafloor. However, this coverage is achieved at the expense of spatial resolution and therefore the detection and location performance that is so important in mine warfare. On the contrary, in the case of SBP with narrowbeam, the beam's footprint on the seabed is narrow, providing good detection and location capabilities but making any attempt of an exhaustive coverage of an area futile. For very specific applications requiring highly resolved data at high densities and low water depths, some systems combine several SBP transducers to increase density and spatial coverage [Inn, a] [Inn, b]. With the aim of increasing swath, low frequency multibeam echosounders have been developed. One can cite as example the BOSS system [Leasko, 2012], the seachirp system [Plantevin, 2017], and the Pangeo Sub-Bottom Imager [Merlin et al., 2011]. This type of system has demonstrated its ability to detect buried objects with good resolution at burial depths of several metres and over swaths of several tens of metres. Their limitations lie in the size of the devices and the fact that they have to be used close to the seabed in order to maintain high spatial resolution. Finally, to conclude this review of devices for detecting buried objects, we can mention low-frequency sidescan sonars [Hunter et al., 2012] [Tanaka et al., 2003] [Nakamura et al., 2004] [Hetet et al., 2004]. The use of a broadband signal and synthetic aperture processing enables these systems to achieve resolutions compatible with the detection of buried objects on large swaths.

A special word needs to be said about the concept of classifying buried objects or, more generally, about classifying objects using low-frequency sonar. As expressed previously, in mine warfare using traditional high frequency systems, the classification of an object is based on its shadow cast on the seafloor. However, in the case of low-frequency imaging (and even more so in the case of a buried object) no shadow can be exploited. So even if good resolution can be achieved and thus provide information on the coarse dimensions of the object, the description of its shape will remain less detailed than what can be achieved using high-frequency systems. So, in order to limit the false alarms generated by a low-frequency system, it is important to find new characteristics of the image or signal that can discriminate a threat from another contact present in the area. It will also be important to define an suitable way of

representing this information. This will be all the more important in the case of buried contacts for which current identification solutions (video, very high resolution acoustic imaging) will not be relevant.

Resonance based classification

Generally speaking, for frequencies above 20kHz and an object with characteristic dimensions of 1m, the object can be considered as a rigid diffuser and acoustic scattering is well described by the geometric theory of diffraction. As the frequency decreases, a non-negligible proportion of the energy can penetrate and give rise to waves travelling around the periphery of the object and, under certain conditions linked to the shape and elasticity of the object, the angle of incidence and the frequency, can create constructive interferences known as resonances [Nicq, 1998]. Modelling [Sessarego et al., 1997] [Talmant et al., 1988] [Déculot et al., 1994] [Gespa, 1987], simulations [Zampolli et al., 2007] [Nicq and Brussieux, 1998] [Sabatini et al., 2022], and experiments [Pinto et al., 2002] [Tesei et al., 2002] on simple geometries have highlighted the existence of these resonances. These studies have highlighted the circumferential resonances circulating in the outer shell (Lamb-type compression waves, guided shell waves), or at the interface between the shell and the external environment (Scholte-Stoneley type). These appear in particular when the length of the path travelled is a multiple of the wavelength and will occur more easily in elastic objects of regular shapes (typically manufactured objects). If the insonified object is filled with a material that allows the acoustic wave to propagate (as opposed to an object filled with air), the various internal reflections will add to the response of the object. These contributions are known as fluid cavity resonances. Exploiting these phenomena should lead to substantial operational gains by making it possible to discriminate between two objects of the same shape but with different internal compositions. However, the low level of some of these phenomena, as well as their variability depending on the type of target and the incidence with which the objects are insonified, make it difficult to exploit them in operations [Bucaro et al., 2007] [Zerr et al., 1999].

Challenges using low frequency wide band sonar systems

Whether for the detection of buried objects and/or for classification based on resonance, low-frequency systems come up against the need to reduce the volume and surface reverberation of the seabed in order to enable high-performance detection and classification. All three dimensions are affected by this reduction in resolution:

- **Range resolution:** As expressed in part 2.1.1, for chirp signals and after matched filtering, range resolution is inversely proportional to bandwidth. It is therefore preferable to use the widest possible frequency bands. In addition, as well as helping to reduce volume reverberation, the use of a wide bandwidth should make it possible to cover greater spectral diversity and therefore improve the performance of resonance classifications. In practice, it is the transducer technology that limits the bandwidth that can be used. The bandwidths available depend on the system's centre frequency: the lower the frequency, the more difficult it will be to use large bandwidths. In [Roed et al., 2020], a bandwidth of 120% of the central frequency is mentioned for a transducer with PZT active material and a bandwidth of 150% of the central frequency for a single crystal transducer. Generally speaking, a bandwidth of 100% of the central frequency already corresponds to very good efficiency.

- **Along-track resolution:** Similarly to what is done on high-frequency systems, it is interesting to improve the along-track resolution in order to be able to estimate the dimensions of the target and to reduce seafloor and sediment volume reverberations by reducing the size of the resolution cell [Hetet, 2003]. In order to obtain the smallest possible apertures without unrealistically increasing the dimensions of the acquisition device, it is possible to perform aperture synthesis [Hunter et al., 2012] [Amate et al., 2005]. It should be noted that because of the poor directivity of the beams at low frequencies, the gains expected by synthetical processing are very high, which means that very long antennas (of the order of several tens of metres) have to be synthesised. However, if the aim of the user of a low-frequency SAS is to exploit resonances, it should be noted that the aperture synthesis process may tend to reduce the detectability of these phenomena. In fact, as expressed above, the appearance of resonant phenomena can be dependent on the aspect by which the target is insonified. Since the principle of aperture synthesis is to integrate several aspects, such a processing may reduce the detectability of these phenomena [Hunter et al.,]. Instead of SAS, a solution based on a towed linear antenna could be considered [Mopin et al., 2016]. However, such systems would need to operate at lower frequencies than those considered here.

- **Elevation resolution:** As with the along-track, the elevation resolution must also be reduced. As with high-frequency systems, this reduction in vertical aperture is necessary to reduce the influence of multiple paths [Pinto et al., 2004] but in the case of a low-frequency system, this reduction in aperture is all the more necessary as it helps to reduce the surface reverberation of the bottom

and the volume reverberation of the sediment. Furthermore, if the elevation resolution is fine enough, it is possible to estimate the depth of burial of a possible contact. Unlike the above-mentioned problems of distance and bearing resolution, which are common to high-frequency systems, the problem of the elevation resolution is specific to low-frequency systems. The three systems mentioned as examples above (MUD, BOSS, and seaChirp) solve this problem by using a large receiving antenna in the vertical direction. However, such devices take up a lot of space, which makes them difficult to use in operational situations. The integrations of these three sonars are shown in Figure 2.11. For down looking geometry systems (BOSS sonar and seaCHIRP sonar), this antenna is placed horizontally and acts as a wing on the carrier (see Figures 2.11(b) and 2.11(c)). For side looking geometry systems (MUD), this antenna is placed vertically, possibly tilted about thirty degrees from the vertical as illustrated on Figure 2.11(a). This acquisition geometry is also that used by the HRLFSAS system studied in this work (see part 2.3.4). Such a device would be complex to integrate into an underwater vehicle or on a towed fish. For this type of device, the elevation resolution depends on the size of the antenna and the working range. Thus a decrease on the size of the device (to facilitate its integration into a carrier, for example) will inevitably lead to a reduction in the number of working hours and therefore in the coverage rate of the system. Another way of obtaining low aperture beams at low frequencies is parametric emission. Successfully applied to sub bottom profilers [GmbH, 2009], parametric emission allows to obtain high directivity low frequency beams with an antenna size not very large compared to wavelength. The other benefits are the large bandwidth potentially available and the low level of the side-lobes in the directivity pattern. A parametric multibeam system with synthetic aperture for detection of buried mines has demonstrated its ability to detect buried objects over a wide swath [Foulon et al., 2011]. The main disadvantage of this method is that, since the narrow parametric beam is generated at the emission, it is necessary to steer the emission in order to cover a wide angular sector, which reduces the forward speed of the carrier and therefore the coverage rate.

The need for low frequency, large bandwidth and narrow beams in order to respectively have a correct sediment penetration, have a good resolution and limit reverberation, mean that systems for detecting buried objects are very difficult to design and are the result of a number of compromises including, first and foremost, system size versus detection performances. Parametric emission, synthetic aperture and adptative beamforming are just a few examples of techniques for achieving good resolutions while maintaining moderate sizes of systems [Kopp, 2004].

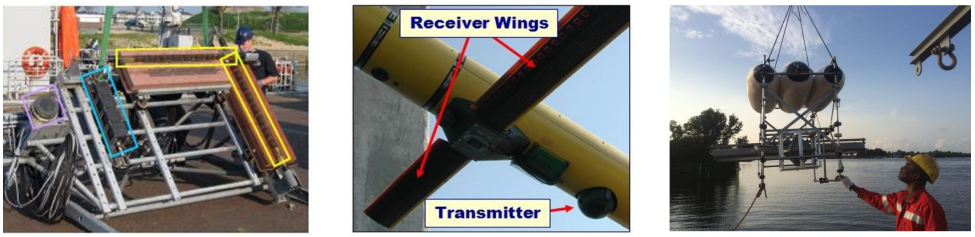

(a) (b) (c)

Figure 2.11: (a) MUD system including receiver arrays (yellow boxes). LF source (blue box), and HF source (Violet box) [Hunter et al., 2012] - (b) BOSS system as integrated on Bluefin 12 UUV [Leasko, 2012] - (d) SeaCHIRP system [Plantevin, 2017]

2.3.4 The HRLFSAS System

As part of the the High Resolution Low Frequency Synthetic Aperture Sonar (HRLFSAS) project, NATO CMRE develops a prototype sensor for the enhanced detection, classification, of objects not detectable or easily recognizable by operational higher-frequency sonar systems and especially for objects partially or fully buried in the seabed. This system consists on a 2D transmitting array with independently driven elements, capable of delivering wideband signals. The transmitter is coupled with a receiver array to perform high-resolution SAS (Synthetic Aperture Sonar) acoustic imaging. Description of the transmit device can be found in [Fioravanti et al., 2019]. The reception system consists of a vertical antenna and a horizontal antenna arranged as shown in Figure 2.12 tilted at 30° from the vertical direction. The horizontal antenna comprises 12 reception elements (red dots on Figure 2.12) and the vertical one comprises 16 reception elements (blue dots on Figure 2.12).

Throughout this document, the coherence phenomena presented in this work are illustrated using data acquired by the HRLFSAS system and made available by the CMRE. These data were acquired during the TORHEX'18 campaign, which took place in July 2018. During this campaign, the acquisition device (transmission and reception) was attached to the end of a submerged mast, itself attached to a carriage capable of moving along a rail installed on the CSSN[1] pier. Facing the pier, the seabed is mud, and some targets were positioned on the seabed between 6 and 10 meter water depth.

Acoustic data consist in a set of 800 pings containing 16 signals from the 8 central

[1]Centro di Supporto e Spertimentazione Navale

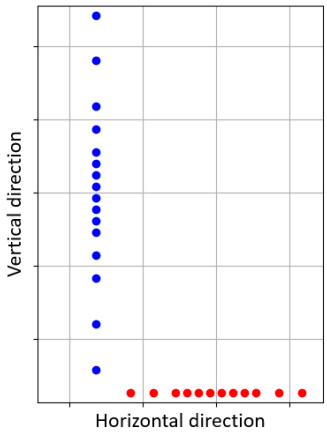

Figure 2.12: HRLFSAS Rx array geometry. Blue dots represent positions of receivers of the vertical antenna, red dots represent positions of receivers of the horizontal antenna.

elements of the horizontal and the vertical array. Each signals corresponds to the recording of 1000 samples from 1 receiver. The sampling frequency is $120kHz$, sound speed has been measured at $1530m \cdot s^{-1}$ and timing of the first sample of each signal is $30ms$. Moreover, between two pings, the carriage is displaced by a distance of around $3cm$ and controlled by a ranging laser. Therefore, the dataset cover an area of around $24m$ in the along-track direction and $6.25m$ in the range direction. This area is centered on an air filled sphere as pictures on Figure 2.13. Figure 2.13(a) represents a sidescan-like image of the data computed by stacking the envelop of all the 800 pings. Figure 2.13(b) represents a SAS image of the sphere computed by performing an aperture synthesis on the 8 central elements of the vertical antenna as it moves along the rail.

2.4 Chapter summary

We have seen in this chapter that SAS systems are increasingly used in the mine countermeasure domain as they can produce images of the seabed with range-independent and frequency-independent resolution. With conventional sidescan sonars, the choice of sonar frequency depends mainly on the range and resolution required. This raised the question of what frequency to use for SAS mine warfare systems. Market research shows that the solution has been to use frequencies that are rather high compared

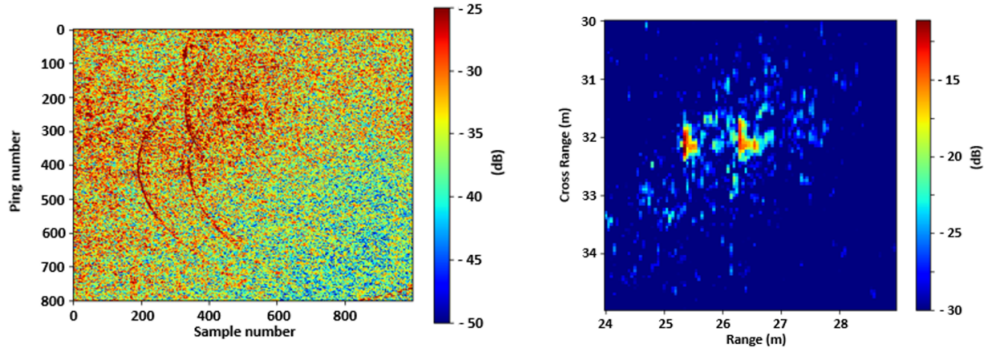

(a) (b)

Figure 2.13: (a) Sidescan-like image of the data computed using one element of the array - (b) SAS image of the data computed using the 16 elements of the vertical antenna through its displacement along the scene.

to the size of the objects sought (>150kHz, generally around 300kHz), mainly for reasons of interpretability of the sonar images produced. In addition to resolution, high-frequency SAS systems enable images to be obtained with very high contrasts between target echoes, projected shadows and the surrounding seabed. These image characteristics are used by mine countermeasures operators or by automatic recognition algorithms to distinguish a threat (a mine, for example) from a rock on the seabed. However, these HF SAS systems suffer from two major limitations: firstly, they are completely ineffective on buried objects, and secondly, their performance drops when the objects are partially buried or when the seabed is studded with rocks of a size and shape compatible with a mine (cluttered environment). To deal with this issue low-frequency SAS systems are currently being developed. Because it penetrates the sediment, the use of low-frequency waves should enable buried objects to be detected. In addition, the use of low-frequency waves should also make it possible to exploit the elastic scattering of a target and thus discriminate between objects of the same shape but with different internal compositions.

The notion of spatial coherence plays a fundamental role in the sonar's ability to detect, locate and characterise underwater objects in a wide variety of maritime and underwater applications, and especially for interferometric SAS systems. The following chapter introduces the notion of coherence.

Chapter 3

The notion of coherence

First studied for light waves, the notion of coherence goes back to the end of the 19th century, beginning of the 20th. The coherence of two waves expresses how well correlated the waves are and as quantified by the cross-correlation function. It thus can be said that two waves are coherent if they have a constant relative phase [Winter et al., 2020]. Two types of coherence of signals can be distinguished: the **temporal coherence** and the **spatial coherence**. The temporal coherence deals with the correlation of a wave field with a delayed version of itself sensed at the same point of space. The spatial coherence deals with the correlation of a wave field with a version of itself in another point of the space but without temporal lag between them [Goodman, 1985]. Obviously in practice, both components are present but for reasons of understanding it is necessary to separate these two points.

This chapter consists on an introduction of the notion of coherence. In sections 3.1 and 3.2 fundamental notions and definitions of temporal and spatial coherence are presented. A fundamental result of the concept of spatial coherence consist on the Van Cittert Zernike (VCZ) theorem that is presented in section 3.4.1. Finally in section 3.5, an example of the use of the concept of spatial coherence is introduced through the estimation of displacement by Displace Phase Center (DPC) method.

3.1 Temporal coherence

Temporal coherence characterises the time extent to which a wave can interfere with a delayed version of itself. It can be expressed as the average correlation between a sampling of this wave and this same sampling delayed by a time τ. The delay after which the resemblance of the original sampling to the delayed one is significantly

reduced is defined as the **coherence time** τ_c. By defining $s_i(t)$ a signal sensed at position X_i of the propagation space, the **temporal coherence** can be computed through the autocorrelation function $\Gamma_{ii}(\tau)$:

$$\Gamma_{ii}(\tau) = \mathbb{E}\left[s_i(t+\tau) \cdot s_i^*(t)\right] \tag{3.1}$$

where * represents the complex conjugate.

It is usually convenient to work with the autocorrelation function normalized by its value at the null temporal lag to define the **degree of self coherence**:

$$\gamma_{ii}(\tau) = \frac{\Gamma ii(\tau)}{\Gamma ii(\tau = 0)} \tag{3.2}$$

The theoretical case of a monochromatic wave is illustrated on figure 3.1.a. On this figure, a signal ($s(t)$) and the same signal delayed by τ ($s(t+\tau)$) are plotted. Because for each delay τ, the signal is perfectly correlated with the delayed version of itself, the coherence time is infinite ($\tau_c = \infty$) as illustrated on figure 3.1.c. On figure 3.1.b a signal whose phase drift significantly during observation time is plotted as well as the delayed version of itself. In such a case of a non-monochromatic signal, at any particular time t, the signal can interfere with its delayed version but since half the time interference are constructive and half the time interference are destructive, averaging over time lead to a null correlation. It can be shown that coherence time is reduced with the range of frequencies Δf according to the following relation

$$\tau_c \approx \frac{1}{\Delta f} \tag{3.3}$$

In the sonar field, pulsed signals are used. Because of their finite length, these signals are never monochromatic. Let's first consider the case of a truncated sinus wave whose mathematical expression is given by (3.4). For such signals (also called CW), the frequency excursion is of the order of $\Delta f = \frac{1}{T}$.

$$s_e(t) = \Pi_T(t) e^{j(2\pi f_0 t)} \tag{3.4}$$

where T is the pulse length, f_0 is the central frequency and $\Pi_T(t)$ the gate function with parameter T such as:

$$\Pi_T(x) \begin{cases} 1 \text{ if } |x| < \dfrac{T}{2} \\ 0 \text{ if } |x| > \dfrac{T}{2} \end{cases} \tag{3.5}$$

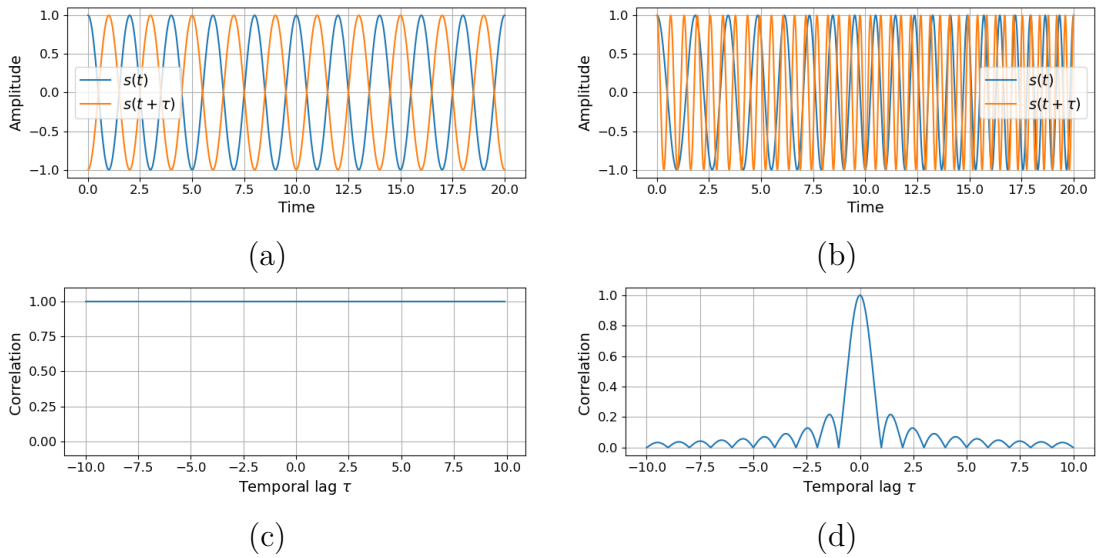

Figure 3.1: (a) Monochromatic signal ($s(t)$), and delayed version of itself ($s(t+\tau)$) - (b) Signal whose phase drift significantly during observation time ($s(t)$) and delayed version of itself ($s(t+\tau)$) - (c) Degree of self coherence of monochromatic signal for different temporal lags- (d) Degree of self coherence of non-monochromatic signal for different temporal lags (from [Gerry and Knight, 2004])

Note that the choice of the gate function is arbitrary and that another function (Tuckey, Gaussian, ...) can be used. On figure 3.2, this CW is represented with different delayed versions of itself. On figure 3.2.a, the temporal lag is null and the two signals are fully correlated. Then on 3.2.b, the two signals are separated by a delay $\tau = T/2$. At this delay, only half of the blue wave is correlated to the yellow one and thus temporal coherence is reduced. From a delay $\tau = T$ (figure 3.2.c) and $\tau > T$ (figure 3.2.d) signals are not correlated anymore. The evolution of the correlation for several values of T as a function of delay is shown on figure 3.2.d. As expected, coherence time is proportional to T. This point is in accordance with the expected coherence time expressed at equation (3.3). It must be noted that triangular shapes observed on correlation curves is related to the rectangular gate function Π_T. If other shapes of the gate function are chosen, other shapes of correlation curves are expected.

Another signal usually used in sonar field, is the Linear Frequency Modulation or

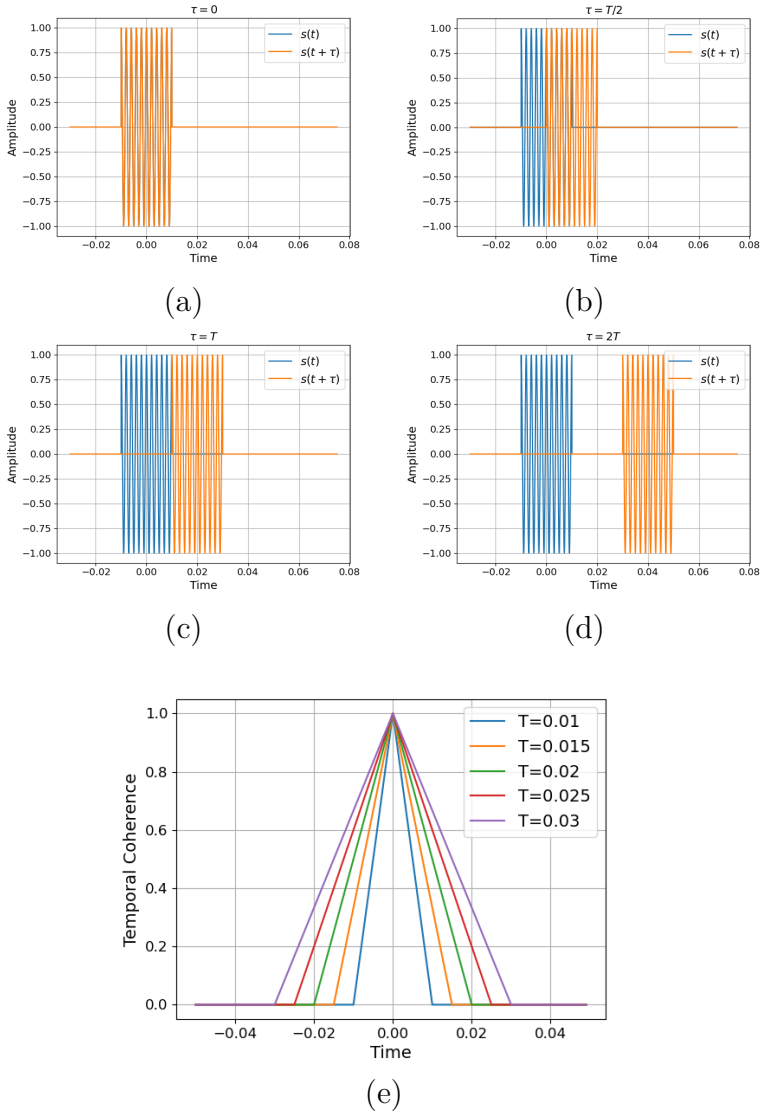

Figure 3.2: CW signal $s(t)$ and delayed version for several time lag : (a) $\tau = 0$ - (b) $\tau = \frac{T}{2}$ - (c) $\tau = T$ - (d) $\tau = 2 \cdot T$ - (e) Temporal coherence as function of temporal lag for several values of pulse length T in the case of a CW signal.

chirp signal. This signal can be mathematically expressed by:

$$s_e(t) = \Pi_T(t) e^{j(2\pi f_0 t + \pi \frac{\Delta f}{T} t^2)} \tag{3.6}$$

In such a case, the bandwidth Δf and the pulse length T are no longer correlated and $\Delta f \neq \frac{1}{T}$. Coherence as function of temporal lag in the case of a chirp signal are plotted on figure 3.3. On figure 3.3(a), figures of coherence for several pulse length T and a same bandwidth Δf are plotted. Figures of coherence are the same: coherence length does not depend anymore on pulse length. On figure 3.3(b), figures of coherence for several bandwidths Δf and a same pulse length T are plotted. It can be seen that the larger the bandwidth, the narrower the main lobe of the coherence pattern. This result is similar to what has been observed in the case of the CW signal. The shape of the coherence figures observed on the figure is a cardinal sine whose opening is inversely proportional to the bandwidth. This cardinal sine is the one produced by the pulse compression in the case of a chirp signal. One can highlight that as it has been introduced the temporal coherence refers to the ability of a signal to interfere with a delay version of itself, but it also refers to the ability of a system to isolate two distinct contributions within a signal. This notion is better known in the radar or sonar field as the temporal (or range) resolution.

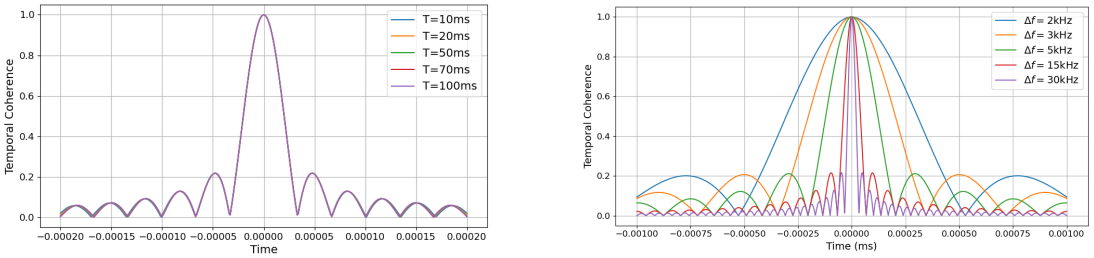

(a) (b)

Figure 3.3: (a) Temporal coherence as function of temporal lag for several values of pulse length T in the case of a chirp signal - (b) Temporal coherence as function of temporal lag for several values of bandwidth Δf in the case of a chirp signal

3.2 Spatial coherence

The spatial coherence deals with the similarity of a signal with a version of itself in another point of the space but without temporal lag between them. In a similar way to the coherence time introduced above, we can define the **coherence length** which defines the distance from which the coherence between two signals of the same wave

sensed at two different positions is significantly reduced. Figure 3.4 illustrates some waves with different temporal and spatial coherence configurations. On figure 3.4(a), the wave has a constant period and a plane wave front: both coherence time τ_c and coherence length L_c are infinite. On figure 3.4(b), the wave has a constant period and still has a regular wave front (single spatial frequency): both coherence time τ_c and coherence length L_c are infinite. On figure 3.4(c), the wave has an irregular period and a regular wave front: coherence time τ_c is finite and coherence length L_c is infinite. On figure 3.4(d), the wave has an irregular period and a irregular wave front: both coherence time τ_c and coherence length L_c are finite.

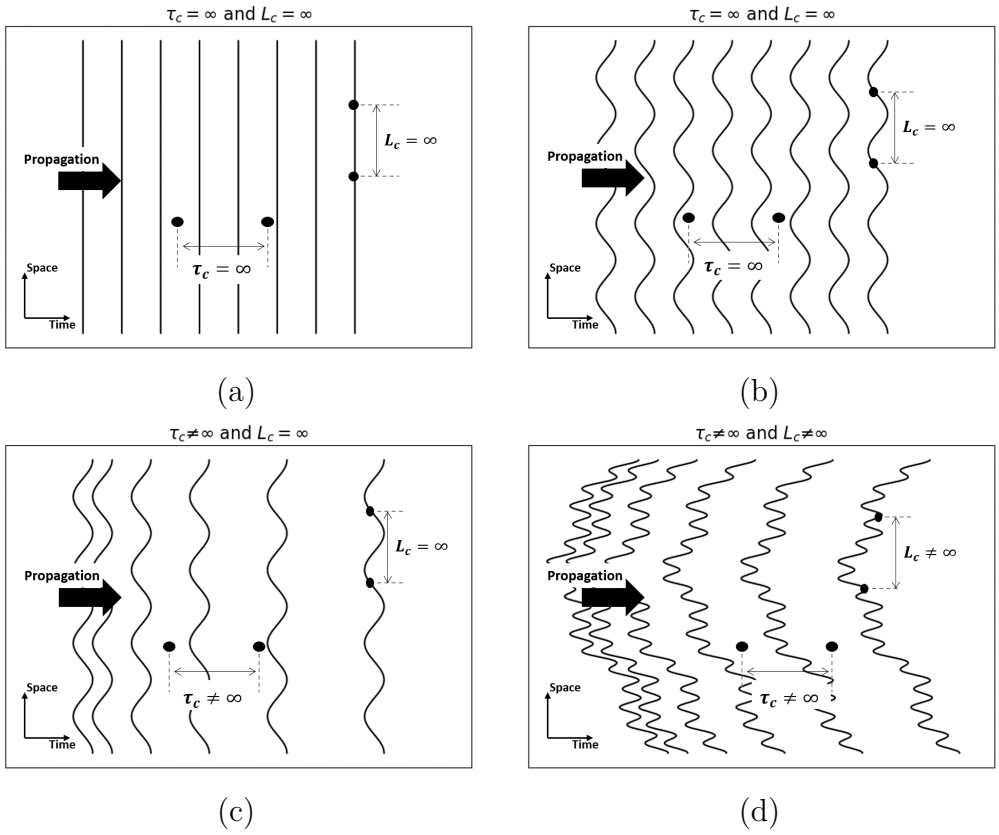

Figure 3.4: (a) Plane wave with infinite coherence time τ_c and infinite coherence length L_c - (b) Wave with regular period (infinite coherence time τ_c) and regular wavefront (infinite coherence length L_c) - (c) Wave with irregular period (finite coherence time τ_c) and regular wavefront (infinite coherence length L_c) - (d) Wave with irregular period (finite coherence time τ_c) and irregular wavefront (finite coherence length L_c)

Another illustration of the spatial coherence is given on the figures 3.5 and 3.6. On figure 3.5(a), a spherical wave propagating from a punctual source is illustrated. Its wavefront is regular and thus coherence length L_c is infinite. The shape of the figure of coherence is shown on figure 3.5(b) where an infinite coherence length can be noticed.

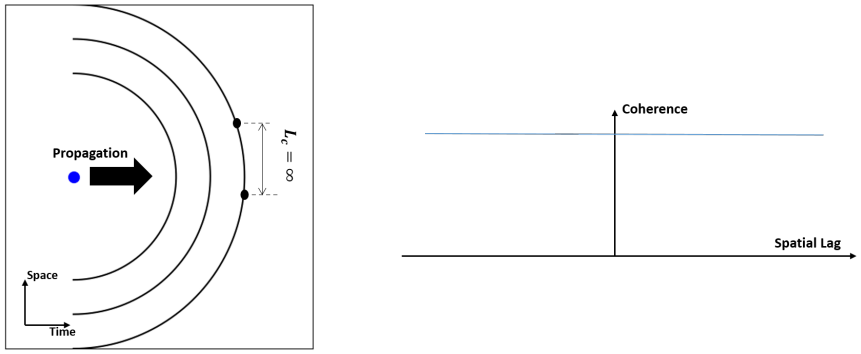

(a) (b)

Figure 3.5: (a) Spherical wave propagating from a ponctual source with regular period (infinite coherence time τ_c) and regular wavefront (infinite coherence length L_c) - (b) schematic view of the coherence function of spatial lag for the spherical wave. Spatial coherence length is infinite.

On figure 3.6, the effect of three spherical waves propagating from three punctual sources that are not co-located is illustrated. On figure 3.6(a), at short range (blue curve) the wavefront is strongly irregular and the coherence length L_c is finite. At medium range (red curve) the wavefront is slightly irregular and the coherence length is still finite but longer that in the case of the blue curve. At far range (green curve), the wavefront can be considered as regular, distribution of sources from this distance is seen ponctual and the coherence length is infinite. This illustration is similar to the one presented with ducks entering a pond in [Knox et al., 2010].

At that stage, the reader can begin to get a glimpse about the link between spatial coherence and distribution of scattered intensity: the spatial coherence length is inversely related to the extent of the distribution of radiated intensity.

In [Goodman, 1985], the author introduces spatial coherence by an explanation of the well known Young's slit experiment. Let us say a word about the experi-

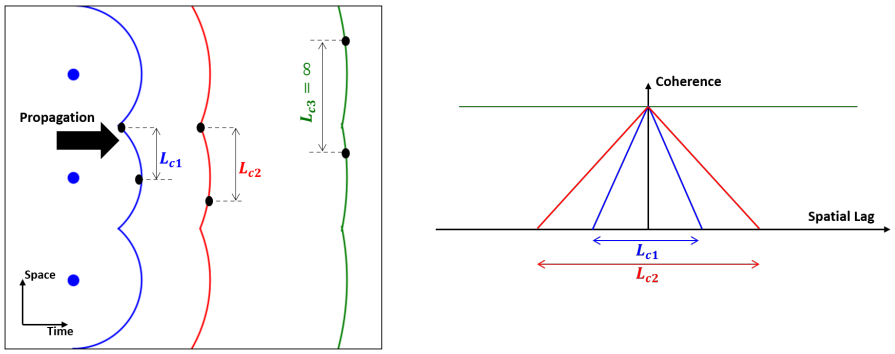

(a) (b)

Figure 3.6: (a) Sum of three spherical waves propagating from three ponctual sources that are not co-located. At short range (blue curve) the wavefront is strongly irregular (finite coherence length L_c), at medium range (red curve) the wavefront is slightly irregular (finite but longer coherence length L_c). At far range (green curve) can be considered as regular (infinite coherence length L_c) - (b) schematic view of the coherence figure for the three ranges.

ment for the understanding of the notion of spatial coherence. The Young's slit experiment is illustrated on figure 3.7. For this section, we have used the notations of [Goodman, 1985]. It consists of a spatially extended incoherent light source S illuminating an opaque screen in which two tiny pinholes have been pierced at points P_1 and P_2. At some distance behind the opaque screen a viewing screen is placed, and the pattern of interference of the light from the two pinholes can be observed on this screen. Insofar as it makes it possible to observe the ability of signals from two holes P_1 and P_2 to interfere, the display screen acts here as a 'coherence detector' for the source S: if interference fringes are visible, that means that the wave field coming from the source S and captured at points P_1 and P_2 is able to interfere and therefore is coherent. The Young's slit experiment reveals the following phenomena:

- when holes P_1 and P_2 are close, the interference fringes are quite visible and this visibility decreases as the distance between points P_1 and P_2 increases. Because this visibility (and so the coherence) depends on the distance between pinholes, it is possible to define the spatial coherence as a function of spatial lag $||P_1P_2||$

- fringes visibility evolves with respect to the distance between the source and the opaque screen with the two pinholes: it is narrow very close to the source

and becomes wider as the distance between the source and the opaque screen increases.

- fringes visibility depends on spatial extension of the source S. The wider the spatial extension of the source, the more interference fringes will only be visible for small spatial lag $||P_1P_2||$

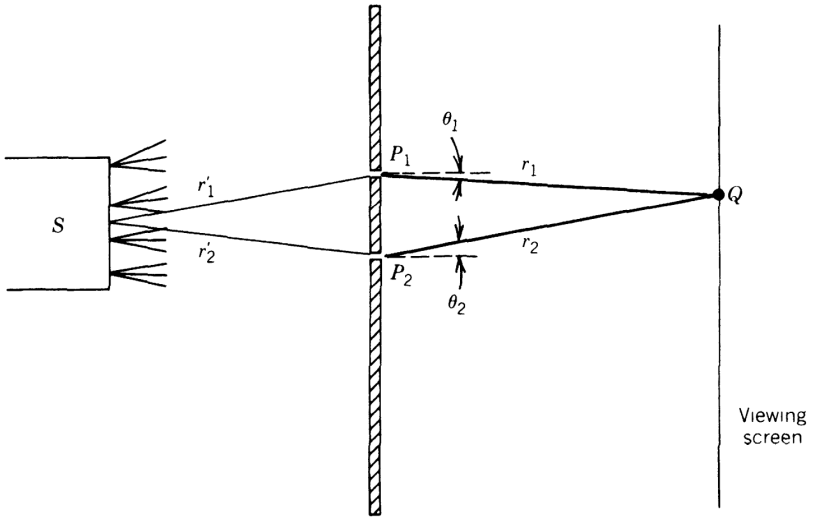

Figure 3.7: Young's interference experiment [Goodman, 1985]

Thus, from the Young's slit experiment it would seem that firstly spatial coherence is a function of spatial lag and decreases as the distance between observation points increases. Secondly coherence length is a function of the distance between the source and the observation plane: the greater this distance, the greater the coherence length. Thirdly, coherence length is a function of the spatial extension of the source: the wider the spatial extension, the shorter the coherence length. These three points are predicted by the Van Cittert Zernike theorem, that under some assumptions, relates spatial coherence to the 2D Fourier transform of distribution of intensity over an incoherent source. This theorem is presented in more detail in part 3.4.

In order to probe further in the definition of spatial coherence, let's consider a set of N receivers at positions $\{X_0, X_1, ..., X_N\}$. These receivers sense over time a wave field, propagating from a distant source. Note that at this step, no assumption is made on the nature of the source. At each position X_i, a signal $P(X_i, t)$ is recorded.

This situation is illustrated on figure 3.8. P is a function of time t and space X_i. For a better understanding, we can draw a parallel between the situation described here and that of Young's slit experiment presented above:

- the radiating source (Σ on figure 3.8) is similar to the spatially extended source S has shown on figure 3.7.
- A set of two receivers (X_i, X_j) is similar to the two pinholes (P_i, P_j) has shown on figure 3.7.

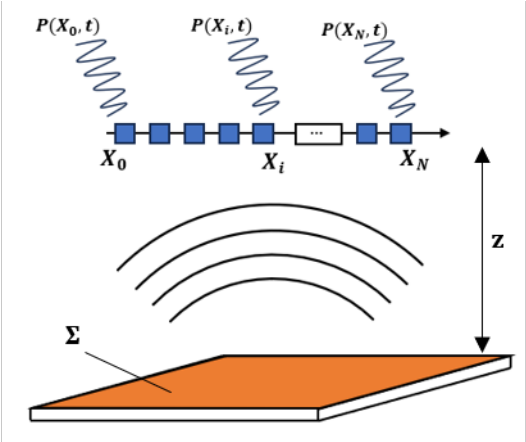

Figure 3.8: Illustration of a set of N receivers sensing over time a wave field propagating from a distance source Σ.

We are interested here in the spatial coherence of the wave field radiated from Σ and sensed on a parallel plane located at a distance z. As expressed previously, spatial coherence relates to the similarity of signals sensed at different points of space (i.e. different X_i) without delay between them. It can therefore be computed through the autocorrelation of P along the spatial dimension. Writing $\rho(\vec{\Delta}, t)$ autocorrelation function:

$$\rho(\vec{\Delta}, t) = \mathbb{E}\left[P\left(X_i, t\right) P^*\left(X_j, t\right)\right] = \left\langle P\left(X_i, t\right) P^*\left(X_j, t\right)\right\rangle \tag{3.7}$$

where (X_i, X_j) are a couple of points separated by a vector $\vec{\Delta}$, and * is the complex conjugate.

Note that $\rho(\vec{\Delta}, t)$ is a function of spatial lag $\vec{\Delta}$ (also called 'baseline') and time. That means that spatial coherence is defined at each instant of time. The time dependance of coherence can be illustrated thanks to the situation presented on figure 3.8. To do so, the source Σ must be considered has a sum of punctual radiators uniformally distributed on its surface. At a given time, only a part of these radiators effectively contributes to the wave field sensed at the observation plane. This part, that can be noted Σ_t acts as a source producing a wave field with a given spatial coherence. Thus, at each instant of time, a different portion of the source Σ (i.e. with a different extent and distribution of radiators) contributes to the wave field and so, at each instant of time, that leads to a different spatial coherence at the observation plan. Theoretically, spatial coherence defined at equation (3.7), can be estimated using a set of seafloor realisations. This estimate written $\hat{\rho}_s(\vec{\Delta}, t)$ is

$$\hat{\rho}_s(\vec{\Delta}, t) = \langle P\left(X_i, t\right) P^*\left(X_j, t\right)\rangle_s \tag{3.8}$$

$\langle\cdot\rangle_s$ being an average over seafloor realizations, the $\hat{}$ serving as a reminder that $\hat{\rho}_s(\vec{\Delta}, t)$ is an estimate of $\rho(\vec{\Delta}, t)$, and the subscript $_s$ mentioning that this estimate is obtained averaging over seafloor realizations.

In practice, we don't have access to different realizations of the seafloor. According to the situation illustrated on Fig. 3.8, and under the spatial ergodicity assumption, another way to estimate $\rho(\vec{\Delta}, t)$ would be an average over sensor pairs presenting a spatial lag $\vec{\Delta}$. Note that on this figure repartition of the X_i is one-dimensional, but the principle remains the same with a 3D repartition. Writing $\hat{\rho}_p(\vec{\Delta}, t)$ such an estimate and by expressing the vector $\vec{\Delta}$ as a function of the inter-sensor distance δ and a unit vector $\mathbf{i}$ such as $\vec{\Delta} = k\delta\mathbf{i}$:

$$\begin{aligned}\hat{\rho}_p(\vec{\Delta}, t) &= \langle P\left(X_i, t\right) P^*\left(X_j, t\right)\rangle_{\overrightarrow{X_iX_j}=\vec{\Delta}} \\ &= \frac{1}{N-k}\sum_{i=1}^{N-k} P\left(X_i, t\right) P^*\left(X_{i+k}, t\right)\end{aligned} \tag{3.9}$$

$\langle\cdot\rangle_{\overrightarrow{X_iX_j}=\vec{\Delta}}$ being an average over sensor pairs separated by a spatial lag $\vec{\Delta}$, the $\hat{}$ serving as a reminder that $\hat{\rho}_p(\vec{\Delta}, t)$ is an estimate of $\rho(\vec{\Delta}, t)$, and the subscript $_p$ mentioning that this estimate is obtained averaging over sensor pairs separated by a given spatial lag. In addition, we have chosen to represent the autocorrelation function in discrete form. This is because, in practice, the receivers have a certain surface area and it is impossible to access the coherence figure in its continuous form. It should be noted that averaging over a set of sensor pairs is not very different from

averaging over seafloor realizations. In fact, in the case of averaging over sensor pairs, each pair of sensors acquires signals from the same seafloor realisation but with different phase shifts, which can be likened to a new realisation, although the independence of the realisations is not reached.

However, in practice, for technical reasons, the number of reception sensors in the acquisition devices is limited and so the number of sensor pairs for a given spatial lag. So it is often necessary to perform a time average, under the temporal ergodicity assumption. Writing $\hat{\rho}_t(\vec{\Delta}, [t_1, t_2])$, the average of $\hat{\rho}_p(\vec{\Delta}, t$ over the time interval $[t_1, t_2]$:

$$\begin{aligned}
\hat{\rho}_t(\vec{\Delta}, [t_1, t_2]) &= \frac{1}{t_2 - t_1} \int_{t_1}^{t_2} \hat{\rho}_p(\vec{\Delta}, t) dt \\
&= \frac{1}{(t_2 - t_1)(N - k)} \int_{t_1}^{t_2} \sum_{i=1}^{N-k} P(X_i, t) P^*(X_{i+k}, t) \, dt \\
&= \frac{1}{(t_2 - t_1)(N - k)} \sum_{i=1}^{N-k} \int_{t_1}^{t_2} P(X_i, t) P^*(X_{i+k}, t) \, dt \\
&= \frac{1}{N - k} \sum_{i=1}^{N-k} \langle P(X_i, t) P^*(X_{i+k}, t) \rangle_{[t_1, t_2]}
\end{aligned} \tag{3.10}$$

$\langle \cdot \rangle_{[t_1, t_2]}$ being an ensemble over the time interval $[t_1, t_2]$. One can note that $\langle P(X_i, t) P^*(X_j, t) \rangle_{[t_1, t_2]}$ is an estimate of intercorrelation between $P(X_i, t)$ and $P^*(X_{i+k}, t)$ evaluated at a null temporal lag.

One word has to be said about time averaging. The idea behind time averaging is that, at each instant of time, a different portion of the scattering medium (i.e. a different realisation of the scattering medium) contributes to the received signal. For this equivalence between time averaging and averaging over realisations of the scattering medium to be completely rigorous, spatial coherence would have to be independent of time, but as expressed in the previous paragraph, this is not the case. So the size of the time window will have an effect on the coherence estimate and such an approximation is only possible for small time intervals $[t_1, t_2]$.

Equation (3.10) states that averaging the autocorrelation (along spatial dimension) function $\hat{\rho}(\vec{\Delta}, t)$ over a time interval $[t_1, t_2]$ is similar to the average of intercorrelation functions (over time dimension) between sensor pairs separated by a spatial lag $\vec{\Delta} = k\delta\mathbf{i}$ and estimated on the time interval $[t_1, t_2]$. This result is of particular interest for what follows, as it provides a link between how coherence is estimated in a practical way on real and simulated data (average of temporal intercorrelation on pairs of sensors) and how the analytic model of the chapter 4 is established (temporal average of spatial autocorrelation).

3.3 Practical Spatial coherence estimation

3.3.1 Computation procedure

We present in this section how spatial coherence is in practice estimated for our work. To do so, it is necessary to introduce the geometry of acquisition in the sonar case. Let's consider a down looking experimental device composed by a transmit element T insonifying seafloor and $\{P_1, P_2, P_3, P_4, P_5\}$ a set of receivers separated by a distance δ. The geometry is illustrated on figure 3.9(a). Please note that, for ease of illustration, the figure 3.9(a) shows an acquisition device whose receivers are distributed in a single dimension, but the considerations set out here remain valid for a 3D distribution.

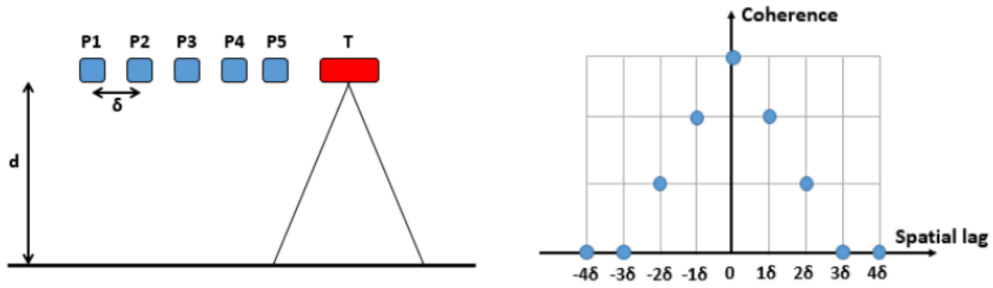

(a) (b)

Figure 3.9: (a) Schematic view of an acquisition device. T is a transmit element and P_i are the receivers - (b) Estimated spatial coherence for the set of inter-sensor distances allowed by the experimental device. Note the triangular shape of the function is just an example

As illustrated on this scheme and because receivers are not punctual, and the acquisition devices do not have an infinite number of receivers, it is only possible to measure the spatial coherence for some inter-sensor distances. On Figure 3.9(b), the coherence figure for the estimated inter-sensor distances is shown. For the device shown in Figure 3.9(a), only the spatial coherence for the spatial lag 0, 1δ, 2δ, 3δ, and 4δ can be estimated. The sensor pairs that can be used to estimate these coherences are summarised in the table 3.1.

In this work, and according to equation (3.10), the first step to estimate coherence is to compute intercorrelation between signals sensed at different position. This

Spatial Lag	Sensor Pairs
0	$\{P_1, P_1\}$, $\{P_2, P_2\}$, $\{P_3, P_3\}$, $\{P_4, P_4\}$, $\{P_5, P_5\}$
1δ	$\{P_1, P_2\}$, $\{P_2, P_3\}$, $\{P_3, P_4\}$, $\{P_4, P_5\}$
2δ	$\{P_1, P_3\}$, $\{P_2, P_4\}$, $\{P_3, P_5\}$
3δ	$\{P_1, P_4\}$, $\{P_2, P_5\}$
4δ	$\{P_1, P_5\}$

Table 3.1: Sensor pairs that can be used to estimate coherence at a given spatial lag.

intercorrelation is estimated over a time interval $[t_i, t_f]$:

$$\begin{aligned}\Gamma\left(X_i, X_j, [t_i, t_f]\right)(\tau) &= \langle P(X_i, t)P^*(X_j, t+\tau)\rangle_{[t_i, t_f]} \\ &= \int_{t_i}^{t_f} P(X_i, t)P^*(X_j, t+\tau)dt\end{aligned} \tag{3.11}$$

Because, we are interested by intercorelation estimated at a null temporal lag, one can note

$$\Gamma\left(X_i, X_j, [t_i, t_f]\right)(\tau = 0) = \int_{t_i}^{t_f} P(X_i, t)P^*(X_j, t)dt \tag{3.12}$$

As stated previously, it should be noted here that for the same spatial lag, several pairs of sensors can be used to estimate the coherence. Thus, the estimations computed on sensors separated by a given spatial lag can be averaged in order to reduce variability. Therefore, for a given spatial lag $\vec{\Delta}$, the coherence can be estimated by averaging magnitude of intercorrelations estimated between sensors pairs separated by a distance Δ. Back to the example of figure 3.9, pairs of sensor presenting a given spatial lag are summarized in table 3.1. The equation (3.13) summarizes this calculation process.

$$\hat{\rho}(\vec{\Delta}, [t_i, t_f]) = \langle |\Gamma\left(X_i, X_j, [t_i, t_f]\right)(\tau = 0)| \rangle_{||\overrightarrow{X_i X_j}||=\vec{\Delta}} \tag{3.13}$$

where $\vec{\Delta}$ is a spatial lag, $|\cdot|$ is the absolute value and $\langle\cdot\rangle_{||\overrightarrow{X_i X_j}||=\vec{\Delta}}$ is the mean over all sensor pairs separated by a vector $\vec{\Delta}$.

In the same way as for temporal coherence, it is often convenient to represent spacial coherence with its power normalised form defining thus the correlation coefficient (also called **degree of coherence**):

$$\hat{\mu}(\vec{\Delta}, [t_1, t_2]) = \left\langle \frac{|\Gamma_{X_i,X_j}([t_1, t_2], \tau = 0)|}{\sqrt{\Gamma_{X_i,X_i}([t_1, t_2], \tau = 0)\Gamma_{X_j,X_j}([t_1, t_2], \tau = 0)}} \right\rangle_{||\overrightarrow{X_i X_j}||=\vec{\Delta}} \tag{3.14}$$

Let's illustrate this computation procedure using HRLFSAS data introduced in section 2.3.4. On figure 3.10(a), intercorrelation matrix between all the sensor is represented. On this figure, sensors 0 to 7 corresponds to the eight receivers of the vertical antenna and sensors 8 to 15 to the eight receivers of the horizontal antenna. Each signal sensed by a receiver is correlated to all the other and the magnitude at null temporal lag is represented in the matrix. We can see that the maximum of correlation can be found on the diagonal of the matrix, that is the expected result because each sensor is perfectly correlated with itself. For pairs of distinct sensors, the level of coherence decreases. The correlation levels between the sensors on the vertical antenna (0 to 7) and those on the horizontal antenna (8 to 15) show very little correlation. This can be explained by the fact that the antennas are spatially distant from each other: the closer the sensors are, the higher the level of coherence. It is not very relevant to evaluate the coherence between two antennas as separated as the vertical and horizontal antennas of HRLFSAS. Let's concentrate instead on the coherence of the vertical antenna and that of the horizontal antenna. Figure 3.10(b), shows the evolution of coherence on the vertical antenna with respect of sensor lags (i.e. the number of sensors separating the two receivers used to compute the coherence estimate). Blue dots represent the estimates and red curve the mean value computed according to equation (3.14). The same curve is represented for the horizontal antenna on Figure 3.10(c). Modelling the size and the shape of these curves are the subject of this manuscript. We can already point out that the triangular shape that the coherence curve seems to have on the horizontal antenna can be predicted by the Van Cittert Zernike theorem presented in section 3.4.

In the following sections we present some characteristics of the coherence curves obtained using the calculation procedure presented here.

3.3.2 Correlation coefficient estimator

The Probability Density Function (PDF) of the magnitude of the correlation coefficient introduced above is given by [Miranda de Sá et al., 2009]:

$$P\left(|\hat{\mu}|;|\mu|,N\right) = 2(N-1)|\hat{\mu}|\left(1-|\mu|^2\right)^N\left(1-|\hat{\mu}|^2\right)^{N-2}\ {}_2F_1\left(N,N;1;|\mu|^2|\hat{\mu}|^2\right) \tag{3.15}$$

where N is the number of independent samples used for the estimation, μ is the expected correlation coefficient and ${}_2F_1$ is the Gauss hypergeometric function. It must be noted, that the formulation of the PDF as it is written in equation (3.15) is only valid for complex or analytic signals. Correlation coefficient probability density functions for real and normally distributed signals can be found in [Brown, 2017].

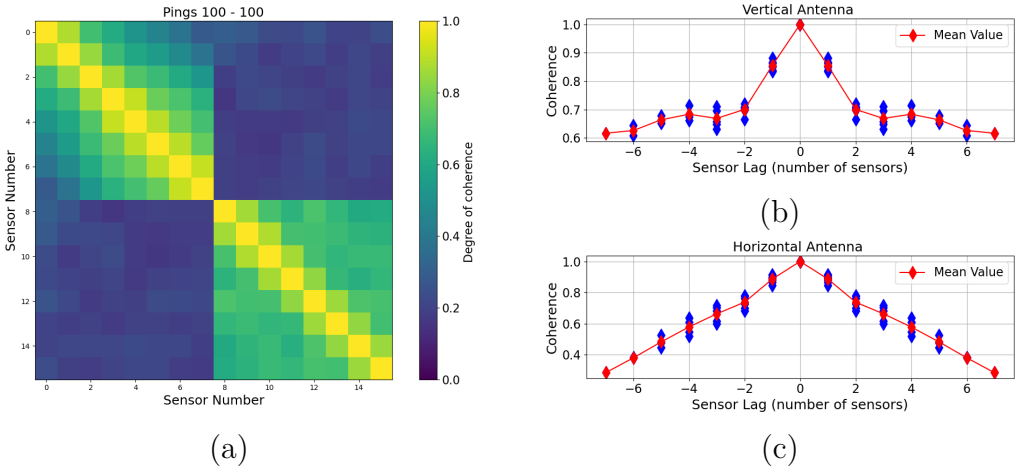

Figure 3.10: (a) Intercorrelation matrix. Sensors 0 to 7 corresponds to the 8 receivers of the vertical antenna and sensors 8 to 15 to the 8 receivers of the horizontal antenna - (b) Evolution of coherence on the vertical antenna with respect of sensor lags - (c) evolution of coherence on the horizontal antenna with respect of sensor lags. Rq: blue dots represent the estimates and red curve the mean value computed according to equation (3.14)

On the figure 3.11, the shape of the PDF is plotted for several values of expected correlation coefficient ($\mu = 0.1$ and $\mu = 0.8$) and several number of independent samples used for the estimation ($N = 20$, $N = 40$ and $N = 80$).

The analysis of these curves shows that:

- bias and standard deviation of the estimator are reduced when increasing N as expected by the estimation theory;
- bias and standard deviation of the estimator are higher for low expected coherence values μ

In order to illustrate bias for low expected coherence value, coherence estimates are computed using HRLFSAS data and represented on Figure 3.12. On this figure, low expected coherence are computed by correlating signals sensed on the vertical antenna with signals sensed on the horizontal antenna. As observed on figure 3.10, these signals are expected to be uncorrelated because the two antennas are far apart. On the contrary, high expected coherence are computed correlating signals sensed by receivers of the horizontal antenna with redundant sensors during sonar's trajectory.

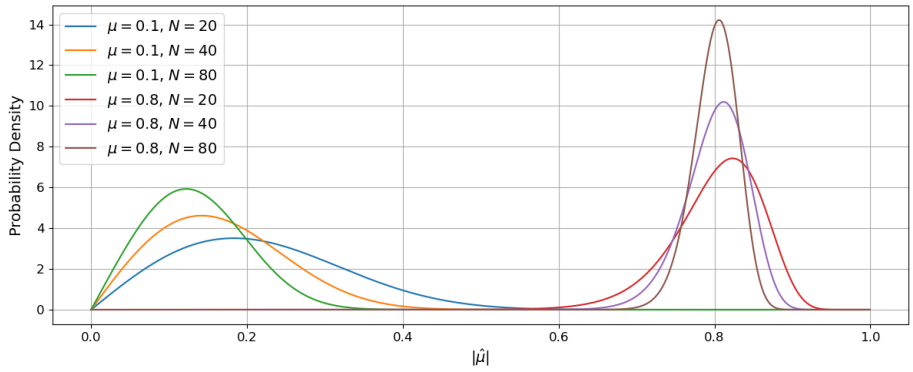

Figure 3.11: Probability density function of the correlation coefficient estimator

Because the sonar's trajectory is almost perfectly controlled (moving the sonar on rails), it is possible to select pair of sensors sensing at the same position, and so to expect a very high level of coherence. On figure 3.12(a), 100 samples are used to estimate coherence and on Figure 3.12(b), 600 samples are used. Comparing low expected coherence values computed with 100 and 600 samples, it must be noticed that the mean coherence (and thus the bias) strongly depends on the the number of samples used for the computation ($\hat{\mu} \approx 0.42$ with $N = 100$, whereas $\hat{\mu} \approx 0.24$ with $N = 600$). Because signals are expected to be uncorrelated, we can underline here the fact that **reducing the number of samples used for the estimation of coherence leads to an increase in the bias of the estimator**. By making the same comparison with high expected coherence values, we note that in this case the variation in the bias is much smaller than in the case of low expected coherence value ($\hat{\mu} \approx 0.85$ with $N = 100$, whereas $\hat{\mu} \approx 0.84$ with $N = 600$). Thus, one can underline here the fact that **the bias of high expected coherence values estimates is less affected by the number of samples used for the computation**. However, one need to consider the mean coherence value $\hat{\mu} \approx 0.85$. Indeed, because these coherence estimates are computed using pair of sensors sensing at the same position, theoretically a degree of coherence of 1 is expected. It will be shown in section 3.3.4 that this decrease of coherence is linked to the Signal to Noise Ratio (SNR).

3.3.3 Influence of the length of the signal

In this section, we focus on the residual bias that affects the coherence estimate for low or zero expected coherence levels. This bias, introduced in the study of the

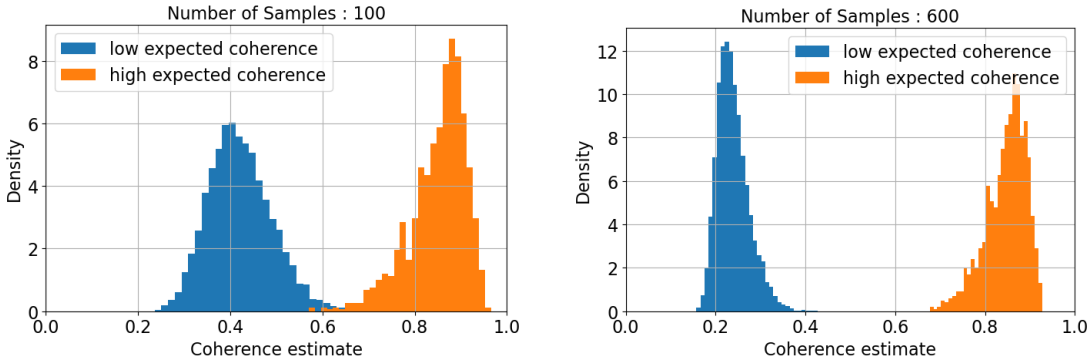

(a) (b)

Figure 3.12: Distribution of coherence estimates for low and high expected coherence levels - (a) 100 samples are used to estimate coherence - (b) 600 samples are used to estimate coherence

estimator (see Figure 3.11) and illustrated using HRLFSAS data (see Figure 3.12) affects the coherence estimates calculated for pairs of sensors that are far apart. We saw in the previous section that one way for reducing this bias is to increase the number of independent samples N used to estimate the correlation. This point is illustrated on Figure 3.13. On these figures, different bias and residual coherence are compared:

- 'PDF' curve represents the theoretical bias computed through the PDF of the estimator (see equation (3.15)) as a function of number of sample N used for the computation:

  $$bias = \mathbb{E}\left[|\hat{\mu}|\left(|\mu|, N\right)\right] - |\mu|$$

  And because we are interested on bias that affects the coherence estimate for zero expected coherence levels ($|\mu| = 0$)

  $$bias = \mathbb{E}\left[|\hat{\mu}|\left(|\mu| = 0, N\right)\right] - |\mu|$$

- 'Simulation' curve represents the estimated correlation coefficient between two random noises generated with N independent samples

- 'Exprimental Data' curve represents the mean value of measured coherence estimates on HRLFSAS data using sensor pairs that are far apart from each other (null expected coherence)

We can see on figure 3.13(a) that curves representing the evolution of theoretical bias and the measured correlation coefficient between two random noises with respect of independent samples N are the same. On the contrary, the bias observed in the HRLFSAS data is slightly higher. That can be explained by the fact, that HRLFSAS signals are oversampled by a factor of around 2.5. That means that, for a given signal length, the number of independant sample allowing the estimation of the coherence is lower than the number of samples in the signal. Results taking into account this oversampling of HRLFSAS data are represented on figure 3.13(b) and show good agreement between the three plotted bias.

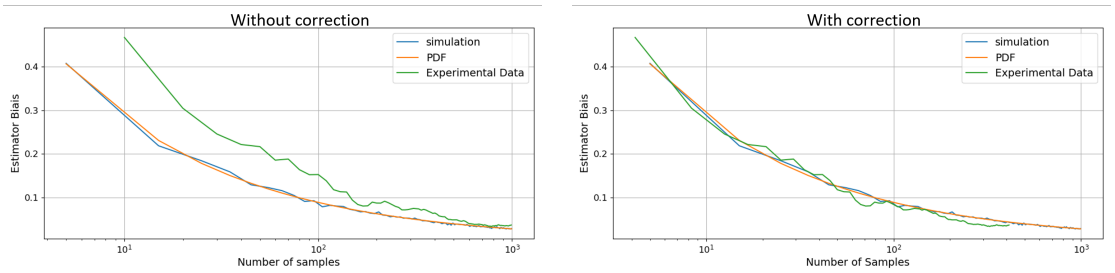

(a) (b)

Figure 3.13: Evolution of the bias of the coherence estimator as a function of the number of independent samples N. 'PDF' curve represents the theoretical bias computed through the PDF of the estimator. 'Simulation' curve represents the measured degree of correlation between two random noises. 'Experimental Data' curve represents the mean value of measured coherence estimates on HRLFSAS data using sensor pairs that are far apart from each other. - (a) without taking into account HRLFSAS oversampling - (b) After compensation for HRLFSAS oversampling

3.3.4 Influence of the signal to noise ratio

In section 3.3.2, we pointed out that the degree of coherence for a zero inter-sensor distance (which is theoretically 1) is in practice reduced as a function of the signal to noise ratio.

Let's consider two signals s_1 and s_2 affected by two independent but identically

distributed noises n_1 and n_2 such as:

$$\begin{aligned} s'_1 &= s_1 + n_1 \\ s'_2 &= s_2 + n_2 \end{aligned} \tag{3.16}$$

By definition (equation (3.7)), the degree of coherence between signals s'_1 and s'_2 is given by:

$$\mu'_{12} = \frac{\langle s'_1 s'_2 \rangle}{\sqrt{\langle s'_1 s'_1 \rangle \langle s'_2 s'_2 \rangle}} \tag{3.17}$$

and the degree of coherence between signals s_1 and s_2 is given by:

$$\mu_{12} = \frac{\langle s_1 s_2 \rangle}{\sqrt{\langle s_1 s_1 \rangle \langle s_2 s_2 \rangle}} \tag{3.18}$$

As the noises are independent:

$$\begin{aligned} \langle s'_1 s'_2 \rangle &= \langle (s_1 + n_1)(s_2 + n_2) \rangle \\ &= \langle s_1 s_2 + s_1 n_2 + s_2 n_1 + n_2 n_1 \rangle \\ &= \langle s_1 s_2 \rangle \end{aligned} \tag{3.19}$$

Similarly,

$$\begin{aligned} \langle s'_1 s'_1 \rangle &= \langle s_1 s_1 \rangle + \langle n_1 n_1 \rangle \\ \langle s'_2 s'_2 \rangle &= \langle s_2 s_2 \rangle + \langle n_2 n_2 \rangle \end{aligned} \tag{3.20}$$

Using 3.19 and 3.20, degree of coherence between s'_1 and s'_2 can be written:

$$\mu'_{12} = \frac{\langle s_1 s_2 \rangle}{\sqrt{(\langle s_1 s_1 \rangle + \langle n_1 n_1 \rangle)(\langle s_2 s_2 \rangle + \langle n_2 n_2 \rangle)}} \tag{3.21}$$

Assuming that mean square level of signals are equals $\langle s_1 s_1 \rangle = \langle s_2 s_2 \rangle = \sigma_s^2$ and likewise for noises components, $\langle n_1 n_1 \rangle = \langle n_2 n_2 \rangle = \sigma_n^2$, and noting $SNR = \frac{\sigma_s^2}{\sigma_n^2}$ the

signal to noise ratio:

$$\begin{aligned}
\mu'_{12} &= \frac{\langle s_1 s_2 \rangle}{\sqrt{\sigma_s^4 + \sigma_n^4 + 2\sigma_s^2\sigma_n^2}} \\
&= \frac{\langle s_1 s_2 \rangle}{\sigma_s^2} \frac{1}{1 + \frac{2\sigma_n^2}{\sigma_s^2} + \frac{\sigma_n^4}{\sigma_s^4}} \\
&= \frac{\langle s_1 s_2 \rangle}{\sigma_s^2} \frac{1}{1 + \frac{2}{SNR} + \frac{1}{SNR^2}} \\
&= \frac{\langle s_1 s_2 \rangle}{\sigma_s^2} \left(\frac{SNR}{1 + SNR} \right) \\
&= \mu_{12} \left(\frac{SNR}{1 + SNR} \right)
\end{aligned} \tag{3.22}$$

Figure 3.14 shows the evolution of the degree of coherence depending on the signal to noise ratio. This evolution is presented for different value of expected coherence μ_{12}. Remaining that on Figure 3.12, a mean coherence value $\mu'_{12} \approx 0.85$ was measured, whereas, the expected coherence was $\mu_{12} = 1$ (sensors pairs were expected collocated). Thanks to Figure 3.14 an SNR of 5.6dB can be deduced for HRLFSAS signals.

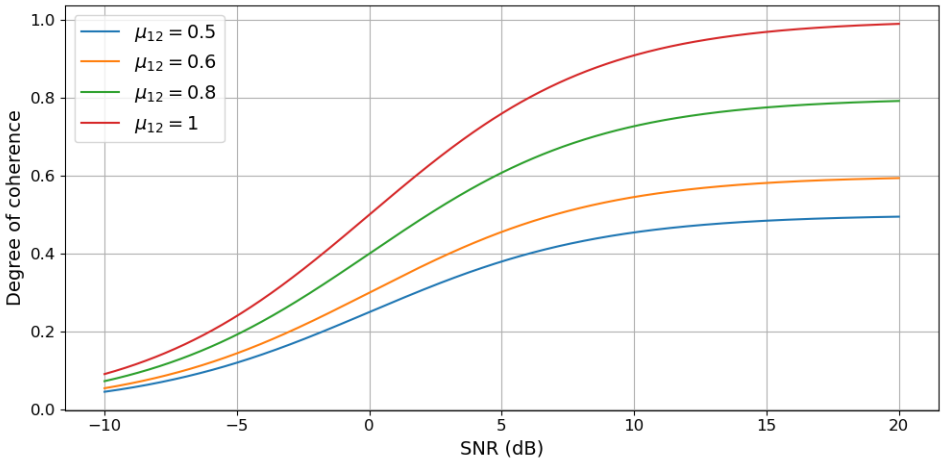

Figure 3.14: Evolution of the degree of coherence depending on the signal to noise ratio for several values of expected correlation coefficient μ. Red curve corresponds to the decrease in coherence that would be observed in the case of co-located sensors.

3.4 The Van Cittert Zernike theorem and its application to the acoustic field

The Van Cittert Zernike theorem was developed in the field of statistical optics. This theorem predicts spatial coherence of a wave field produced by an incoherent source. In this section, the theorem and its assumptions are introduced, as well as its extension to acoustic sources.

3.4.1 The Van Cittert Zernike theorem

The Van Cittert Zernike (VCZ) theorem, was introduced and developed at the end of the 30s' [Van Cittert, 1934][Zernike, 1938]. Other works have subsequently presented extensions or reformulations of the theorem [Wolf and Born, 1955][Born et al., 1999]. In [Goodman, 1985], the author presents an discussion about VCZ theorem. The main lines of the derivation of this theorem are summarised here.

Let's consider an incoherent source Σ composed by a great number of statistically independent radiating elements $\bar{X}$. At a large distance z, two observating points Q_1 and Q_2 are defined. The observation plane containing Q_1 and Q_2 is assumed to be parallel to the source Σ and at a distance z from it. The geometry of the problem and its characteristic dimensions are shown in 3.15.

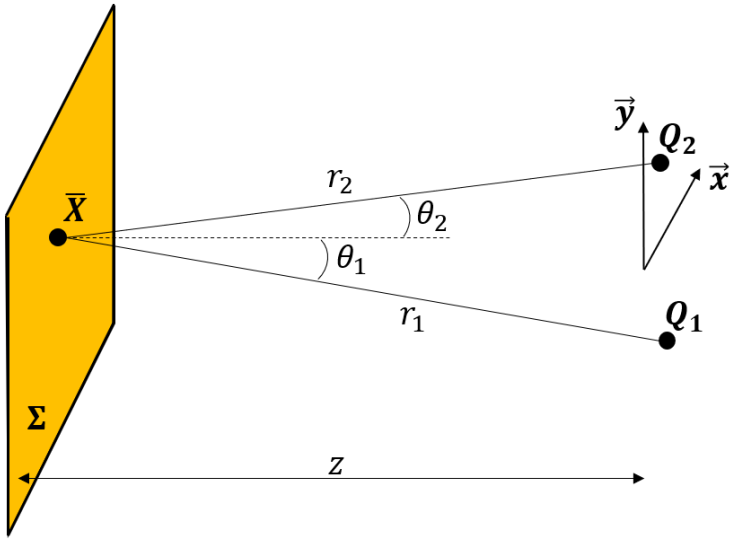

Figure 3.15: VCZ geometry

As stated in equation (3.7) the coherence is given by :

$$\hat{\rho}(Q_1, Q_2, \tau = 0) = \langle s\left(Q_1, t\right) \cdot s^*\left(Q_2, t\right) \rangle \tag{3.23}$$

where $s\left(Q_1, t\right)$ is the signal sensed at position Q_1, $s\left(Q_2, t\right)$ is the signal sensed at position Q_2, * is the complex conjugate and $< \cdot >$ is an ensemble over source realisations.
Signal sensed at position Q_1 is the sum over all contributions $\bar{X}$ of Σ and is given by:

$$s\left(Q_1, t\right) = \int_\Sigma \frac{\chi(\theta_1)}{r_1} s_0\left(\bar{X_1}, t - \frac{r_1}{c}\right) d\bar{X_1} \tag{3.24}$$

where r_1 is the distance between contribution $\bar{X_1}$ of Σ and point Q_1, θ_1 is the angle between the normal direction of Σ and the direction of $\overrightarrow{\bar{X_1}Q_1}$, χ is the directional amplitude pattern produced by Σ and $s_0\left(\bar{X_1}, t - \frac{r_1}{c}\right)$ is the elementary signal produced at position $\bar{X_1}$ and delayed by $\frac{r_1}{c}$.

Similarly,

$$s\left(Q_2, t\right) = \int_\Sigma \frac{\chi(\theta_2)}{r_2} s_0\left(\bar{X_2}, t - \frac{r_2}{c}\right) d\bar{X_2} \tag{3.25}$$

and

$$\begin{aligned}
\hat{\rho}(Q_1, Q_2, \tau = 0) &= \langle s\left(Q_1, t\right) \cdot s^*\left(Q_2, t\right) \rangle \\
&= \left\langle \int_\Sigma \int_\Sigma \frac{\chi(\theta_1)}{r_1} \frac{\chi(\theta_2)}{r_2} s_0\left(\bar{X_1}, t - \frac{r_1}{c}\right) s_0^*\left(\bar{X_2}, t - \frac{r_2}{c}\right) d\bar{X_1} d\bar{X_2} \right\rangle \\
&= \int_\Sigma \int_\Sigma \frac{\chi(\theta_1)}{r_1} \frac{\chi(\theta_2)}{r_2} \left\langle s_0\left(\bar{X_1}, t - \frac{r_1}{c}\right) s_0^*\left(\bar{X_2}, t - \frac{r_2}{c}\right) \right\rangle d\bar{X_1} d\bar{X_2} \\
&= \int_\Sigma \int_\Sigma \frac{\chi(\theta_1)}{r_1} \frac{\chi(\theta_2)}{r_2} \hat{\rho}\left(\bar{X_1}, \bar{X_2}, \tau = \frac{r_2 - r_1}{c}\right) d\bar{X_1} d\bar{X_2}
\end{aligned} \tag{3.26}$$

As well as the expression $\hat{\rho}(Q_1, Q_2, \tau = 0)$ represents the correlation of the field sensed at positions Q_1 and Q_2 and evaluated at a null temporal lag, $\hat{\rho}\left(\bar{X_1}, \bar{X_2}, \tau = \frac{r_2 - r_1}{c}\right)$ represents represents the correlation of the field sensed at positions $\bar{X_1}$ and $\bar{X_2}$ and evaluated at a $\tau = \frac{r_2 - r_1}{c}$ temporal lag.

Assuming narrow band signal, meaning that time difference $\frac{r_2 - r_1}{c}$ is shorter than coherence time (see part 3.1), it is shown in [Goodman, 1985] that :

$$\hat{\rho}\left(\bar{X_1}, \bar{X_2}, \tau = \frac{r_2 - r_1}{c}\right) = \hat{\rho}\left(\bar{X_1}, \bar{X_2}, \tau = 0\right) e^{-j\frac{2\pi}{\lambda}(r_2 - r_1)} \tag{3.27}$$

Moreover, assuming that Σ is an incoherent source,

$$\hat{\rho}\left(\bar{X_1}, \bar{X_2}, \tau = 0\right) = \begin{cases} I(\bar{X}) & \text{if } \bar{X_1} = \bar{X_2} \\ 0 & \text{else.} \end{cases} \tag{3.28}$$

where $I(\bar{X})$ is the intensity radiated by Σ at point $\bar{X}$.

Using equations (3.27) and (3.28), equation (3.26) becomes:

$$\hat{\rho}(Q_1, Q_2, \tau = 0) = \int_{\Sigma} \frac{\chi(\theta_1)}{r_1} \frac{\chi(\theta_2)}{r_2} I(\bar{X}) e^{-j\frac{2\pi}{\lambda}(r_2 - r_1)} d\bar{X} \tag{3.29}$$

Assuming that :

- distance z between source and the observation area is large comparing to other distances:
$$\frac{1}{r_1} \cdot \frac{1}{r_2} \approx \frac{1}{z^2} \tag{3.30}$$
- observation angles are small
$$\chi(\theta_1) \approx \chi(\theta_2) \approx 1 \tag{3.31}$$

equation (3.29) becomes:

$$\hat{\rho}(Q_1, Q_2, \tau = 0) = \int_{\Sigma} \frac{I(\bar{X})}{z^2} e^{-j\frac{2\pi}{\lambda}(r_2 - r_1)} d\bar{X} \tag{3.32}$$

Finally, we assume that points Q_1 and Q_2 lie in a parallel plan towards the source Σ as represented on Figure 3.15. Noting (x, y, z) coordinates of point $\bar{X}$, $(x_1, y_1, 0)$ the coordinates of point Q_1, $(x_2, y_2, 0)$ the coordinates of point Q_2 and with respect of large distance z, distances r_1 and r_2 can be written:

$$\begin{aligned} r_1 &= \sqrt{z^2 + (x_1 - x)^2 + (y_1 - y)^2} \approx z + \frac{(x_1 - x)^2 + (y_1 - y)^2}{2z} \\ r_2 &= \sqrt{z^2 + (x_2 - x)^2 + (y_2 - y)^2} \approx z + \frac{(x_2 - x)^2 + (y_2 - y)^2}{2z} \end{aligned} \tag{3.33}$$

and so equation (3.32) becomes

$$\hat{\rho}(Q_1, Q_2, \tau = 0) = \frac{e^{-j\Psi}}{z^2} \int_{\Sigma} I(x, y) e^{-j\frac{2\pi}{\lambda \cdot z}((x_2 - x_1) \cdot x + (y_2 - y_1) \cdot y)} dx dy \tag{3.34}$$

with $\Psi = \frac{\pi}{\lambda \cdot z}\left((x_2^2 + y_2^2)2 - (x_1^2 + y_1^2)\right)$ Expression (3.34) is the van Cittert Zernike theorem. It is often presented on its normalized form:

$$\hat{\mu}(Q_1, Q_2) = \frac{e^{-j\Psi}\int_\Sigma I(x,y)e^{-j\frac{2\pi}{\lambda \cdot z}((x_2-x_1)\cdot x+(y_2-y_1)\cdot y)}dxdy}{\int_\Sigma I(x,y)dxdy} \tag{3.35}$$

The Van Cittert Zernike theorem presented mathematically either on equations (3.34) and (3.35) states that **spatial coherence is proportional to the 2D Fourier transform of the spatial intensity distribution produced by an incoherent source**. In [Goodman, 1985], the author points out that the mathematical expression of the VCZ theorem linking coherence to the intensity distribution through an incoherent source is the same as that links a diffraction pattern to the aperture of coherent source. In other words, mathematically the spatial intensity distribution is to spatial coherence what the aperture of a source is to its radiation pattern. This result is of great interest and explains very well the phenomena observed in the Young's slit experiment. Indeed as we saw in part 3.2, one can notice in equations (3.34) and (3.35) that:

- Spatial coherence depends on spatial extension of the source Σ. The wider the spatial extension of the source, the narrower the coherence length.
- Spatial coherence evolves with respect to the distance z between the source and the observation plan: it is narrow, very close to the source and becomes wider as the distance between the source and the observation plan increases.

3.4.2 Application to an acoustic field

Despite of the clear interest of the VCZ as stated above, its application to the sonar domain is not straight forward given that acoustic sources produce coherent acoustic field. However, under some assumptions, it is applicable to an acoustic field scattered by an incoherent medium [Mallart and Fink, 1991]. The main idea is that considering an acoustic source insonifying an incoherent medium (seafloor for example), at any instant of time, the scattered field is produced by a part of a seafloor called 'isochronous volume' in [Fink and Cardoso, 1984]. This volume acts as a source, and if the sediment is incoherent (i.e. scattering medium is composed by a great number of scatterers that are randomly distributed), this source can be considered incoherent and thus some optic results applied. However, one must be aware of a major difference that is the dependence of time. **Indeed, shape, size and statistical properties of the 'isochronous volume' depends on the one hand on the transmitted energy diagram but also on the intersection between transmitted beam**

and seafloor. This intersection depends on depth, and so on time. Therefore properties of equivalent source, and so coherence of scattered field, vary on time, which means that the VCZ results are significantly different. The broad outlines of the calculation of [Mallart and Fink, 1991] are given here.

Let's consider an acoustic source of aperture δ, facing an incoherent seafloor Σ and a set of two receivers Q_1 and Q_2 as illustrated on figure 3.16.

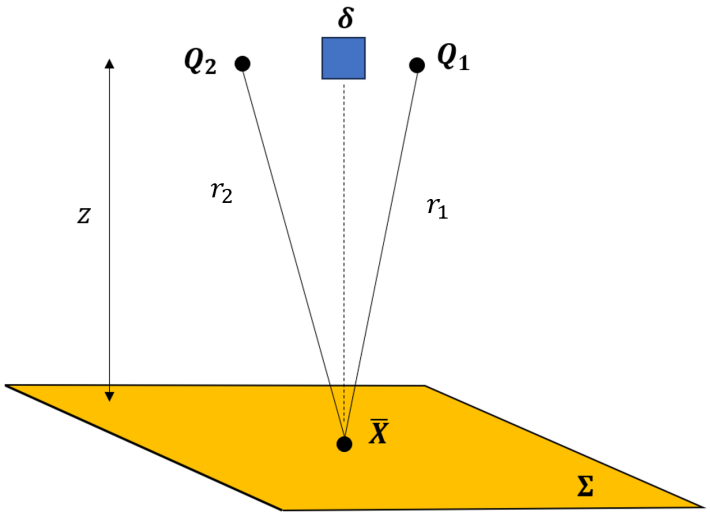

Figure 3.16: VCZ geometry

The incident pressure field sensed at position $\bar{X}$ of Σ and produced by such a transmit source can be written:

$$\chi(\bar{X}) = \int_{\delta} \delta(X_T) \frac{e^{j2\pi f R_T/c}}{R_T} dX_T \text{ with } R_T = ||\bar{X} X_T|| \tag{3.36}$$

where δ is the physical aperture of the transmit source.

The contribution to the scattered pressure field produced by a scatterer $\bar{X}$ of Σ and sensed at position Q_1 can be written:

$$s_{\bar{X}}(Q_1) = \chi(\bar{X})\sigma(\bar{X}) \frac{e^{j2\pi f R_{Q_1}(\bar{X})}}{R_{Q_1}(\bar{X})} \tag{3.37}$$

where σ is the scattering function, and $R_{Q_1}(\bar{X}) = ||\bar{X}Q_1||$. The pressure scattered field produced by the whole medium Σ is obtained summing over all scattering elements and given by:

$$s(Q_1) = \int_{\Sigma} \chi(\bar{X})\sigma(\bar{X}) \frac{e^{j2\pi f R_{Q_1}(\bar{X})}}{R_{Q_1}(\bar{X})} d\bar{X} \tag{3.38}$$

As stated in equation (3.8) the spatial coherence of the field sensed at positions Q_1 and Q_2 could be estimated by :

$$\begin{aligned} \hat{\rho}(Q_1, Q_2) &= \langle s\left(Q_1\right) \cdot s^*\left(Q_2\right) \rangle \\ &= \int_{\Sigma}\int_{\Sigma} \chi(\bar{X}_1)\chi^*(\bar{X}_2) \left\langle \sigma(\bar{X}_1)\sigma(\bar{X}_2) \right\rangle \frac{e^{j2\pi f\left(R_{Q_1}(\bar{X}_1) - R_{Q_2}(\bar{X}_2)\right)}}{R_{Q_1}(\bar{X}_1)R_{Q_2}(\bar{X}_2)} d\bar{X}_1 d\bar{X}_2 \end{aligned} \tag{3.39}$$

Assuming an incoherent seafloor

$$\left\langle \sigma(\bar{X}_1)\sigma(\bar{X}_2) \right\rangle = \sigma_0 \delta(\bar{X}_2 - \bar{X}_1) \tag{3.40}$$

where δ is a Dirac function and σ_0 a constant scattering factor. Under this assumption, equation (3.39) reduces to:

$$\hat{\rho}(Q_1, Q_2) = \sigma_0 \int_{\Sigma_1} \left|\chi(\bar{X})\right|^2 \frac{e^{j2\pi f\left(R_{Q_1}(\bar{X}) - R_{Q_2}(\bar{X})\right)}}{R_{Q_1}(\bar{X})R_{Q_2}(\bar{X})} d\bar{X} \tag{3.41}$$

Assuming that depth z is greater than other distances:

$$\frac{1}{R_{Q_1}(\bar{X})} \frac{1}{R_{Q_2}(\bar{X})} \approx \frac{1}{z^2} \tag{3.42}$$

and writing $\bar{X} = (x, y, z)$, $Q_1 = (x_1, y_1, 0)$ and $Q_2 = (x_2, y_2, 0)$ equation (3.46) becomes

$$\hat{\rho}(Q_1, Q_2) = \frac{\sigma_0}{z^2} e^{-j\frac{2\pi}{\lambda z}\left((x_2^2 + y_2^2) - (x_1^2 - y_1^2)\right)} \int_{\Sigma_1} \left|\chi(\bar{X})\right|^2 e^{-j\frac{2\pi}{\lambda z}((x_2 - x_1)\cdot x + (y_2 - y_1)\cdot y)} dxdy \tag{3.43}$$

This equation is very similar in its formulation to equation (3.34) and in this case the coherence is proportional to the Fourier transform of the intensity distribution on the seafloor. Note that this intensity distribution is a function of the radiation pattern of the transmitting antenna. In order to probe further, let's apply the assumption on depth z to equation (3.36). In such a case, incident pressure field becomes:

$$\chi(\bar{X}) = \frac{e^{j\frac{2\pi f z}{c}(1 + \bar{X}^2)}}{z} \int_{\delta} \delta(X_T) e^{j\frac{\pi f}{zc}(X_T \bar{X} + X_T^2)} dX_T \tag{3.44}$$

and

$$\left|\chi(\bar{X})\right|^2 = \frac{1}{z^2}\int_{\delta_1}\int_{\delta_2}\delta(X_{T1})\delta(X_{T2})e^{\frac{j\pi f}{zc}\left(X_{T1}-X_{T2}+\bar{X}\left(X_{T1}^2-X_{T2}^2\right)\right)}dX_{T1}dX_{T2} \tag{3.45}$$

It is shown in [Mallart and Fink, 1991] that inserting equation (3.45) into equation (3.43) spatial coherence reduces to:

$$\hat{\rho}(Q_1,Q_2) = \frac{\sigma_0}{z^4}R_\delta(x_1-x_2,y_1-y_2) \tag{3.46}$$

where R_γ is the autocorrelation of the aperture γ. Let's illustrate this result using HRLFSAS data. Observed coherence on the horizontal antenna is represented on Figure 3.17(a). This figure is an extension of figure 3.10(c) computed using pairs of sensors with greater spatial diversity, so that the entire coherence figure can be observed. This coherence figure has a triangular shape with a base $L_c \approx 0.50cm$ long. According to the VCZ theorem, the antenna that would produce such a coherence would have a linear aperture of length $L = L_c/2 \approx 0.25m$. This result can be compared with the aperture actually used by the HRLFSAS system. To characterise this aperture, it is possible to use a strong scatterer in the scene. The contribution of this bright spot acquired along the sonar trajectory is shown in the blue box in Figure 3.17(b). Based on the maximum of the signal, this contribution trace is automatically extracted and plotted as a function of the bearing angle on Figure 3.17(c). By approximating the aperture of the beam by a parabola, it is possible to estimate the -3dB beamwidth at a value of approximately $2\theta_{-3dB} \approx 25°$. Considering a narrow band signal with a central frequency $f_0 = 12kHz$, the linear antenna that would produce such a beam should have a length of $25cm$ that is in accordance with the theoretical aperture deduced from coherence figure applying the VCZ theorem. This way of estimating transmit beam shape applying VCZ theorem was also performed in [Geiman et al., 2000].

3.5 Spatial coherence application: the micronavigation estimation

As expressed in part 2.2.2, in order to coherently integrate data sensed over the trajectory, SAS systems need to accurately estimate the displacement of the antenna in order to produce well focussed imagery as any phase error in the processing result in image defocussing [Cook and Brown, 2009]. In practice, there are three important shifts or directions to consider. These shifts are illustrated on 3.18:

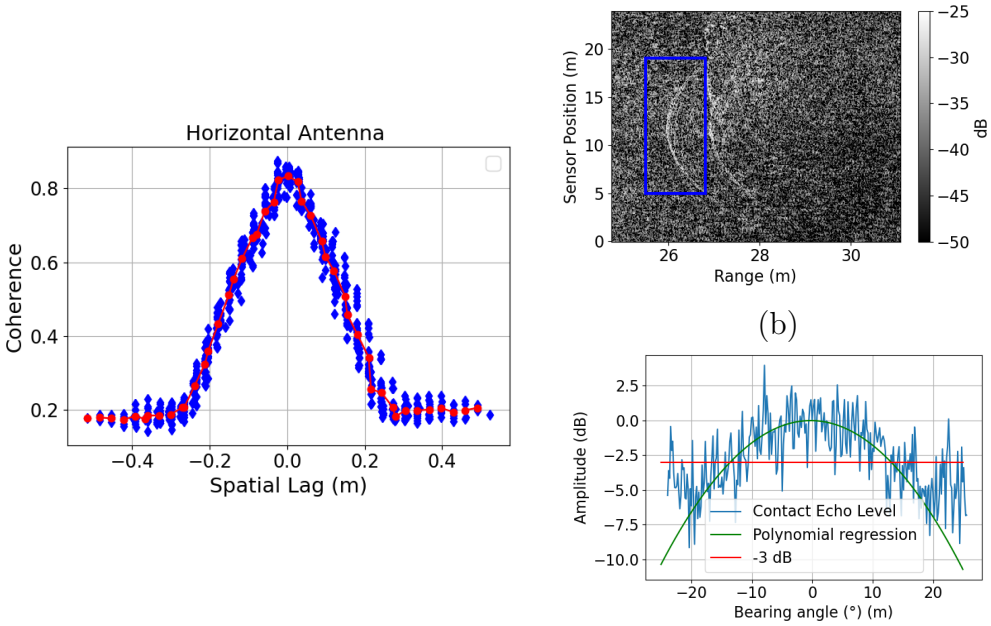

(a) (b) (c)

Figure 3.17: (a)Observed coherence on the horizontal antenna Blue dots reprensents the estimates and red curve the mean value - (b) Natural sonar image of the scene. Blue box highlights contribution of a strong scatterer used for beam shape estimation. - (c) Extracted contribution of a strong scatterer

- sway Δ_x (translation transversal of the ship's direction of travel)
- yaw Δ_θ (rotation around the vertical axis)
- surge Δ_y (translation in the ship's direction of travel)

We have already seen that a DVL Aided INS navigation system as commonly used in AUVs, does not allow the displacement of the antenna to be estimated to a sufficient accuracy. To deal with this point, displaced phase center (DPC) motion estimation has been widely studied. This method uses the correlation properties of the signals between two successive pings to estimate the offset between the two antennas. The basic idea is that if we transmit using a transmitter/receiver pair at a given position and then transmit a second time at the same position with another pair, assuming that the environment has not changed, the signals to be received are exactly the same. However, if the position of the two transmit-receiver pairs is not

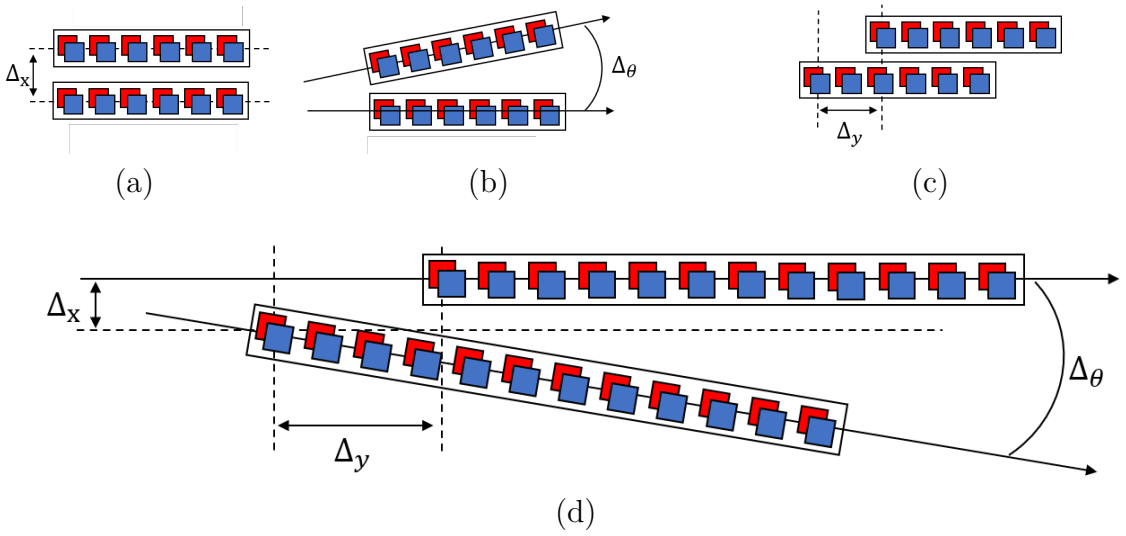

Figure 3.18: Illustration of the three shifts estimated by DPCA method: (a) Across track displacement Δ_y - (b) Yaw Δ_θ (An across track shift is added for clarity of the scheme) - (c) Along trach displacement Δ_x (An across track shift is added for clarity of the scheme) - (d) Combination of the three shifts.

exactly the same, the two signals will appear slightly different and this difference can be used to estimate the relative position between the two phase centres. This loss in similarity is a consequence of temporal and spatial coherence of the seafloor. Estimating the latter from the measured signals can therefore be used to estimate the three displacements mentioned above. Let's have a look how these three shifts can be estimated.

Sway - Across track displacement

Let's consider an across track shift between antenna as represented on Figure 3.18(a). In such a case, one of the two antennas is closer to the area to be imaged than the other. Therefore, correlating the sensors from one antenna with the same sensors from the other antenna will result in a shift in the cross-correlation peak that is a function of the path difference between the two antennas and therefore of the spatial offset. Such a modification of the cross-correlation function refers to temporal coherence as described in part 3.1. If the system is broadband, the cross-correlation peak is fine enough to estimate the transverse offset using this information. A constant sway shift between the two antenna results in a constant time shift.

Yaw

Let's consider a rotation around the vertical axis of one antenna relative to the other one as represented on Figure 3.18(b). Please note that on Figure 3.18(b), an across track shift it also represented. In the same way as for estimating the sway, correlating the sensors from one antenna with the same sensors from the other antenna will result in a time shift, but in this case this time shift is not constant over all sensor pairs. Indeed, a yaw angle between the two antenna results in a proportionality coefficient between observed time shifts.
Thus, a linear regression on the time shifts observed by sensor pairs allow to deduce sway and then yaw angle between the two antenna.

Surge - Along-track displacement

Let's consider an along-track shift between antenna as represented on Figure 3.18(c). Please note that on Figure 3.18(c) an across track shift it also represented. In order to estimate along-track displacement, the idea is to compute the correlation between phase centers at ping i with the phase centers at ping j. If the device has not moved by more than one PCA antenna length, phase centres overlap between the two pings, so it is possible to find maximum coherence between the phase centres of the two successive pings. The separation between these overlapping phase centers (i.e. those with the highest coherence), represents the along-track displacement. If we take the example shown in 3.18(c), PCA pairs presenting the highest level of coherence would be (3,1), (2,4), (3,5) and (4,6). Thus it is possible to deduce that between these two pings the antenna has advanced by a distance corresponding to the distance separating two phase centres. Knowing the physical separation of the antenna's sensors, it is easy to deduce the surge.

This principle is illustrated here by the use of the HRLFSAS data introduced in section 2.3.4. Figure 3.19 shows coherence estimates of all sensor pairs of the horizontal antenna of HRLFSAS between different pings. On image *Pings 100 - 100*, each sensor is correlated with itself and thus, maximum coherence values are observed on the diagonal of the matrix. For two successive pings (*Pings 99 - 100* and *Pings 100 - 101*), the antenna has moved, and so the maximum of coherence is no longer on the diagonal of the matrix, but it is offset by a number of sensors corresponding to the longitudinal displacement of the antenna. In the extreme case of pings separated by 4 recurrences (*Pings 100 - 96* and *Pings 100 - 104*), there remains only two co-located phase centres left (the last of ping 100 with the first of ping 104).

To explain how to estimate displacement, Figure 3.20 represents, for two successive pings (Ping 100 and Ping 101), the measured coherence between each phase centers of

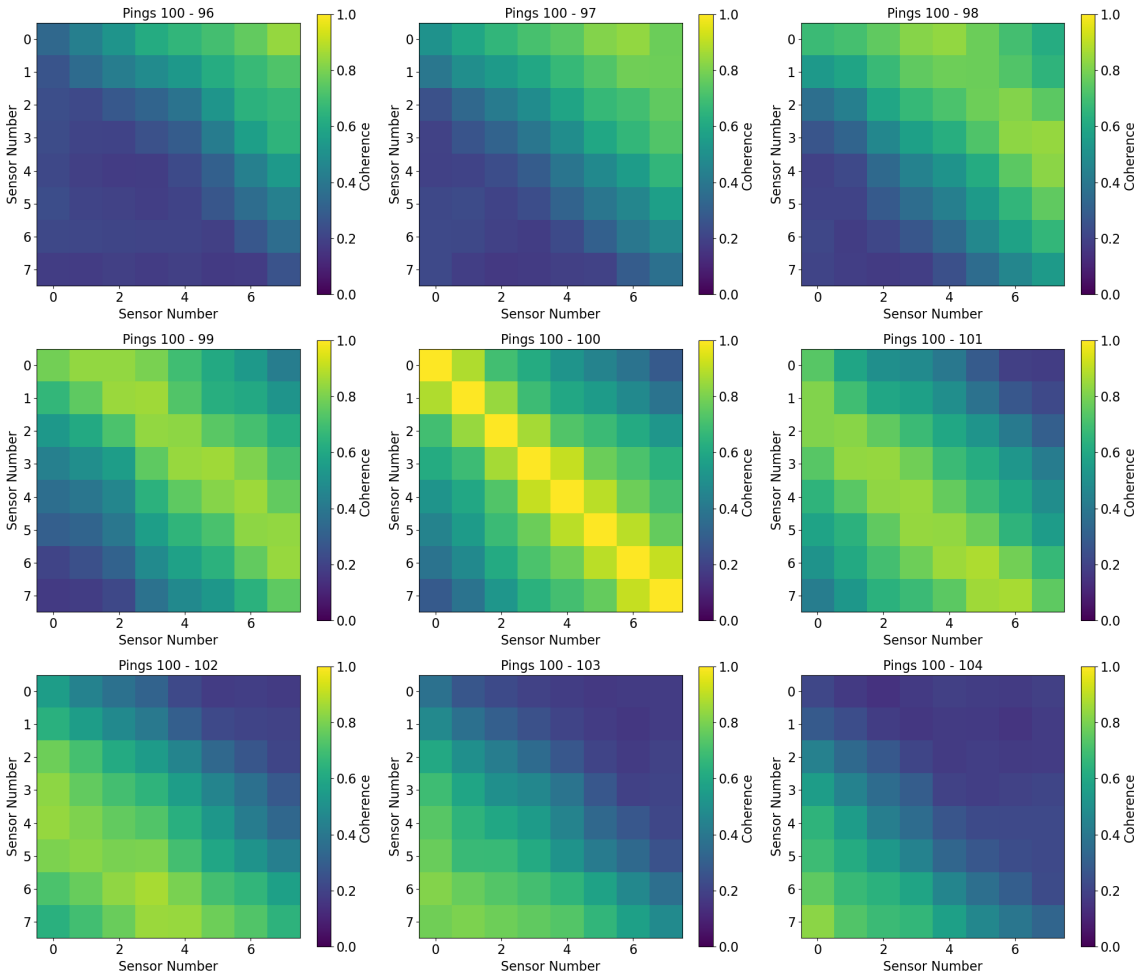

Figure 3.19: Illustration of coherence measured on sensor pairs of the horizontal antenna of HRLFSAS between successive pings

ping n°100 and all the phase centers of the ping n°101. For a given phase center, these coherence measurements are represented as a function of spatial lag (here expressed as a number of phase centres separation). The search for maximum coherence is used to estimate the displacement of the antenna between the two pings (in this case between 1 and 2 PCA separation). The array of sensors that make up the antenna can only estimate coherence discretely, and it appears here that in order to be able to accurately estimate displacement it is useful to define an interpolator. We saw in

the section 3.4, that the Van Cittert Zernike theorem predicts for HRLFSAS system a figure of coherence as a triangular shape with a length of $L_c \approx 0.5cm \approx 16 \cdot \delta$ (with δ the physical sensor lag). Such a triangle can be used as interpolator and is plotted on Figure 3.20. The top of the triangle indicates an offset of $1.77\delta_{PCA}$ i.e. a distance of $2.7cm$ which is compatible with the command applied to the carriage system on which the acquisition device is fixed .

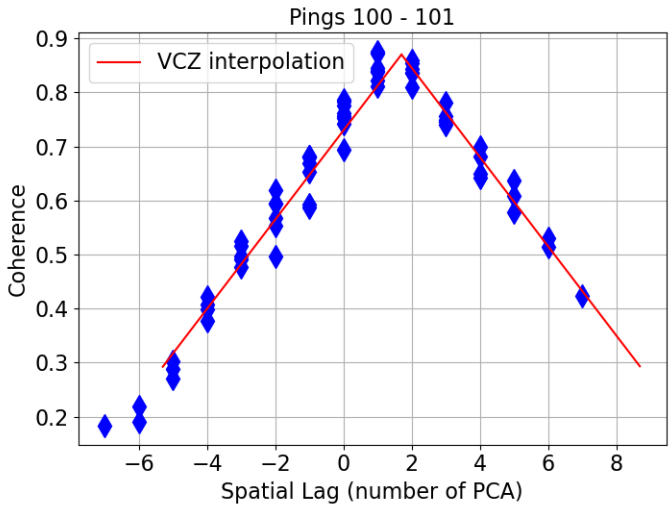

Figure 3.20: Evolution of the measured coherence between each phase centers of two successive pings as function of spatial lag. Blue dots represent the coherence estimates and the triangular red curve is the theoretical shape of the coherence as predicted by the Van Cittert Zernike theorem.

Various types of interpolator such as smoothing interpolation Kernels have been studied with the aim of improving the estimation accuracy of ping-to-ping platform displacement [Brown et al., 2020] [Thomas and Hunter, 2022]. Recently, the possibility of estimating the motion of the SAS platform using spatiotemporal coherence through a machine learning approach has been introduced [Xenaki et al., 2022].

3.6 Chapter summary

In this chapter we introduced the notion of coherence of a wavefield, and in particular its spatial coherence. Spatial coherence has been defined as the degree similarity of a signal with a version of itself in another point of the space but without temporal lag

between them. Spatial coherence can therefore be quantified through the autocorrelation along the spatial dimension. Under the ergodicity assumption, spatial coherence is estimated in practice by averaging over a time interval, and averaging over pairs of sensors with a given spatial lag.

Fundamental result of spatial coherence, the Van Cittert Zernike theorem has been presented. Originally defined in the field of statistical optics, this theorem states that in the far field of an incoherent surface, spatial coherence is proportional to the 2D Fourier transform of the intensity distribution of the surface. This formulation of the VCZ theorem, referred to as the 'Optical formulation' in this document, tells us that a broad intensity distribution will produce a wavefield with narrow spatial coherence, and conversely, a narrow intensity distribution will produce a wavefield with broad spatial coherence. However, despite of the clear interest of the VCZ in its 'optic formulation', its application to the sonar domain is not straight forward given that acoustic sources produce coherent acoustic field. However, under some assumptions, it is applicable to an acoustic field scattered by an incoherent medium. That leads to another formulation of the VCZ theorem, referred to as the 'acoustic formulation' in this document, that states that in the far field of an incoherent scattering medium insonified by an acoustic source, spatial coherence is proportional to the autocorrelation of the source aperture. Established under strong assumptions, these two forms of the theorem VCZ provide an intuitive view of spatial coherence. However, they need to be extended to suit for active sonar and to take into account physical processes (absorption, seafloor scattering capacity), hardware and computational parameters (sonar aperture, transmit signal and temporal windowing). this extension is the purpose of the following chapter.

Chapter 4

Analytical Modeling of spatial coherence

As expressed previously, VCZ theorem provides an intuitive view of the evolution of spatial coherence. However, different physical, environmental and sonar parameters have a significant influence on spatial coherence. The aim of this chapter is to define a formalism that allows the following phenomena to be taken into account when modelling coherence :

- seafloor scattering capacity;
- transmission losses;
- transmitted pulse;
- time interval over which coherence is estimated;
- sonar apertures.

The formalism proposed in this chapter enables coherence to be modelled in down-looking geometry (see section 4.2) and in side-looking geometry (see section 4.3).

4.1 Geometry and convention

Let's consider two phase centers at positions Q_1 and Q_2. The space is provided with an orthonormal reference frame illustrated on figure 4.1 and such that:

- The origin is the centre between the two phase centers;

- axis x: horizontal towards the direction of insonification (across track);
- axis y: horizontal to the direction of sonar advance (along track);
- axis z: vertical, pointing downwards.

Let's consider a scattering element $\bar{X}$ laying on the seafloor at depth d and position (x, y). The position of $\bar{X}$ can be expressed in both cartesian or spherical coordinates as follow:

$$\bar{X} = \begin{pmatrix} x \\ y \\ d \end{pmatrix} = r \begin{pmatrix} \cos(\phi)\cos(\theta) \\ \sin(\phi)\cos(\theta) \\ -\sin(\theta) \end{pmatrix} = r\vec{n} \tag{4.1}$$

where :

- ϕ is the azimuth angle positive from $\vec{x}$ to $\vec{y}$;
- θ is the grazing angle positive from $\vec{n}$ to the horizontal plane;
- $r = \sqrt{x^2 + y^2 + d^2}$ is the range;
- $\vec{n} = \begin{pmatrix} \cos(\phi)\cos(\theta) \\ \sin(\phi)\cos(\theta) \\ -\sin(\theta) \end{pmatrix}$ is the pointing vector.

Conventions and notations are illustrated in Figure 4.1

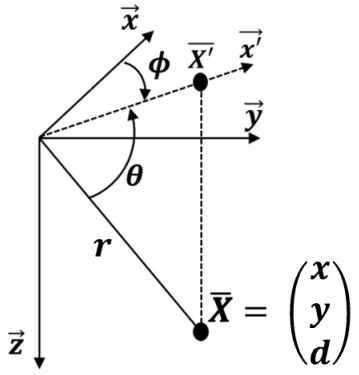

Figure 4.1: 3D representation of axis and angle conventions.

A few remarks can be made about the range of angles ϕ and θ. In a first approach, the azimuth angle ϕ is considered as a free parameter. In practice, the excursion of this angle is limited by the longitudinal aperture of the sensor. It should also be noted that in the case of side-looking sonar, an excursion greater than $[\frac{-\pi}{2}, \frac{\pi}{2}]$ makes little sense. Unlike ϕ, which is a free parameter, under flat bottom assumption, the grazing angle θ is fixed by the depth d and the slant distance r by the following pair of relationships:

$$\begin{cases} \sin(\theta) & = \frac{-d}{r} \\ \cos(\theta) & = \frac{1}{r}\sqrt{r^2 - d^2} \end{cases} \tag{4.2}$$

According to these conventions let's consider two points Q_1 and Q_2 at coordinates:

$$Q_1 = \begin{pmatrix} -x_0/2 \\ -y_0/2 \\ -z_0/2 \end{pmatrix} \qquad Q_2 = \begin{pmatrix} x_0/2 \\ y_0/2 \\ z_0/2 \end{pmatrix} \tag{4.3}$$

Notations and geometry are summarized in figure 4.2.

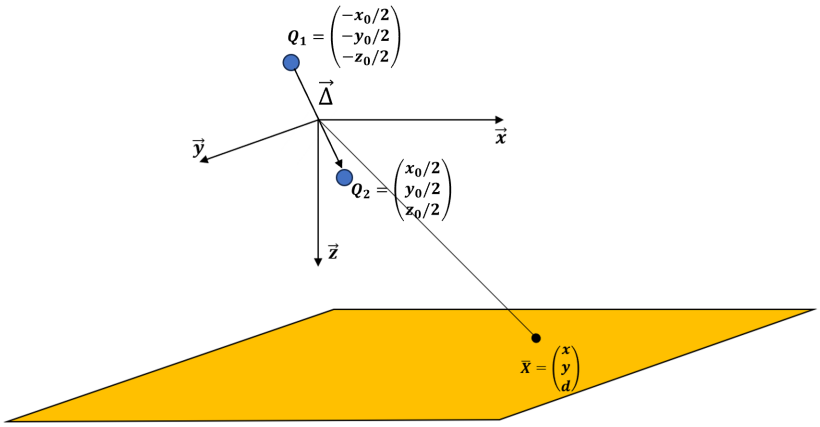

Figure 4.2: Diagram of acquisition geometry.

In the following of this section, we set out to explain an analytical formula for expressing spatial coherence as a function of the distance between points Q_1 and Q_2, i.e., according to $\vec{\Delta} = (x_0, y_0, z_0)$

4.1.1 Received signal modelling

Let's consider a phase center at position Q_i. The contribution of a scatterer $\bar{X}$ at position (x, y, d) can be expressed by:

$$s_i\left(\bar{X}, t\right) = \zeta(\bar{X})\chi(\bar{X})\sigma(\bar{X})s_0\left(t - \frac{2r_i(\bar{X})}{c}\right) \tag{4.4}$$

Where:

- c is sound speed
- $r_i(\bar{X})$ is the one way distance between points Q_i and $\bar{X}$;
- $\zeta(\bar{X})$ represents propagation losses. It is a function of distance $R(\bar{X})$ and absorption coefficient α;
- $\chi(\bar{X})$ is the combined transmit/receive directivity pattern. It is a function of frequency and aperture of the Tx/Rx element;
- $\sigma(\bar{X})$ is the seafloor reflectivity function. It is a function of bottom type;
- s_0 is the transmitted signal.

The signal sensed at position Q_i is obtained summing over all scattering elements on the insonified surface of the bottom:

$$\begin{aligned} s_i(t) &= \int_{\bar{X}} s_i\left(\bar{X}, t\right) d\bar{X} \\ &= \int_{\bar{X}} \zeta(\bar{X})\chi(\bar{X})\sigma(\bar{X})s_0\left(t - \frac{2r_i(\bar{X})}{c}\right) d\bar{X} \end{aligned} \tag{4.5}$$

4.1.2 Time difference formulation

To establish the analytical model of coherence, a formulation of time lag between signals emitted and received at positions Q_1 and Q_2 is needed. The development of this expression is presented in this section. Writing t_1 the round-trip propagation time between Q_1 and $\bar{X}$, and similarly t_2 the the round-trip propagation time between

Q_2 and $\bar{X}$, $\vec{n}$ the pointing vector and $r_0 = sqrt(x_0^2 + y_0^2 + z_0^2)$ the norm of vector $\vec{\Delta}$:

$$\begin{aligned} t_1 &= \frac{2}{c}\sqrt{\left(x + \frac{x_0}{2}\right)^2 + \left(y + \frac{y_0}{2}\right)^2 + \left(d + \frac{z_0}{2}\right)^2} \\ &= \frac{2}{c}\sqrt{x^2 + y^2 + d^2 + \frac{1}{4}\left(x_0^2 + y_0^2 + z_0^2\right) + xx_0 + yy_0 + dz_0} \\ &= \frac{2}{c}\sqrt{r^2 + \frac{1}{4}r_0^2 + r\vec{n}\cdot\vec{\Delta}} \\ &= \frac{2r}{c}\sqrt{1 + \frac{r_0^2}{4r^2} + \frac{\vec{n}\cdot\vec{\Delta}}{r}} \end{aligned} \tag{4.6}$$

and similarly,

$$\begin{aligned} t_2 &= \frac{2}{c}\sqrt{\left(x - \frac{x_0}{2}\right)^2 + \left(y - \frac{y_0}{2}\right)^2 + \left(d - \frac{z_0}{2}\right)^2} \\ &= \frac{2r}{c}\sqrt{1 + \frac{r_0^2}{4r^2} - \frac{\vec{n}\cdot\vec{\Delta}}{r}} \end{aligned} \tag{4.7}$$

Assuming that the distance to the seafloor is large compared to sensor separation:

$$x^2 + y^2 + d^2 >> x_0^2 + y_0^2 + z_0^2 \tag{4.8}$$

The following Taylor expansion can be used:

$$\sqrt{1 + x^2} = 1 + \frac{1}{2}x - \frac{1}{8}x^2 + \underset{x\to 0}{o}(x^3) \tag{4.9}$$

and equation (4.6) becomes:

$$\begin{aligned} \sqrt{1 + \frac{r_0^2}{4r^2} + \frac{\vec{n}\cdot\vec{\Delta}}{r}} &\approx 1 + \frac{1}{2}\left(\frac{r_0^2}{4r^2} + \frac{\vec{n}\cdot\vec{\Delta}}{r}\right) + \frac{1}{8}\left(\frac{r_0^2}{4r^2} - \frac{\vec{n}\cdot\vec{\Delta}}{r}\right)^2 + \underset{1/r\to 0}{o}(1/r^4) \\ &\approx \frac{\vec{n}\cdot\vec{\Delta}}{2r} + \frac{1}{8r^2}\left(r_0^2 + \frac{(\vec{n}\cdot\vec{\Delta})^2}{r^2}\right) + \underset{1/r\to 0}{o}(1/r^3) \end{aligned} \tag{4.10}$$

similarly equation (4.7) becomes:

$$\sqrt{1 + \frac{r_0^2}{4r^2} - \frac{\vec{n}\cdot\vec{\Delta}}{r}} \approx -\frac{\vec{n}\cdot\vec{\Delta}}{2r} + \frac{1}{8r^2}\left(r_0^2 + \frac{(\vec{n}\cdot\vec{\Delta})^2}{r^2}\right)2 + \underset{1/r\to 0}{o}(1/r^3) \tag{4.11}$$

Finally, time lag between signals emitted and received at positions X_1 and X_2 can be expressed by:

$$t_2 - t_1 \approx -\frac{2}{c}\vec{n} \cdot \vec{x_0} \tag{4.12}$$

Developing the spherical coordinate vector $\vec{n}$ and $\vec{x_0}$:

$$(t_2 - t_1)(r, \phi) \approx \frac{-2}{c}\left[(x_0 \cos(\phi) + y_0 \sin(\phi))\cos(\theta) - z_0 \sin(\theta)\right] \tag{4.13}$$

Or in cartesian coordinates:

$$\begin{aligned}(t_2 - t_1)(x, y) &= \frac{-2}{c \cdot r}(x \cdot x_0 + y \cdot y_0 + d \cdot z_0) \\ &\approx \frac{-2}{c \cdot d}(x \cdot x_0 + y \cdot y_0 + d \cdot z_0)\end{aligned} \tag{4.14}$$

4.1.3 Computation of spatial coherence

By definition, the coherence for a spatial lag $\vec{\Delta}$ as introduced in paragraph 4.1 is expressed by:

$$\hat{\rho}(\vec{\Delta}, t) = \langle s_1(t) \cdot s_2^*(t) \rangle \tag{4.15}$$

where

- $\langle \cdot \rangle$ represents an ensemble over seafloor realisations;
- s_1 and s_2 are two signals sensed at points of space Q_1 and Q_2 as introduced in paragraph 4.1 and such as $\overrightarrow{Q_1 Q_2} = \vec{\Delta}$

According to equation (4.5) $s_1(t)$ and $s_2(t)$ can be written:

$$s_1(t) = \int_\Sigma \zeta_1(\bar{X_1})\chi_1(\bar{X_1})\sigma(\bar{X_1})s_0\left(t - \frac{2r_1(\bar{X_1})}{c}\right)d\bar{X_1} \tag{4.16}$$

$$s_2(t) = \int_\Sigma \zeta_2(\bar{X_2})\chi_2(\bar{X_2})\sigma(\bar{X_2})s_0\left(t - \frac{2r_2(\bar{X_2})}{c}\right)d\bar{X_2} \tag{4.17}$$

Inserting equations (4.16) and (4.17) in (4.15),

$$\begin{aligned}\hat{\rho}(\vec{\Delta},t) &= \langle s_1(t)\cdot s_2^*(t)\rangle \\ &= \left\langle \int_\Sigma\int_\Sigma \zeta(\bar{X_1})\zeta(\bar{X_2})\chi_1(\bar{X_1})\chi_2(\bar{X_2})\sigma(\bar{X_1})\sigma^*(\bar{X_2}) \right. \\ &\qquad \left. s_0\left(t-\frac{2r_1(\bar{X_1})}{c}\right)s_0^*\left(t-\frac{2r_2(\bar{X_2})}{c}\right)d\bar{X_1}d\bar{X_2}\right\rangle \\ &= \int_\Sigma\int_\Sigma \zeta_1(\bar{X_1})\zeta_2(\bar{X_2})\chi_1(\bar{X_1})\chi_2(\bar{X_2})\left\langle\sigma(\bar{X_1})\sigma^*(\bar{X_2})\right\rangle \\ &\qquad s_0\left(t-\frac{2r_1(\bar{X_1})}{c}\right)s_0^*\left(t-\frac{2r_2(\bar{X_2})}{c}\right)d\bar{X_1}d\bar{X_2}\end{aligned} \tag{4.18}$$

Assuming an incoherent seafloor with constant index,

$$\left\langle\sigma(\bar{X_1})\sigma^*(\bar{X_2})\right\rangle = \sigma^2(\bar{X})\delta\left(\bar{X_2}-\bar{X_1}\right) \tag{4.19}$$

assuming similar propagation losses,

$$\zeta_1(\bar{X_1}) \approx \zeta_2(\bar{X_1}) \approx \zeta(\bar{X}) \tag{4.20}$$

and writing:

$$t_1(\bar{X}) = \frac{2r_1(\bar{X})}{c} \qquad \text{and} \qquad t_2 = \frac{2r_2(\bar{X})}{c} \tag{4.21}$$

equation (4.18) becomes:

$$\hat{\rho}(\vec{\Delta},t) = \int_\Sigma \zeta^2(\bar{X})\chi_1(\bar{X})\chi_2(\bar{X})\sigma^2(\bar{X})s_0\left(t-t1(\bar{X})\right)s_0^*\left(t-t_2(\bar{X})\right)d\bar{X} \tag{4.22}$$

As stated in part 3.3 it is often convenient to estimate coherence over a time interval $[t_i, t_f]$ and:

$$\begin{aligned}\hat{\rho}(\vec{\Delta},[t_i,t_f]) &= \int_{t_i}^{t_f}\hat{\rho}(\vec{\Delta},t)dt \\ &= \int_\Sigma \zeta^2(\bar{X})\chi_1(\bar{X})\chi_2(\bar{X})\sigma^2(\bar{X})\int_{t_i}^{t_f} s_0\left(t-t_1(\bar{X})\right)s_0^*\left(t-t_2(\bar{X})\right)dtd\bar{X}\end{aligned} \tag{4.23}$$

we then perform the following change of variable:

$$\left\{u = t - t_1(\bar{X}) \right. \tag{4.24}$$

and equation (4.23) becomes:

$$\begin{aligned}\hat{\rho}(\vec{\Delta},[t_i,t_f]) &= \int_\Sigma \zeta^2(\bar{X})\chi_1(\bar{X})\chi_2(\bar{X})\sigma^2(\bar{X}) \int_{t_i-t_1(\bar{X})}^{t_f-t_1(\bar{X})} s_0\left(u\right) s_0^*\left(u+(t_1-t_2)\left(\bar{X}\right)\right) du d\bar{X} \\ &= \int_\Sigma \zeta^2(\bar{X})\chi_1(\bar{X})\chi_2(\bar{X})\sigma^2(\bar{X})\Gamma_{\left[t_i,t_f\right]}\left((t_1-t_2)\left(\bar{X}\right)\right) d\bar{X}\end{aligned} \tag{4.25}$$

with

$$\Gamma_{\left[t_i,t_f\right]}\left((t_1-t_2)\left(\bar{X}\right)\right) = \int_{t_i-t_1(\bar{X})}^{t_f-t_1(\bar{X})} s_0\left(u\right) s_0^*\left(u+(t_1-t_2)\left(\bar{X}\right)\right) du \tag{4.26}$$

Writing s_0 as a CW signal:

$$s_0(t) = A\Pi_T(t)e^{j2\pi f_0 t} \tag{4.27}$$

where A is an amplitude factor, f_0 is the central frequency and $\Pi_T(t)$ is a rectangular function such as:

$$\Pi_T(t) = \begin{cases} 1 & \text{if} \quad |t| < \frac{T}{2} \\ 0 & \text{else} \end{cases} \tag{4.28}$$

equation (4.26) becomes

$$\begin{aligned}\Gamma_{\left[t_i,t_f\right]}\left((t_1-t_2)\left(\bar{X}\right)\right) &= \int_{t_i-t_1(\bar{X})}^{t_f-t_1(\bar{X})} s_0\left(u\right) s_0^*\left(u+(t_1-t_2)\left(\bar{X}\right)\right) du \\ &= A^2 \int_{t_i-t_1(\bar{X})}^{t_f-t_1(\bar{X})} \Pi_T(u)\Pi_T(u+(t_1-t_2)(\bar{X}))e^{j2\pi f_0(t_1-t_2)(\bar{X})} du \\ &= A^2 e^{j2\pi f_0(t_1-t_2)(\bar{X})} \int_{t_i-t_1(\bar{X})}^{t_f-t_1(\bar{X})} \Pi_T(u)\Pi_T(u+(t_1-t_2)(\bar{X}))du \\ &= A^2 e^{j2\pi f_0(t_1-t_2)(\bar{X})} \Lambda\left(\vec{\Delta},T,[t_i,t_f]\right)\left(\bar{X}\right)\end{aligned} \tag{4.29}$$

where

$$\Lambda\left(\vec{\Delta},T,[t_i,t_f]\right)\left(\bar{X}\right) = \int_{t_i-t_1(\bar{X})}^{t_f-t_1(\bar{X})} \Pi_T(u)\Pi_T(u+(t_1-t_2)(\bar{X}))du \tag{4.30}$$

Λ is a temporal function corresponding to the intersection of the pulse length T with the seafloor over the temporal interval $\left[t_i - t_1(\bar{X}), t_f - t_1(\bar{X})\right]$. It can be seen as a contribution coefficient of a point of the seafloor to the coherence. It is similar to the masking function in [Brown, 2017] or the isochronous volume in [Fink and Cardoso, 1984]. It corresponds to the portion of the seafloor that has contributed to coherence over the time interval over which it is estimated.

Inserting equation (4.29) and (4.26) in (4.25), the expression of coherence becomes:

$$\hat{\rho}(\vec{\Delta},[t_i,t_f]) = A^2 \int_{\bar{X}} \zeta^2(\bar{X})\chi_1(\bar{X})\chi_2(\bar{X})\sigma^2(\bar{X})\Lambda\left(\vec{\Delta},T,[t_i,t_f]\right) e^{j2\pi f_0(t_1-t_2)(\bar{X})} d\bar{X} \tag{4.31}$$

To probe further, we will distinguish two acquisition geometries: vertical geometry (down-looking geometry) and slant geometry (side-looking geometry). This distinction should enable us to explain the form of the masking function.

4.2 Down looking geometry

Coherence modelling of this geometry, has been studied in [Brown, 2017]. The main steps of the modelling are presented here. To do so, scattering element positions are defined in Cartesian coordinates.

$$\begin{aligned}\hat{\rho}(\vec{\Delta},[t_i,t_f]) &= A^2 \int_{\Sigma} \zeta^2(\bar{X})\chi_1(\bar{X})\chi_2(\bar{X})\sigma^2(\bar{X})\Lambda\left(\vec{\Delta},T,[t_i,t_f]\right) e^{j2\pi f_0(t_1-t_2)(\bar{X})} d\bar{X} \\ &= A^2 \iint_{x,y} \zeta^2(x,y)\chi_1(x,y)\chi_2(x,y)\sigma^2(x,y) \\ &\qquad \Lambda\left(\vec{\Delta},T,[t_i,t_f]\right) e^{j2\pi f_0(t_1-t_2)(x,y)} dxdy\end{aligned} \tag{4.32}$$

replacing $(t_1 - t_2)(x, y)$ by equation (4.14), equation (4.32) becomes

$$\begin{aligned}\hat{\rho}(\vec{\Delta},[t_i,t_f]) = A^2 \iint_{x,y} &\zeta^2(x,y)\chi_1(x,y)\chi_2(x,y)\sigma(x,y) \\ &\Lambda\left(\vec{\Delta},T,[t_i,t_f]\right) e^{j\frac{2\pi}{d\lambda_0}(x\cdot x_0+y\cdot y_0+d\cdot z_0)} dxdy\end{aligned} \tag{4.33}$$

4.2.1 Masking function

This section aims to explain the form of the masking function $\Lambda\left(\vec{x_0},T,[t_i,t_f]\right)$. Remember that

$$\begin{aligned}\Lambda\left(\vec{\Delta},T,[t_i,t_f]\right)\left(\bar{X}\right) &= \int_{t_i}^{t_f} \Pi_T(t-t_1(\bar{X}))\Pi_T(t-t_2(\bar{X}))dt \\ &= \int_{t_i-t_1(\bar{X})}^{t_f-t_1(\bar{X})} \Pi_T(u)\Pi_T(u+(t_1-t_2)(\bar{X}))du\end{aligned} \tag{4.34}$$

Assuming that the distance between points of view is small with respect to depth,

$$t_1(\bar{X}) \approx t_2(\bar{X}) \approx \bar{t}(\bar{X}) \tag{4.35}$$

where $\bar{t}(\bar{X}) = \frac{t_1(\bar{X})+t_2(\bar{X})}{2}$. Equation (4.34) becomes

$$\Lambda\left(\vec{\Delta}, T, [t_i, t_f]\right)\left(\bar{X}\right) = \int_{t_i-\bar{t}(\bar{X})}^{t_f-\bar{t}(\bar{X})} \Pi_T(u)^2 du \tag{4.36}$$

The function $\Lambda\left(\vec{\Delta}, T, [t_i, t_f]\right)$ can be interpreted as the sum over the time interval $[t_i, t_f]$ of the intersection of a rectangular pulse of length T with the seafloor. Let's first have a look on this intersection pattern. In Figure 4.3, the intersection of a rectangular pulse of length T with seafloor is illustrated for different times and different pulse lengths. This intersection pattern evolves over time, changing from a disc to a ring as the pulse propagates ($\bar{t}$ increasing). The maximum size of the disc and the thickness of the ring are a function of the pulse length T.

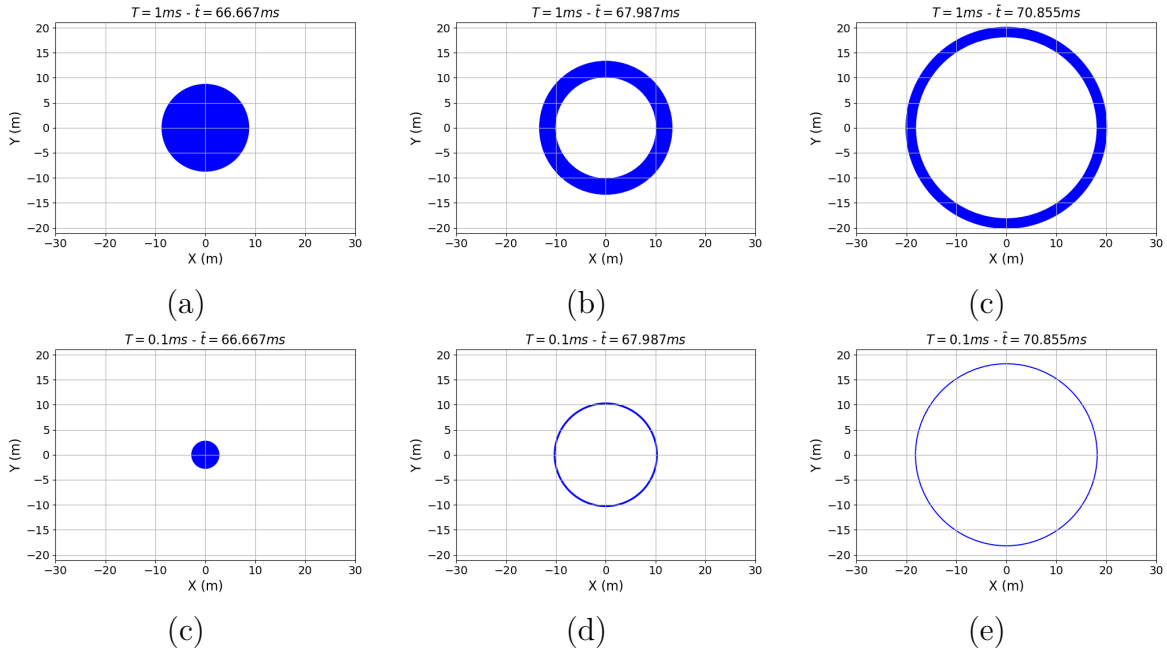

Figure 4.3: Intersection of a rectangular pulse of length T with seafloor for different times $\bar{t}$ - (a)$T = 1ms$ and $\bar{t} = 66.667ms$ - (b)$T = 1ms$ and $\bar{t} = 67.987ms$ - (c)$T = 1ms$ and $\bar{t} = 70.855ms$ - (d)$T = 0.1ms$ and $\bar{t} = 66.667ms$ - (e)$T = 0.1ms$ and $\bar{t} = 67.987ms$ - (f)$T = 0.1ms$ and $\bar{t} = 70.855ms$

As mentioned above, the function Λ represents the sum over time of the intersection of the rectangular pulse with the seafloor. This function can therefore be defined over three conditions on $\bar{X}$

- if $\bar{t}(\bar{X}) < t_i - \frac{T}{2}$ or $\bar{t}(\bar{X}) > t_f + \frac{T}{2}$, thus $\bar{X}$ is not insonified during the time interval $[t_i, t_f]$ and the masking function is null
- if $\bar{t}(\bar{X}) > t_i + \frac{T}{2}$ or $\bar{t}(\bar{X}) < t_f - \frac{T}{2}$, thus $\bar{X}$ is fully covered by the pulse and the masking function is equal to T
- if $t_i - \frac{T}{2} < \bar{t}(\bar{X}) < t_i + \frac{T}{2}$ or $t_f - \frac{T}{2} < \bar{t}(\bar{X}) < t_f + \frac{T}{2}$, thus $\bar{X}$ is covered only by a part of the pulse and the masking function evolves in proportion to the fraction of the pulse that has covered the point $\bar{X}$

This allows the form of $\Lambda\left(\vec{\Delta}, T, [t_i, t_f]\right)$ to be explained as follows

$$\Lambda\left(\vec{\Delta}, T, [t_i, t_f]\right) = \begin{cases} 0 & \text{if} \quad \bar{t}(\bar{X}) < t_i - \frac{T}{2} \\ \frac{T}{2} + \left(\bar{t} - t_i\right) & \text{if} \quad t_i - \frac{T}{2} < \bar{t}(\bar{X}) < t_i + \frac{T}{2} \\ T & \text{if} \quad t_i + \frac{T}{2} < \bar{t}(\bar{X}) < t_f - \frac{T}{2} \\ \frac{T}{2} - \left(\bar{t} - t_f\right) & \text{if} \quad t_f - \frac{T}{2} < \bar{t}(\bar{X}) < t_f + \frac{T}{2} \\ 0 & \text{if} \quad \bar{t}(\bar{X}) > t_f + \frac{T}{2} \end{cases} \tag{4.37}$$

The masking function $\Lambda\left(\vec{x_0}, T, [t_i, t_f]\right)$ is schematically represented in Figure 4.4 for two different pulse length T. White parts correspond to area of the space that are not covered by the pulse during $[t_i, t_f]$ and where the masking function is null. Blue parts correspond to area of the space that are fully covered by the pulse during $[t_i, t_f]$ and the masking function is equal to T. Transitions parts are shown in red in figures.

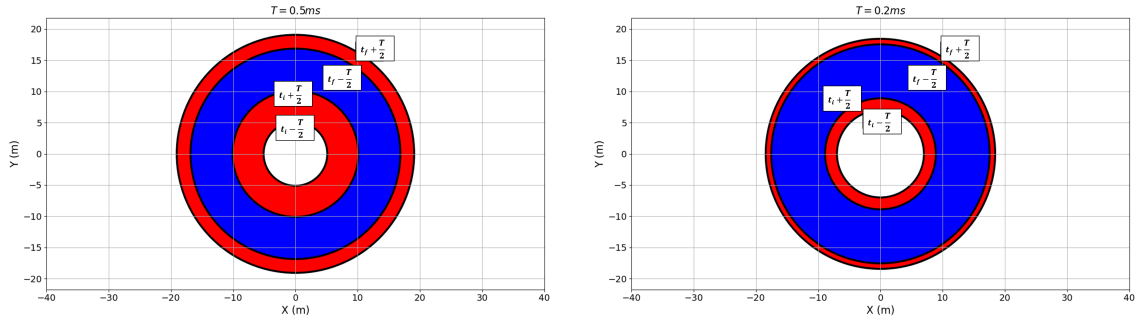

(a) (b)

Figure 4.4: Schematic view of the evolution of $\Lambda\left(\vec{\Delta}, T, [t_i, t_f]\right)$ for two different pulses length T. (a) $T = 0.5m$ - (b) $T = 0.2ms$

It can be noticed that the width of transition zones is proportional to pulse length T. Thus if the pulse is short enough, transition zones can be neglected and the masking function reduces to:

$$\Lambda\left(\vec{\Delta},[t_i,t_f]\right)=\begin{cases}0 & \text{if} \quad \bar{t}(\bar{X})<t_i\\ T & \text{if} \quad t_i<\bar{t}(\bar{X})<t_f\\ 0 & \text{if} \quad \bar{t}(\bar{X})>t_f\end{cases} \tag{4.38}$$

Moreover, if in addition of a short pulse length, the date t_i is chosen so that $t_1<\frac{2d}{c}$, thus, $\Lambda\left(\vec{\Delta},T,[t_i,t_f]\right)$ is no longer a ring but a disk whose diameter a_f is a function of time t_f:

$$a_f=\sqrt{\left(\frac{t_f\cdot c}{2}\right)^2-d^2} \tag{4.39}$$

and

$$\Lambda\left(\vec{\Delta},T,[t_i,t_f]\right)=circ_{a_f}(x,y)=\begin{cases}1 & \text{if} \quad \sqrt{x^2+y^2}<a_f\\ 0 & \text{else}\end{cases} \tag{4.40}$$

The relatively simple form of this masking function is of interest for the analytical study of coherence presented in the following paragraph.

4.2.2 Spatial Coherence

Now that we have explained the form of the masking function, we can deduce the analytical expression of coherence in simple cases.

First case

Let's consider the following assumptions:

- Omnidirectional sensors

$$\forall(x,y)\in\mathbb{R}^2 \quad \chi_1(x,y)=\chi_2(x,y)=1$$

- Homogenous flat bottom with constant index

$$\forall(x,y)\in\mathbb{R}^2 \quad \sigma(x,y)=\sigma$$

- Constant propagation losses throughout the integration domain

$$\forall(x,y)\in\mathbb{R}^2 \quad \zeta(x,y)=\zeta(0,0)=\zeta$$

under these assumptions equation (4.33) reduces to:

$$\hat{\rho}(\vec{\Delta},[t_i,t_f]) = A^2\zeta^2\sigma^2 \iint_{x,y} \Lambda\left(\vec{\Delta},T,[t_i,t_f]\right) e^{-j\frac{2\pi}{d\lambda_0}(x\cdot x_0+y\cdot y_0+d\cdot z_0)}dxdy \tag{4.41}$$

As we saw in the previous section, the masking function Λ represents the portion of the seafloor contributing to the signal during the temporal interval $[t_i,t_f]$. As a result, the equation (4.41) is similar to the Van Cittert Zernike theorem in its 'optic' formulation as it relates the spatial coherence to the 2D Fourier transform of the distribution of intensity across an incoherent source. In this case, the source is the part of seafloor temporally bounded by the masking function, and without modulation of intensity because scattering, propagation losses and directivity are considered constant.

Let's consider that $t_i < \frac{2d}{c}$ and that the pulse length T is short. In such a case, and from what we have seen about the masking function, $\Lambda\left(\vec{\Delta},T,[t_i,t_f]\right)$ reduces to disk as described by equation (4.40).

Finally, inserting equation (4.40) in (4.41) leads to

$$\begin{aligned}\hat{\rho}(\vec{\Delta},[t_i,t_f]) &= A^2\zeta^2\sigma^2 \iint_{x,y} circ_{a_f}(x,y)e^{-j\frac{2\pi}{d\lambda_0}(x\cdot x_0+y\cdot y_0+d\cdot z_0)}dxdy \\ &= A^2\zeta^2\sigma^2 e^{-j\frac{2\pi z_0}{\lambda_0}}\mathcal{F}_{2D}\left\{circ_{a_f}(x,y)\right\}\left(\frac{x_0}{d\lambda_0},\frac{y_0}{d\lambda_0}\right)\end{aligned} \tag{4.42}$$

From [Gradshteyn and Ryzhik, 2007], the 2D Fourier transform of a disk of radius a is given by:

$$\mathcal{F}_{2D}\left\{circ_a(x,y)\right\}(\kappa_x,\kappa_y) = 2\pi a^2\frac{J_1(2\pi a\sqrt{\kappa_x^2+\kappa_y^2})}{2\pi a\sqrt{\kappa_x^2+\kappa_y^2}} \tag{4.43}$$

where J_1 is the Bessel function of order 1 and a the radius of the disk. Inserting equation (4.43) evaluated at $\kappa_x = \frac{x_0}{d\lambda_0}$ and $\kappa_x = \frac{y_0}{d\lambda_0}$ into equation (4.42), spatial coherence can be written:

$$\hat{\rho}(\vec{\Delta},[t_i,t_f]) = 2A^2\zeta^2\sigma^2\pi a_f^2\frac{J_1(2\pi\frac{a_f}{\lambda_0 d}\sqrt{x_0^2+y_0^2})}{2\pi\frac{a_f}{\lambda_0 d}\sqrt{x_0^2+y_0^2}} \tag{4.44}$$

To facilitate interpretation, it is convenient to normalise the equation (4.44) and the

degree of coherence can be written

$$\begin{aligned}\hat{\mu}(\vec{x_0},[t_i,t_f]) &= \frac{\hat{\rho}(\vec{x_0},[t_i,t_f])}{\sqrt{\hat{\rho}(\vec{x_0}=(0,0,0),[t_i,t_f])^2}} \\ &= 2\frac{J_1(2\pi\frac{a}{\lambda_0 d}\sqrt{x_0^2+y_0^2})}{2\pi\frac{a}{\lambda_0 d}\sqrt{x_0^2+y_0^2}}\end{aligned} \tag{4.45}$$

For illustration purposes, figure 4.5(d) shows the degree of coherence for three different values of t_f represented in Figures 4.5(a), 4.5(b) and 4.5(c). Spatial coherence as a function of x_0 is represented in Figure 4.5(d). One can see that, increasing the value of t_f (and so increasing the diameter of the masking function), leads to a decrease of the coherence length. Obviously this illustration is very theoretical because, as mentioned above, it does not take into account energy variations within the masking function (propagation losses, bottom scattering, directivity, etc.). Nevertheless, this illustration highlights the fact that if the energy variations within the masking function remain moderate, then the size of the masking function plays a dominant role, decreasing or increasing the spatial coherence in the form of a cardinal Bessel function.

Second case

Let's consider the following assumptions:

- Homogenous flat bottom with constant index

$$\forall(x,y)\in\mathbb{R}^2 \quad \sigma(x,y)=\sigma$$

- Constant propagation losses throughout the integration domain

$$\forall(x,y)\in\mathbb{R}^2 \quad \zeta(x,y)=\zeta$$

- Time interval $[t_i,t_f]$ defined such as $t_i < \frac{2d}{c}$ and t_f large enough so that the contributing portion of the seafloor is limited by the directivity and not by the masking function. Under these assumptions:

$$\forall(x,y)\in\mathbb{R}^2 \quad \Lambda\left(\vec{\Delta},T,[t_i,t_f]\right)(x,y)=1$$

- Finite length sensors. Writing $\delta_L(X,Y)$ the aperture of sensor where L represents the characteristic aperture length of the sensors. It should be noted

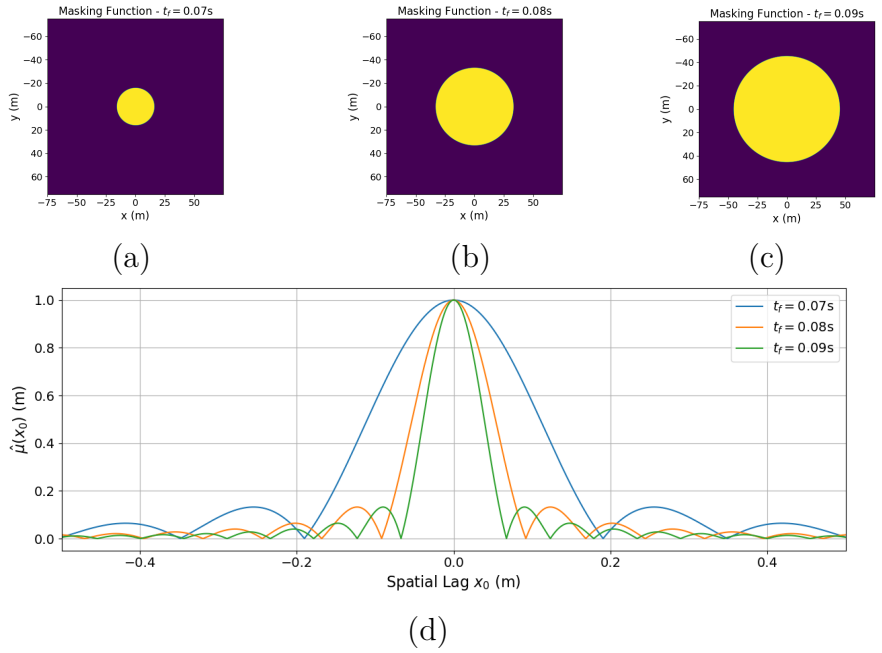

Figure 4.5: Masking function $\Lambda\left(\vec{x_0}, \left[t_i < \frac{2d}{c}, t_f\right]\right)$ for (a) $t_f = 0.07s$ - (b) $t_f = 0.08s$ -(c) $t_f = 0.09s$ - (d) Degree of coherence as function of spatial lag x_0 for the different values of t_f.

that, for the moment, no assumption has been made about the shape. The calculations that follow are valid whatever the shape of the sensor aperture (linear, rectangular, circular, etc.). In such a case

$$\forall (x,y) \in \mathbb{R}^2 \quad \chi_1(x,y) = \chi_2(x,y) = \mathcal{F}_{2D}\left\{\delta_L(X,Y)\right\}(x,y)$$

under these assumptions equation (4.33) reduces to:

$$\begin{aligned}\hat{\rho}(\vec{\Delta}, [t_i, t_f]) &= A^2\zeta^2\sigma^2 \iint_{x,y} \chi_1(x,y)\chi_2(x,y) e^{-j\frac{2\pi}{d\lambda_0}(x\cdot x_0 + y\cdot y_0 + d\cdot z_0)} dxdy \\ &= A^2\zeta^2\sigma^2 e^{-j\frac{2\pi z_0}{\lambda_0}} \iint_{x,y} \mathcal{F}_{2D}\left\{\delta_L(X,Y)\right\}^2(x,y) e^{-j\frac{2\pi}{d\lambda_0}(x\cdot x_0 + y\cdot y_0)} dxdy\end{aligned} \tag{4.46}$$

noting that,

$$\iint_{x,y} \mathcal{F}_{2D}\left\{\delta_L(X,Y)\right\}^2(x,y) e^{-j\frac{2\pi}{d\lambda_0}(x\cdot x_0 + y\cdot y_0)} dxdy = \mathcal{F}_{2D}^{-1}\left\{\mathcal{F}_{2D}\left\{\delta_L(X,Y)\right\}^2\right\} \tag{4.47}$$

where $\mathcal{F}_{2D}^{-1}\left\{\mathcal{F}_{2D}\left\{\delta_L(X,Y)\right\}^2\right\}$ is the autocorrelation of $\delta_L(X,Y)$. The equation (4.46) is similar to the Van Cittert Zernike theorem in its 'acoustic' formulation as it relates spatial coherence and the autocorrelation of the transmit aperture. Indeed, in the present case, the transmit aperture is $\delta_L(X,Y)$ and the receiver is supposed omnidirectional such as the transmit/receive aperture is only $\delta_L(X,Y)$.

Let's now consider the case of a rectangular aperture sensor with lengths L_x and L_y. In such case:

$$\delta_{L_x,L_y}(X,Y) = \begin{cases} 1 & \text{if} \quad |X| < \frac{L_x}{2} \quad \text{and} \quad |Y| < \frac{L_y}{2} \\ 0 & \text{else} \end{cases} \tag{4.48}$$

and $\forall (x,y) \in \mathbb{R}^2$

$$\begin{aligned} \chi_1(x,y) = \chi_2(x,y) &= L_x L_y \operatorname{sinc}\left(kL_x \sin(\theta_x)\right) \operatorname{sinc}\left(kL_y \sin(\theta_y)\right) \\ &= L_x L_y \operatorname{sinc}\left(\frac{kL_x}{r}x\right) \operatorname{sinc}\left(\frac{kL_y}{r}y\right) \end{aligned} \tag{4.49}$$

with $\sin(\theta_x) = \frac{x}{r}$ and $\sin(\theta_y) = \frac{y}{r}$

Inserting equation (4.49) in equation (4.46) gives:

$$\begin{aligned} \hat{\rho}(\vec{\Delta}, [t_i, t_f]) &= A^2\zeta^2\sigma^2 L_x^2 L_y^2 e^{-j\frac{2\pi z_0}{\lambda_0}} \iint_{x,y} \operatorname{sinc}^2\left(\frac{kL_x}{r}x\right) \operatorname{sinc}^2\left(\frac{kL_y}{r}y\right) e^{-j\frac{2\pi}{d\lambda_0}(x\cdot x_0 + y\cdot y_0)} dxdy \\ &= A^2\zeta^2\sigma^2 L_x^2 L_y^2 e^{-j\frac{2\pi z_0}{\lambda_0}} \int_x \operatorname{sinc}^2\left(\frac{kL_x}{r}x\right) e^{-j\frac{2\pi\cdot x\cdot x_0}{d\lambda_0}} dx \int_y \operatorname{sinc}^2\left(\frac{kL_y}{r}y\right) e^{-j\frac{2\pi\cdot y\cdot y_o}{d\lambda_0}} dy \end{aligned} \tag{4.50}$$

Assuming that the angles θ_x and θ_y remain small (narrow beam sensors), $\sin(\theta_x) = \frac{x}{r} \approx \frac{x}{d}$ and $\sin(\theta_y) = \frac{y}{r} \approx \frac{y}{d}$. Then performing the following change of variables,

$$\begin{cases} x' = \frac{x}{\lambda_0 \cdot d} \\ y' = \frac{y}{\lambda_0 \cdot d} \end{cases} \tag{4.51}$$

equation (4.50) becomes:

$$\begin{aligned} \hat{\rho}(\vec{\Delta}, [t_i, t_f]) = A^2\zeta^2\sigma^2 L_x^2 L_y^2 \left(\lambda_0 \cdot d\right)^2 e^{-j\frac{2\pi z_0}{\lambda_0}} \\ \int_{x'} \operatorname{sinc}^2\left(2\pi L_x x'\right) e^{-j2\pi\cdot x_0\cdot x'} dx' \int_{y'} \operatorname{sinc}^2\left(2\pi L_y y'\right) e^{-j2\pi\cdot y_0\cdot y'} dy' \end{aligned} \tag{4.52}$$

Noting that

$$\int_{-\infty}^{+\infty} \left(\frac{\sin(\pi L x)}{\pi L x} \right)^2 e^{-j2\pi \cdot \nu \cdot x} dx = tri_L(\nu) \tag{4.53}$$

where tri_L is the triangular function of size L defined by:

$$tri_L(x) = tri\left(\frac{x}{L}\right) = \begin{cases} 1 - \left|\frac{x}{L}\right| & \text{if} \quad \left|\frac{x}{L}\right| < 1 \\ 0 & \text{otherwise} \end{cases} \tag{4.54}$$

And finally

$$\hat{\rho}(\vec{\Delta}, [t_i, t_f]) = A^2 \zeta^2 \sigma^2 L_x^2 L_y^2 \left(\lambda_0 \cdot d\right)^2 e^{-j\frac{2\pi z_0}{\lambda_0}} tri_{2L_x}(x_0) tri_{2L_y}(y_0) \tag{4.55}$$

Assuming that points Q_1 and Q_2 laid on the same plane parallel to the seafloor $z_0 = 0$ and after normalisation:

$$\hat{\mu}(\vec{\Delta}) = tri_{2L_x}(x_0) tri_{2L_y}(y_0) \tag{4.56}$$

That corresponds to a pyramid whose base has a rectangular shape of length $4 \cdot L_x$ on $4 \cdot L_y$. However, the Van Cittert Zernike in its 'optic formulation' states that spatial coherence is proportional to the autocorrelation of the source aperture, i.e. of lengths $2 \cdot L_x$ on $2 \cdot L_y$. The difference of a factor of 2 is due to the equivalent phase centre formulation used in this document. With such a formulation, a spatial lag x_0 of two phase centers corresponds to a physical distance between sensors of $2x_0$ that is in accordance with VCZ theorem formulation. To illustrate, three different rectangular apertures illustrated in Figures 4.6(a), 4.6(b) and 4.6(c). These apertures produced a beam with a directivity (see equation (4.49)) whose projection on seafloor is represented in Figures 4.6(d), 4.6(e) and 4.6(f). These directivities take the form of a product of cardinal sines whose size is given by the frequency f_0 and the antenna aperture L_x and L_y. For this study, the frequency is fixed at $f_0 = 15kHz$.

Analytical modelling of the degree of coherence given by equation (4.56) is illustrated in Figure 4.7. Figures 4.7(a), 4.7(b) and 4.7(c) represents 2D spatial coherence corresponding to the aperture showed in Figure 4.6. For reasons of interpretation, it is often easier to analyse cross-sections of these coherences, i.e. hus along track coherence (i.e. with $x_0 = 0$) and across track coherence (i.e. with $y_0 = 0$) which are represented in Figure 4.7(d) and 4.7(e). We recognize the triangular form predicted by the VCZ theorem. We can see that a large aperture produces large coherence and vice versa. This qualitative result can be linked to case 1 discussed

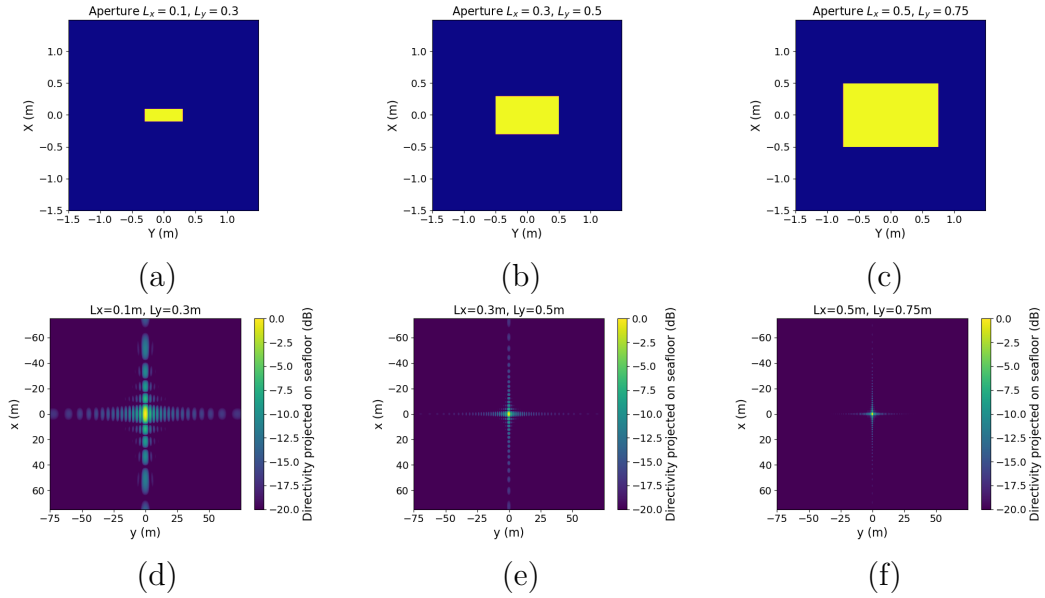

Figure 4.6: Schematic representations of the studied rectangular apertures and the respective projected directivities on the seafloor in three cases (a) (d) $Lx = 0.1$ and $Ly = 0.3$ - (b)(e) $Lx = 0.3$ and $Ly = 0.5$ - (c)(f) $Lx = 0.5$ and $Ly = 0.75$.

earlier. In fact, we saw in case 1 that if the seafloor radiation is only bounded by the masking function, then the smaller the area bounded by this function, the larger the coherence. In the present case, the seafloor radiation is no longer limited by the masking function (assumed to be very large) but by the directivity produced by an emitter with a given aperture. So the larger the aperture of the emitter, the smaller the spot on the seafloor will be, which, in a similar way to the previous case will produce large coherence.

Similarly considering the case of a gaussian aperture with parameters α_x and α_y, the aperture function can be written:

$$\delta_{\alpha_x,\alpha_y}(X,Y) = \frac{e^{-\left(\frac{X^2}{\alpha_x^2}+\frac{Y^2}{\alpha_y^2}\right)}}{\pi\alpha_x\alpha_y} \tag{4.57}$$

and $\forall(x,y) \in \mathbb{R}^2$

$$\chi_1(x,y) = \chi_2(x,y) = e^{-\frac{\omega^2}{4c^2r^2}\left(x^2\alpha_x^2+y^2\alpha_y^2\right)} \tag{4.58}$$

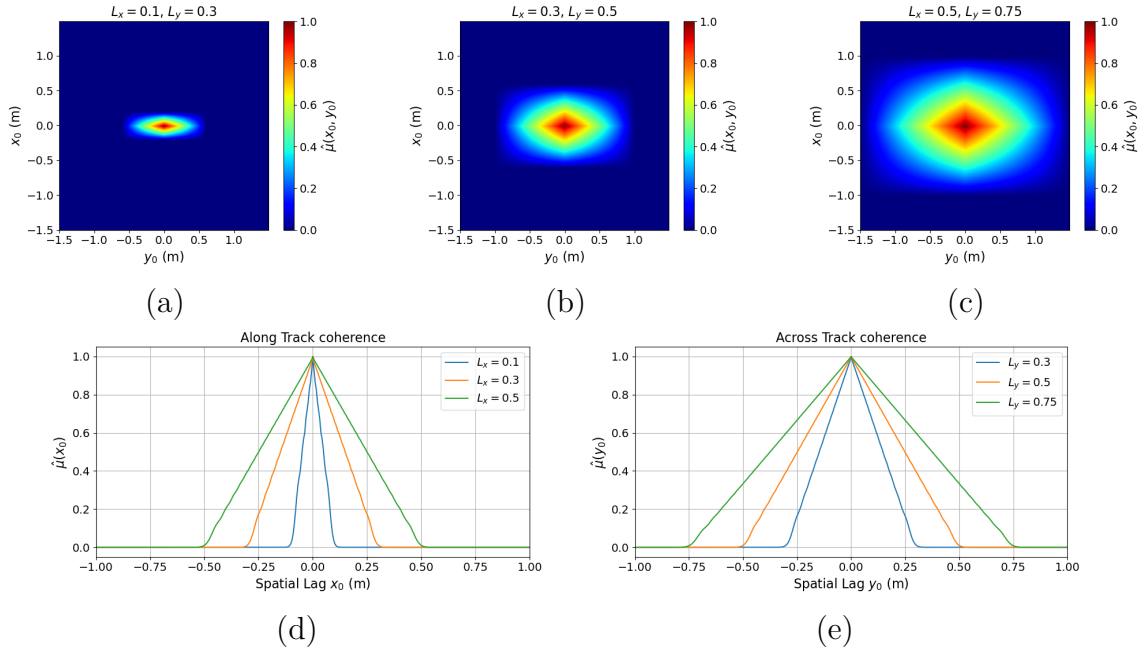

Figure 4.7: 2D degree of coherence (a) $L_x = 0.1$ and $L_y = 0.3$ - (b) $L_x = 0.3$ and $L_y = 0.5$ - (c) $L_x = 0.5$ and $L_y = 0.75$. - (d) Along track coherence - (e) Across track coherence.

In a similar way to the assumption made for the rectangular aperture, we are assuming here narrow beam sensors and so

$$\chi_1(x,y) = \chi_2(x,y) \approx e^{-\frac{\omega^2}{4c^2d^2}\left(x^2\alpha_x^2 + y^2\alpha_y^2\right)} \tag{4.59}$$

Inserting equation (4.59) in equation (4.46) gives:

$$\begin{aligned}
\hat{\rho}(\vec{\Delta}, [t_i, t_f]) &= A^2\zeta^2\sigma^2 e^{-j\frac{2\pi z_0}{\lambda_0}} \iint_{x,y} e^{-\frac{2\omega^2}{4c^2d^2}\left(x^2\alpha_x^2 + y^2\alpha_y^2\right)} e^{-j\frac{2\pi}{d\lambda_0}(x\cdot x_0 + y\cdot y_0)} dxdy \\
&= A^2\zeta^2\sigma^2 e^{-j\frac{2\pi z_0}{\lambda_0}} \int_x e^{-\frac{2\omega^2}{4c^2d^2}x^2\alpha_x^2} e^{-j\frac{2\pi}{d\lambda_0}x\cdot x_0} dx \int_y e^{-\frac{2\omega^2}{4c^2d^2}y^2\alpha_y^2} e^{-j\frac{2\pi}{d\lambda_0}y\cdot y_0} dy \\
&= A^2\zeta^2\sigma^2 e^{-j\frac{2\pi z_0}{\lambda_0}} \underbrace{\int_x e^{-\frac{2\omega^2\alpha_x^2}{4c^2d^2}x^2 - j\frac{2\pi x_0}{d\lambda_0}x} dx}_{\Phi_x} \underbrace{\int_y e^{-\frac{2\omega^2\alpha_y^2}{4c^2d^2}y^2 - j\frac{2\pi y_0}{d\lambda_0}y} dy}_{\Phi_y}
\end{aligned} \tag{4.60}$$

From [Gradshteyn and Ryzhik, 2007] equation (3.323)

$$\int_{-\infty}^{+\infty} e^{-p^2x^2 \pm qx} dx = \frac{\sqrt{\pi}}{p} e^{\frac{q^2}{4p^2}} \tag{4.61}$$

and so,

$$\Phi_x = \int_x e^{-\frac{2\omega^2\alpha_x^2}{4c^2d^2}x^2 - j\frac{2\pi x_0}{d\lambda_0}x} dx = \frac{2cd\sqrt{\pi}}{\omega\alpha_x} e^{\frac{-x_0^2}{\alpha_x^2}} \tag{4.62}$$

and similarly

$$\Phi_y = \int_y e^{-\frac{2\omega^2\alpha_y^2}{4c^2d^2}x^2 - j\frac{2\pi y_o}{d\lambda_0}y} dy = \frac{2cd\sqrt{\pi}}{\omega\alpha_y} e^{\frac{-y_0^2}{\alpha_y^2}} \tag{4.63}$$

and finally

$$\hat{\rho}(\vec{\Delta}, [t_i, t_f]) = A^2\zeta^2\sigma^2 \frac{4\pi c^2 d^2}{\omega^2\alpha_x\alpha_y} e^{-\left(\frac{x_0^2}{\alpha_x^2} + \frac{y_0^2}{\alpha_y^2}\right)} \tag{4.64}$$

$$\hat{\mu}(\vec{x_0}) = e^{-\left(\frac{-x_0^2}{\alpha_x^2} + \frac{y_0^2}{\alpha_y^2}\right)} \tag{4.65}$$

In the same way as for the rectangular aperture case, directivities and coherence are represented in Figure 4.8. Figures 4.8(a), 4.8(b), and 4.8(c) shows the three studied apertures, respectively ($\alpha_x = 0.1$, $\alpha_x = 0.04$), ($\alpha_x = 0.05$, $\alpha_x = 0.07$) and ($\alpha_x = 0.06$, $\alpha_x = 0.08$). Figures 4.8(d), 4.8(e), and 4.8(f) show directivities projected on seafloor as given by equation (4.59). Figures 4.8(g), 4.8(h), and 4.8(i) show 2D spatial coherence as predicted by the analytical modelling given by equation (4.65). Finally along track coherence (i.e. with $x_0 = 0$) and across track coherence (i.e. with $y_0 = 0$) are represented in Figures 4.8(e) and 4.8(f). We verify the Gaussian form predicted by the VCZ theorem.

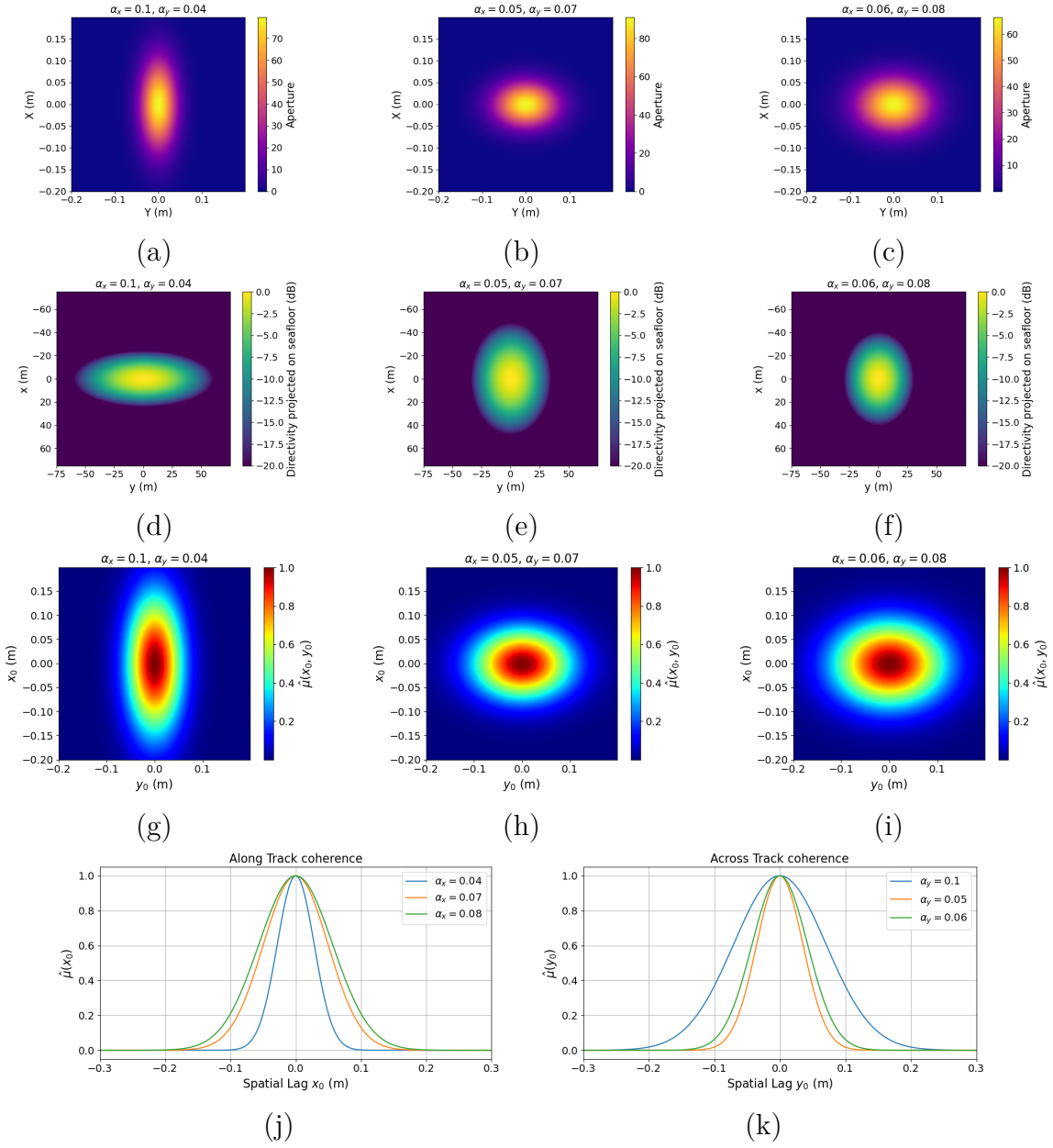

Figure 4.8: Schematic representations of the studied gaussian apertures, respective directivities projected on seafloor and respective 2D degree of coherence (a)(d)(g) $\alpha_x = 0.1$ and $\alpha_x = 0.04$ - (b)(e)(h) $\alpha_x = 0.05$ and $\alpha_x = 0.07$ - (c)(f)(i) $\alpha_x = 0.06$ and $\alpha_x = 0.08$ - (j) Along track coherence - (k) Across track coherence.

4.2.3 Summary of the analytical expression of coherence in down looking geometry

To summarise, the equation (4.33) presented in this section, models spatial coherence in the case of down-looking sonars. This expression is very similar to the VCZ in its optical formulation in that it relates the coherence factor to the 2D Fourier transform of the intensity distribution across an incoherent source, it being understood that in the present case this incoherent source is the insonified seafloor. To avoid confusion, we will refer to the portion of the seafloor contributing to coherence as the 'seafloor equivalent source' and the sonar transmit device as the 'transmit source'. Spatial coherence will therefore be a function of the extent and distribution of energy within the equivalent seafloor source. As shown by equation (4.33), this distribution of intensity of the seafloor equivalent source is determined by:

- Directivity functions χ_1 and χ_2. These functions depend on the aperture of the sensors and the frequency. The larger the aperture of the transducers, the narrower the directivity lobe. Similarly, the higher the frequency, the narrower the lobe. The directivity diagram depends on the shape of the transducers. In this way, the directivity functions limit the extent of the seafloor equivalent antenna and modulate the energy distribution within it.

- A masking function Λ that is a function of the time interval over which coherence is estimated. This masking function spatially corresponds to the part of the seabed covered by the sonar pulse during the estimated time interval. We saw in part 4.2.1 that if the pulse is sufficiently short (T small), then the masking function is constant over these non-zero values. If the pulse is long, then the masking function has transition zones at its boundaries. The masking function affects the extent of the seafloor equivalent source.

- The seafloor reflectivity function σ that is maximal at nadir and then decreases with incidence angle. This decrease depends on the type of seafloor. For very rough bottoms, this decrease will be moderate, whereas smoother seafloors will show greater decreases. Therefore, a smooth seafloor will tend to reduce the extent of the seafloor equivalent source while smoothing the energy distribution within the masking function. For frequencies between $10kHz$ and $100kHz$, it can be modelled by the Jackson model.

- The propagation loss function. It depends on the absorption coefficient and increase with range. Thus propagation loss function will limit the extent of the seafloor equivalent source.

The complexity of these different functions does not allow us to solve the model analytically in a general case. Special simplified cases have been presented in this section. This has enabled us to recover, under strong assumptions, two major results from [Fink and Cardoso, 1984]. Firstly, the degree of coherence is proportional to the autocorrelation of the transmit source aperture. To obtain this result it is necessary to assume a time interval such that the masking function is large enough not to limit the extent of the seafloor equivalent source. Similarly, propagation losses and the reflectivity function of the seafloor must be assumed to be constant so as not to influence the intensity distribution of the seafloor equivalent source. Under these assumptions, the extent and energy distribution of the seafloor equivalent source (and so the degree of coherence) is defined only by the directivity (and therefore the aperture) of the sensors. The second result we were able to observe is that coherence is independent of frequency. This result can be explained as follows. For a given transmit source aperture an increase in frequency results in a narrower directivity, which in turn results in a smaller seafloor equivalent source extent. This equivalent seafloor source therefore radiates at a higher frequency but from a smaller extent. These two effects compensate each other, resulting in a field radiated by the seafloor equivalent source with the same coherence as that which would have been produced by the same transmit source at a different frequency. However, this independence in terms of frequency needs to be discussed. Indeed, as we have just said, a change in the radiation pattern of a transmit source due to a change in frequency is 'compensated' by the change in the extent of the seafloor equivalent source. However, this reasoning does not take into account the effect of the change in frequency on other parameters such as the seafloor scattering function or propagation losses, which will also affect the extent and energy distribution of the seafloor equivalent source and so the coherence. From an operational point of view, this frequency independence can only be observed for frequency intervals that do not significantly modify the reflectivity of the seafloor and propagation losses.

In the next chapter, numerical methods will be used to discuss the influence of other parameters but first let's look at the establishment of the analytical model in the side looking geometry.

4.3 Side looking geometry

The aim of this section is to present a formalism for obtaining an analytical formulation of coherence in the case of sonar in side looking geometry.

4.3.1 Received signal modelling

We recall that the signal received at the position of a phase centre Q_i can be written according to the equation (4.5)

$$s_i(t) = \int_{\Sigma} \zeta(\bar{X})\chi(\bar{X})\sigma(\bar{X})s_0\left(t - \frac{2r_i(\bar{X})}{c}\right) d\bar{X} \tag{4.66}$$

Using the spherical coordinates shown in Figure 4.1, equation (4.5) can be written:

$$s_i(t) = \iint_{r,\phi} \zeta(r)\chi(r,\phi)\sigma(r)s_0\left(t - t_i(r,\phi)\right) r dr d\phi \tag{4.67}$$

Considering that sensors are infinitely open in the vertical direction (narrow aperture and wide beamwidth), thus χ does not depend on r:

$$\chi(r,\phi) = \chi(\phi)$$

Under this hypothesis and with this formalism, the analytical formula for coherence expressed by the equation (4.31) becomes:

$$\hat{\rho}(\vec{\Delta},[t_i,t_f]) = A^2 \iint_{r,\phi} \zeta^2(r)\chi_1(\phi)\chi_2(\phi)\sigma^2(r,\phi)\Lambda\left(\vec{\Delta},T,[t_i,t_f]\right) e^{j2\pi f_0(t_1-t_2)(r,\phi)} r dr d\phi \tag{4.68}$$

4.3.2 Masking function

In a similar way to what was discussed in part 4.2.1 for vertical geometry, the masking function Λ corresponds to the portion of the seafloor contributing during the time interval $[t_i, t_f]$ under consideration. Its analytical expression is similar to the previous case and given by:

$$\Lambda\left(\vec{x_0},T,[t_i,t_f]\right) = \begin{cases} 0 & \text{if} \quad \frac{2r}{c} < t_i - \frac{T}{2} \\ \frac{T}{2} + \left(\frac{2r}{c} - t_i\right) & \text{if} \quad t_i - \frac{T}{2} < \frac{2r}{c} < t_i + \frac{T}{2} \\ T & \text{if} \quad t_i + \frac{T}{2} < \frac{2r}{c} < t_f - \frac{T}{2} \\ \frac{T}{2} - \left(\frac{2r}{c} - t_f\right) & \text{if} \quad t_f - \frac{T}{2} < \frac{2r}{c} < t_f + \frac{T}{2} \\ 0 & \text{if} \quad \frac{2r}{c} > t_f + \frac{T}{2} \end{cases} \tag{4.69}$$

with the difference that in the side looking geometry, the excursion range of ϕ is limited to the interval $\left[\frac{-\pi}{2}, \frac{\pi}{2}\right]$. Figure 4.9 shows the footprint of the masking function on the seafloor for two different pulse length values. As stated for the down looking geometry, if the pulse length T is short enough, masking function can be assumed constant over its non zero values.

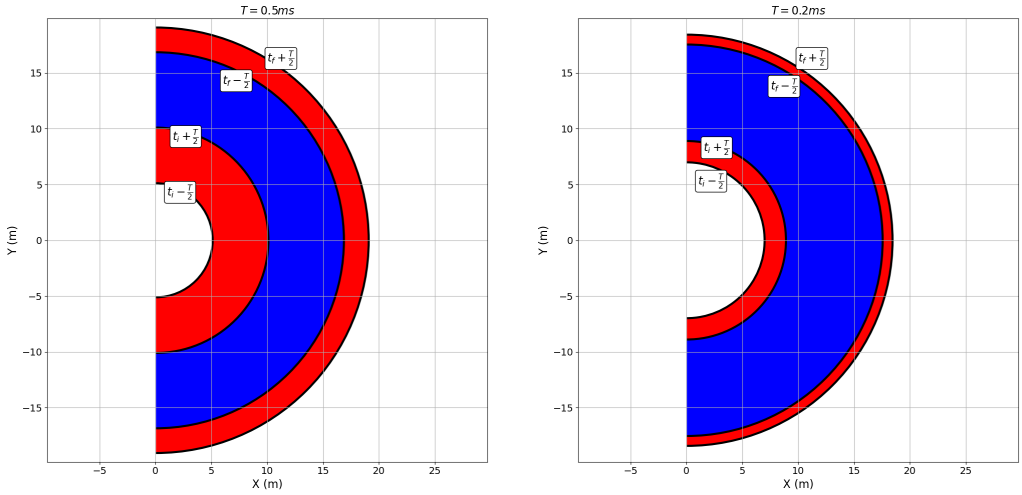

(a) (b)

Figure 4.9: Schematic view of the evolution of $\Lambda\left(\vec{x_0}, T, [t_i, t_f]\right)$ in side looking geometry for two different pulse length T. (a) $T = 0.5ms$ - (b) $T = 0.2ms$.

4.3.3 Side Looking directivity projected on seafloor

In the same way as in down looking geometry, equation (4.68) shows directivity pattern projected onto the seafloor. In side looking observation geometry, acquisition and reception devices are often tilted at a given angle from the vertical direction in order to orientate the directivity lobes. Figure 4.10(a) shows directivity projected onto the seafloor for a transmitter with a rectangular aperture tilted at 30° from the vertical. In Figure 4.10(b) along track directivities are represented for different longitudinal (L_x) apertures. We can recognize the classic form of the cardinal sine, similar to that observed in the down looking geometry, where the width of the main lobe is inversely proportional to the aperture of the transmission device. In Figure 4.10(c) across track directivities are represented for different vertical (L_x) apertures. We can see that the beam's footprint on the seafloor tends to 'spread out'. It is this tendency that allows us to make the hypothesis that for a sensor that is sufficiently vertically open, and for a given temporal interval $[t_i, t_f]$, the directivity pattern projected onto the seafloor ($\chi_1(\phi)$ and $\chi_2(\phi)$) of the equation (4.68) only depends on ϕ and no more on r.

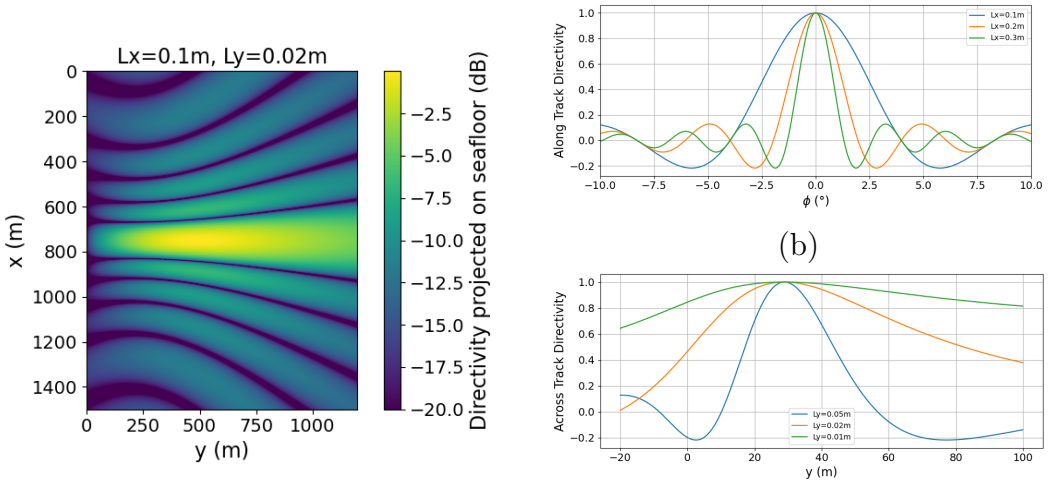

(a) (b) (c)

Figure 4.10: (a) Illustration of directivity projected onto the seafloor for a transmitter with a rectangular aperture tilted at 30° from the vertical -(b) Along track directivities for different longitudinal (L_x) apertures - (c) Across track directivities for different vertical (L_y) apertures.

4.3.4 Spatial coherence computation

Now that we have clarified the shape and expression of the masking function in part 4.3.2, we can continue to develop the expression of the spatial coherence in side looking geometry. Let's go back to the equation (4.68).

$$\hat{\rho}(\vec{\Delta},[t_i,t_f]) = A^2 \iint_{r,\phi} \zeta^2(r)\chi_1(\phi)\chi_2(\phi)\sigma^2(r)\Lambda\left(\vec{\Delta},T,[t_i,t_f]\right) e^{j2\pi f_0(t_1-t_2)(r,\phi)} r dr d\phi \tag{4.70}$$

Let us then consider that the interval $[t_i,t_f]$ is sufficiently short so that the integration factor and the propagation losses do not vary significantly $\forall r \in \left[\frac{ct_i}{2},\frac{ct_f}{2}\right]$. Writing $\bar{r} = \frac{\frac{ct_i}{2}+\frac{ct_f}{2}}{2}$ equation (4.70) becomes

$$\hat{\rho}(\vec{\Delta},[t_i,t_f]) = A^2\zeta^2(\bar{r})\bar{r}^2 \iint_{r,\phi} \chi_1(\phi)\chi_2(\phi)\sigma^2(r)\Lambda\left(\vec{\Delta},T,[t_i,t_f]\right) e^{j2\pi f_0(t_1-t_2)(r,\phi)} dr d\phi \tag{4.71}$$

Under this same assumption on the interval $[t_i,t_f]$, the scattering term does not vary significantly $\forall r \in \left[\frac{ct_i}{2},\frac{ct_f}{2}\right]$ and the time difference $(t_1-t_2)(r,\phi)$ does not depend

on r. Moreover, for a short pulse length T, we will consider a constant masking function such as:

$$\Lambda\left(\vec{\Delta}, T, [t_i, t_f]\right)(r, \phi) \approx \begin{cases} 0 & \text{if } \frac{2r}{c} < t_i \\ T & \text{if } t_i < \frac{2r}{c} < t_f \\ 0 & \text{if } \frac{2r}{c} > t_f \end{cases} \tag{4.72}$$

By restricting the integration domain over r to the interval $\left[\frac{t_i c}{2}, \frac{t_f c}{2}\right]$ for which Λ is non-zero, we obtain:

$$\begin{aligned} \hat{\rho}(\vec{\Delta}, [t_i, t_f]) &= A^2 \zeta^2(\bar{r}) \sigma^2(\bar{r}) \bar{r}^2 T \int_{\frac{t_i c}{2}}^{\frac{t_f c}{2}} \int_{\phi} \chi_1(\phi) \chi_2(\phi) e^{j 2\pi f_0 (t_1 - t_2)(\phi)} dr d\phi \\ &= A^2 \zeta^2(\bar{r}) \sigma^2(\bar{r}) \bar{r}^2 T \frac{c(t_f - t_i)}{2} \int_{\phi} \chi_1(\phi) \chi_2(\phi) e^{j 2\pi f_0 (t_1 - t_2)(\phi)} d\phi \end{aligned} \tag{4.73}$$

Recalling from equation (4.13) that time difference is expressed by:

$$(t_2 - t_1)(\phi) = \frac{-2}{c} \left[(x_0 \cos(\phi) + y_0 \sin(\phi)) \cos(\theta) - z_0 \sin(\theta) \right] \tag{4.74}$$

Assuming that ϕ is small, cosinus and sinus can be developed at the order 2 and:

$$\begin{cases} \sin(\phi) & \approx \phi \\ \cos(\phi) & \approx 1 - \frac{\phi^2}{2} \end{cases} \tag{4.75}$$

Inserting equation (4.75) in equation (4.74)

$$\begin{aligned} (t_2 - t_1)(\phi) &= \frac{-2}{c} \left[\left(x_0 \left(1 - \frac{\phi^2}{2} \right) + y_0 \phi \right) \cos(\theta) - z_0 \sin(\theta) \right] \\ &= \frac{-2}{c} \left[\frac{-x_0}{2} \cos(\theta) \phi^2 + y_0 \cos(\theta) \phi + x_0 \cos(\theta) - z_0 \sin(\theta) \right] \end{aligned} \tag{4.76}$$

and

$$\begin{aligned} 2\pi f_0 (t_1 - t_2)(\phi) &= \frac{-2\pi x_0 \cos(\theta)}{\lambda_0} \phi^2 + \frac{4\pi y_0 \cos(\theta)}{\lambda_0} \phi + \frac{4\pi}{\lambda_0} (x_0 \cos(\theta) - z_0 \sin(\theta)) \\ &= -\alpha \phi^2 + 2\beta \phi + \gamma \end{aligned} \tag{4.77}$$

with

$$\begin{aligned}\alpha &= \frac{2\pi x_0 \cos(\theta)}{\lambda_0} \\ \beta &= \frac{2\pi y_0 \cos(\theta)}{\lambda_0} \\ \gamma &= \frac{4\pi}{\lambda_0}\left(x_0 \cos(\theta) - z_0 \sin(\theta)\right)\end{aligned} \tag{4.78}$$

Inserting equation (4.77) in equation (4.73), the coherence analytical expression reduces to

$$\begin{aligned}\hat{\rho}(\vec{\Delta}, [t_i, t_f]) &= A^2 \zeta^2(\bar{r}) \sigma^2(\bar{r}) \bar{r}^2 T \frac{c(t_f - t_i)}{2} \int_\phi \chi_1(\phi)\chi_2(\phi) e^{j(-\alpha\phi^2 + 2\beta\phi + \gamma)} d\phi \\ &= A^2 \zeta^2(\bar{r}) \sigma^2(\bar{r}) \bar{r}^2 T \frac{c(t_f - t_i)}{2} e^{j\gamma} \underbrace{\int_\phi \chi_1(\phi)\chi_2(\phi) e^{j(-\alpha\phi^2 + 2\beta\phi)} d\phi}_{\Phi(\phi)}\end{aligned} \tag{4.79}$$

We can see that with these notations $\alpha \propto x_0$, $\beta \propto y_0$ and γ is the delayed arrival time projected on the antenna. Therefore equation (4.79) is similar to the equation (4.33) for the down looking geometry. In the following part, this spatial coherence theoretical formula is illustrated in some simple cases.

4.3.5 Along and across track coherence

By way of illustration, equation (4.79) is solved in certain simple cases.

Case 1: Along track spatial coherence

Let's consider the following assumptions:

- A gaussian aperture sensor. As previously stated, sensors are considered fully open in the vertical plan, and so

$$\begin{aligned}\chi_1(\phi) = \chi_2(\phi) &= e^{\frac{-\omega^2 \alpha_y^2 y^2}{4c^2 R^2}} \\ &= e^{\frac{-\omega^2 \alpha_y^2 \cos^2(\theta) \sin^2(\phi)}{4c^2}} \\ &\approx e^{\frac{-\omega^2 \alpha_y^2 \cos^2(\theta)}{4c^2}\phi^2}\end{aligned} \tag{4.80}$$

- A zero across track spatial lag: $x_0 = 0$, and so the function Φ in equation (4.79) reduces to:

$$\begin{aligned}\Phi(\phi) &= \int_{\phi} \chi_1(\phi)\chi_2(\phi)e^{j2\beta\phi}d\phi \\ &= \int_{\phi} \chi_1(\phi)\chi_2(\phi)e^{\frac{j4\pi y_0\cos(\theta)}{\lambda_0}\phi}d\phi\end{aligned} \tag{4.81}$$

One can note the close resemblance between the equation (4.81) and the integral part of equation (4.46) developed for the down looking geometry for which we would also have chosen a zero across track spatial lag: $x_0 = 0$. We will show in the remainder of this calculation that under the same assumptions as those used in the case 2 of the calculation of spatial coherence in down looking geometry, in side looking geometry, longitudinal coherence also follows the VCZ theorem in its 'acoustic' formulation Inserting equation (4.80), in equation (4.81) and using [Gradshteyn and Ryzhik, 2007] equation (3.323):

$$\begin{aligned}\Phi(\phi) &= \int_{\phi} e^{-\frac{k^2\alpha_y^2\cos^2(\theta)}{2}\phi^2+2jky_0\cos(\theta)\phi}d\phi \\ &= \frac{\sqrt{2\pi}}{k\alpha_y\cos(\theta)}e^{-\frac{(2\cdot y_0)^2}{\alpha_y^2}}\end{aligned} \tag{4.82}$$

and finally,

$$\hat{\rho}(\vec{\Delta},[t_i,t_f]) = A^2\zeta^2(\bar{r})\sigma^2(\bar{r})\bar{r}^2T\frac{\sqrt{\pi}c(t_f-t_i)}{\sqrt{2}k\alpha_y\cos(\theta)}e^{-\frac{(2\cdot y_0)^2}{\alpha_y^2}+j\cdot\gamma} \tag{4.83}$$

And after normalisation,

$$\hat{\mu}(\vec{\Delta},[t_i,t_f]) = e^{-\frac{(2\cdot y_0)^2}{\alpha_y^2}+j\cdot\gamma} \tag{4.84}$$

Except for the phase shift γ induced by the delay between the two sensors, equation (4.84) is similar to equation (4.65); It is easy to show that in a case of a linear aperture, spatial coherence would have been:

$$\hat{\mu}(\vec{\Delta},[t_i,t_f]) = tri_L(2\cdot x_0)e^{+j\cdot\gamma} \tag{4.85}$$

Case 2: across track spatial coherence

Let's now consider the case where the along track spatial lag y_0 is null and study the form of the spatial coherence function as a function of across track spatial lag x_0. In

this case, χ_1 and χ_2 remain unchanged but $\beta = 0$ and

$$\Phi(\phi) = \int_{\phi} \chi_1(\phi)\chi_2(\phi)e^{-j\alpha\phi^2}d\phi \tag{4.86}$$

We can see from the equation (4.86) that the parameter α, which is proportional to the spatial lag across track x_0, is a factor of ϕ^2 and not just ϕ. Thus coherence in the across track direction is no longer linked to a fourier transform of the intensity distribution on the bottom, as is the case under certain hypotheses in the down looking geometry or in the along track direction for a side looking geometry. If we develop the expression for Φ, we obtain

$$\begin{aligned}\Phi(\phi) &= \int_{\phi} e^{-\left(\frac{k^2\alpha_y^2\cos^2(\theta)}{2}+j\alpha\right)\phi^2}d\phi \\ &= \int_{\phi} e^{-\frac{k\cos(\theta)}{2}\left(k\cos(\theta)\alpha_y^2+2jx_0\right)\phi^2}d\phi \\ &= \frac{\sqrt{2\pi}}{\sqrt{k\cos(\theta)\left(k\cos(\theta)\alpha_y^2+2jx_0\right)}}\end{aligned} \tag{4.87}$$

We can see that unlike the previous example (along-track displacement) for which the Φ function had the same form as that predicted by the VCZ theorem (triangular in the case of linear openings, and Gaussian in the case of Gaussian openings), in the case of across-track displacement, the form of the Φ function given by the equation (4.87) is very different. Figure 4.11 represents the evolution of coherence as a function of a displacement across track x_0 for different apertures (Figure 4.11(a)) and for different central frequencies (Figure 4.11(b)). We can see that in the case of across-track displacement, coherence is all the more greatly reduced: the smaller the longitudinal aperture of the sensors α_y and the lower the central frequency f_0. This is because, in the case of across-track displacement, it is the curvature of the wavefront within the directivity of the sensors that reduces coherence. Thus small physical apertures will produce very wide directivity lobes in which the differences in curvature of the wavefronts will reduce the level of coherence. Similarly, at a fixed physical aperture, a drop in wave frequency will lead to a larger directivity lobe and therefore to a faster drop in the coherence level.

Case 3: Bi-dimensional coherence

To conclude this chapter, we can also explain the form of the 2D coherence function in the case of a linear aperture. In this case, χ_1 and χ_2 remain unchanged but $\alpha \neq 0$

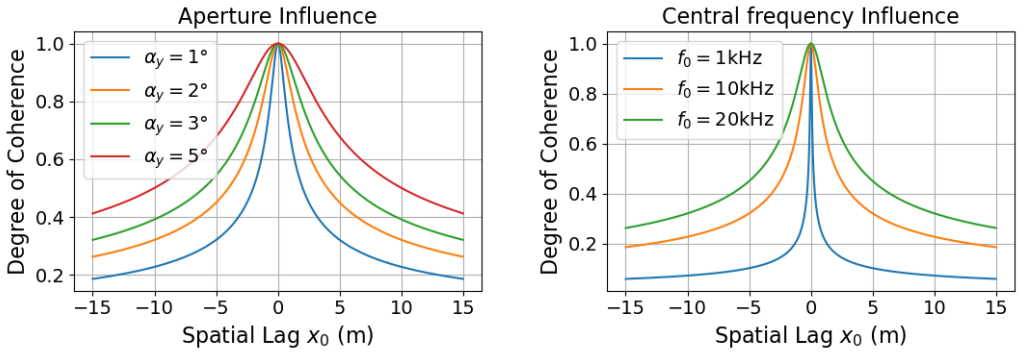

(a) (b)

Figure 4.11: Evolution of coherence as a function of a across track displacement x_0 for (a) different apertures α_y and (b) different central frequencies f_0

and $\beta \neq 0$ and $\Phi(\phi)$ becomes.

$$\begin{aligned}\Phi(\phi) &= \int_{\phi} \chi_1(\phi)\chi_2(\phi) e^{j\left(-\alpha\phi^2 + 2\beta\phi\right)} d\phi \\ &= \int_{\phi} e^{-\left(\frac{k\alpha_y^2 \cos^2(\theta)}{2} + jx_0\cos(\theta)\right)\phi^2 + j2ky_0\cos(\theta)\phi} d\phi \\ &= \frac{\sqrt{2\pi}}{\sqrt{k\cos(\theta)\left(k\cos(\theta)\alpha_y^2 + 2jx_0\right)}} e^{\frac{-2ky_0^2\cos(\theta)}{k\alpha_y^2\cos(\theta)+j2x_0}}\end{aligned} \tag{4.88}$$

Note that if $y_0 = 0$ and $x_0 \neq 0$, equation (4.88) reduces to equation (4.87) and if $y_0 \neq 0$ and $x_0 = 0$, equation (4.88) reduces to equation (4.82). Figure 4.12 represents 2D spatial coherence for different apertures α_y. We find that the coherence drop occurs very quickly in the along-track direction (of the order of the antenna aperture as predicted by the VCZ theorem) whereas in the across-track direction, the coherence length is greater. We also note that, as indicated above, the coherence length in the across-track direction still depends on the longitudinal aperture α_y and that the larger this aperture (directional beam), the greater the coherence length. However, a point which was not raised and which is well illustrated by the figure is that if x_0 increases (across-track shift), coherence decreases but tolerance to an along-track spatial lag (y_0) seems to increase.

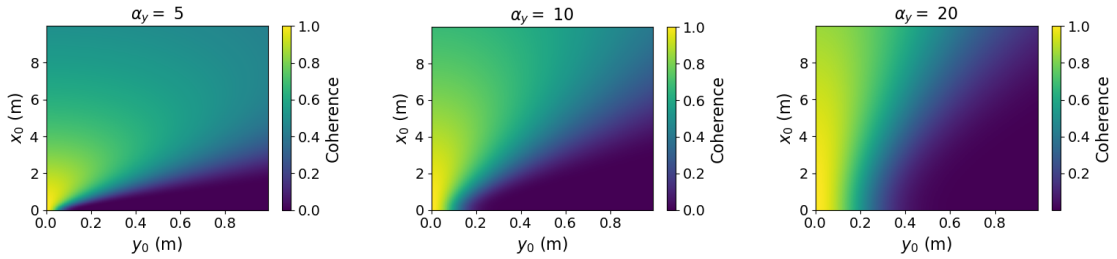

(a) (b) (c)

Figure 4.12: 2D spatial coherence for different apertures α_y (a) $\alpha_y = 5°$, (b) $\alpha_y = 10°$, and (c) $\alpha_y = 20°$

4.4 Chapter summary

In this chapter, an analytical model of spatial coherence has been detailed. For this purpose, the study has been separated into two acquisition geometries:

- **Down-looking geometry:** Receivers are assumed to laid on the same plan parallel to the seafloor. The depth is considered to be large compared to the other dimensions of the problem, in particular the size of the observation zone (i.e. the distance between the receivers) and the extent of the scattering area (i.e. high directivity beams).

- **Side-looking geometry:** In such a case, sensors are assumed to be fully opened in the vertical plane. Moreover, scattering and transmission losses terms are assumed not vary much over the portion of the seafloor sensed during the time interval $[t_i, t_f]$ defining the estimate of the spatial coherence.

The model expression obtained in the down-looking geometry is presented in part 4.2, equation (4.33). This expression is very similar to the VCZ in its optical formulation in that it relates the coherence factor to the 2D Fourier transform of the intensity distribution across an incoherent source, it being understood that in the present case this incoherent source is the insonified seafloor (called 'seafloor equivalent source' in this document). Spatial coherence is therefore a function of the extent and distribution of intensity within the equivalent seafloor source. Extent and distribution of intensity within the equivalent seafloor source is a combination of seafloor scattering, sound absorption, sonar aperture, transmit signals and temporal windowing effects. It has been shown that considering directional sensors (i.e. with a

finite aperture) and, assuming homogeneous flat bottom with constant index, constant propagation losses, temporal window $[t_i, t_f]$ such as $t_i < \frac{2d}{z}$ and t_f large enough so that the contributing portion of the seafloor is limited by the directivity and not by the masking function, coherence is proportional to the autocorrelation of the sensor aperture, as predicted by the VCZ in its 'acoustic formulation'.

The model expression obtained in the side-looking geometry is presented in part 4.3, equation (4.79). It has been shown that:

- **Along-track coherence**: assuming a null across-track spatial lag and directional sensors in the along-track direction (i.e. with a finite aperture), along-track coherence follows the VCZ theorem in its 'acoustical formulation'.
- **Across-track coherence**: assuming a null along-track spatial lag and directional sensors in the along-track direction (i.e. with a finite aperture) it has been shown that across-track coherence depends on along-track aperture: the longer the aperture the wider the coherence
- **Bi-dimensional coherence**: in the case of a Gaussian aperture, it was possible to compute the form of the 2D coherence, i.e. in the presence of an along-track and an across-track spatial lag (see equation (4.88)). The expression thus obtained is compatible with the results obtained in just one of the two dimensions (i.e. evaluating the expression at an along-track or across-track spatial lag equal to 0). However, there is one point in this model that we are unable to explain. Indeed,we noticed that in the presence of spatial lag in both dimensions, if across-track spatial lag increases, coherence decreases but tolerance to an along-track spatial lag seems to increase. This point will have to be studied in greater detail to ensure that it is not a phenomenon induced by a modelling hypothesis.

Chapter 5

Numerical study of spatial coherence

In the previous chapter, we presented an analytical expression of spatial coherence for down looking and side looking geometries. However, we were only able to solve the integral form of these expressions under very restrictive hypotheses, that is why in this chapter we propose a numerical study of the coherence. This numerical study will be based on two methods. First, a numerical integration of the equations 4.31 for the down looking geometry and 4.79 for the side looking geometry. This numerical integration should make it possible to extend the analytical study presented in the previous chapter by relaxing some assumptions. In particular those relating to the masking function Λ and those relating to the bottom reverberation σ. The numerical resolution of the analytical models is satisfactory in the down looking geometry, but in the side looking geometry, the geometric decorrelation phenomena, not taken into account in the analytical model, led us to propose a numerical modelling of the temporal signals from which the spatial coherences are estimated. This numerical modelling of the signals, which is closer to the actual acquisition geometry, is the second point in the numerical study of coherence and allows to take into account geometric decorrelation.

In the first part of this chapter we present the geometric decorrelations that mismatch footprint and stretching are. Then in part 5.2 the numerical integration of the equations 4.31 for the down looking geometry allows to study the influence of various time windows $[t_i, t_f]$ as well as the influence of sediment type through various forms of scattering function. Finally, in the part 5.3, the signals are modelled numerically using the point-based scattering model. Using the simulated signals,

coherences are estimated before and after compensation for geometric phenomena.

5.1 Geometric decorrelation

Geometric decorrelation, also called 'baseline decorrelation' is a well known phenomenon in the SAR community. It can be divided into two contributions: the mismatch footprint and the stretching. These two points are presented hereafter.

5.1.1 Mismatch footprint

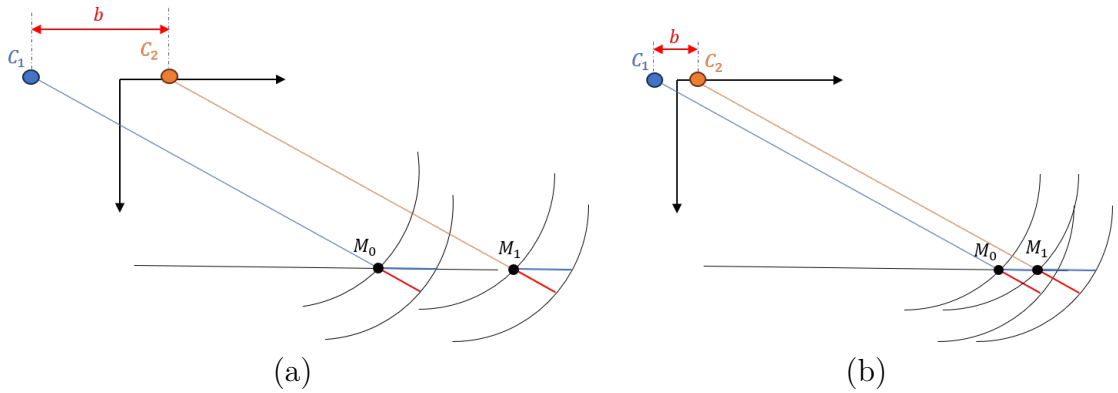

Figure 5.1: Illustration of the mismatch footprint phenomenon for two different baselines. On illustration (a) baseline is larger than on illustration (b). It can be noticed than on illustration (a) the portions of the seafloor contributing to the two sensors are completely separated, whereas in illustration (b) they partly overlap.

Let's consider t_1, the time at which, contribution of seabed point M_0 is sensed by the phase center C_1. This date is given by

$$t_1 = \frac{2 \cdot d_1(0)}{c} \tag{5.1}$$

where $d_1(0)$ is the one way distance between the phase center C_1 and the point M_0 and c is the sound speed. Similarly, let's consider t_2, the time which, contribution of seabed point M_0 is sensed by the phase center C_2.

Time difference $t_1 - t_2$ corresponds to the temporal lag between time at which the contribution of M_0 is perceived by the phase centers C_1 and C_2. It can be expressed by the well known interferometric equation:

$$t_1 - t_2 = \frac{2 \cdot (d_1(0) - d_2(0))}{c} = \frac{2b\sin(\zeta)}{c} \tag{5.2}$$

where b is the baseline and ζ is the pointing angle.

At the date t_1 the portion of the seabed that contributed to signal sensed at phase center C_1 corresponds at all the scattering elements, continuously distributed around M_0 and contained in the resolution cell projected onto the seafloor. Thus, noting x_0 the abscissa of the point M_0 and Δr the range resolution, the portion of the seafloor that contributed to the signal measured in C_1 is:

$$\mathbb{M}_1 = \left\{ M_x, x \in \left[x_0 - \frac{\Delta r}{2\sin(\zeta)}, x_0 + \frac{\Delta r}{2\sin(\zeta)} \right] \right\} \tag{5.3}$$

At the same t_1 the portion of the seabed that contributed to the signal sensed at phase center C_2 is different of whose sensed by C_1 (and defined as $\mathbb{M}_1$). Indeed, in such a case, contributing scattering elements are still contained into the resolution cell projected on seafloor but are now distributed around another point M_1. In the case of a flat seafloor and phase centers lying on the same plane of the seafloor (as illustrated in Figure 5.1), M_1 is located at abscissa $x_1 = x_0 + b$ and the ensemble $\mathbb{M}_2$ of points contributing at signal sensed at C_2 at the date t_1 is:

$$\begin{aligned} \mathbb{M}_2 &= \left\{ M_x, x \in \left[x_1 - \frac{\Delta r}{2\sin(\zeta)}, x_1 + \frac{\Delta r}{2\sin(\zeta)} \right] \right\} \\ &= \left\{ M_x, x \in \left[x_0 + b - \frac{\Delta r}{2\sin(\zeta)}, x_0 + b + \frac{\Delta r}{2\sin(\zeta)} \right] \right\} \end{aligned} \tag{5.4}$$

This shift on seafloor contributing area is called the mismatch footprint which can lead to decorrelation, if it is left uncompensated.

Note that in this case, range resolution can refer either to the resolution achieved by raw signals or after pulse compression. In the case of a match-filtered LFM signal $\Delta r = \frac{c}{2B}$ where B is the bandwidth.

The decorrelation induced by mismatch footprint is illustrated in Figure 5.1. On this figure the situation of two phase centers insonifying a part of a flat seafloor at a given instant of time is illustrated for two different baselines. The portions of

the seafloor contributing to the two sensors are completely separated in illustration (a), whereas in illustration (b) they partly overlap. At this point, the reader can begin to get an idea of how coherence evolves as a function of the baseline and the size of the resolution cell projected onto the seafloor. Indeed, for a large baseline (with respect to range resolution projected onto seafloor), portions of the seafloor contributing to signals sensed at position C_1 (ensemble $\mathbb{M}_1$) and C_2 (ensemble $\mathbb{M}_2$) are completely disjoint (see 5.1(a)) and thus, signals are expected to be uncorrelated. On the contrary, if the baseline is short with respect to range resolution projected onto seafloor, portions of the seafloor contributing to signals sensed at position C_1 (ensemble $\mathbb{M}_1$) and C_2 (ensemble $\mathbb{M}_2$) are partially joint (see 5.1(b)) and thus, signals are expected to be partially correlated.

5.1.2 Stretching

Stretching effect occurs after mismatch footprint compensation. Let's consider a perfect mismatch footprint compensation around M_0, that means that M_0 contribution occurs at the same time sample on both signals sensed at phase centers C_1 and C_2. However, this compensation is carried out only for the point M_0 and because of the difference of point of view from both phase centers, other contributions will occurs on C_2 at a shifted instant of time compared to their contribution on the signal sensed at position C_1. In other words, the scene viewed from C_2 is covered at a faster rate than the one viewed from C_1. Therefore, even if the contribution M_0 acts on the same time sample of signals sensed at C_1 and C_2, it will not be the case for the other contributing elements. As in the case of the mismatch footprint, the reader can see here the relationship between decorrelation induced by stretching phenomenon and resolution projected onto seafloor. Indeed, for a large baseline (with respect to range resolution projected onto seafloor), and with the exception of the point M_0 which is assumed to be perfectly aligned, other scatterers will contribute on both signals at different instant of time and thus induce decorrelation. This is illustrated on Figure 5.2. The seafloor section between points M_0 and M_x is insonified by the phase center C_2 at a faster rate than the same portion of the seafloor that would be insonified by the phase centre C_1.

According to notations introduced in Figure 5.2, relative time stretching β is given by

$$\beta = \frac{M_xA - M_xB}{M_xB} = \frac{\sin(\gamma + \varphi)}{\sin(\gamma)} - 1 \tag{5.5}$$

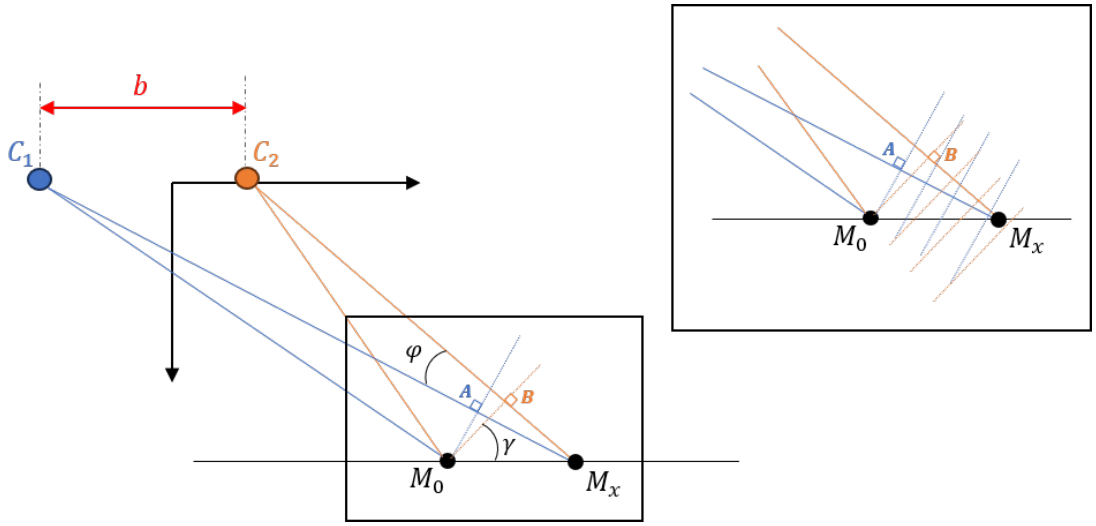

Figure 5.2: Illustration of the stretching phenomenon. The seafloor section between points M_0 and M_x is insonified by the phase center C_2 at a faster rate than the same portion of the seafloor that would be insonified by the phase centre C_1.

5.1.3 Summary on decorrelation on side looking configuration

In this section, we propose to summarise the influence of previously introduced geometric decorrelations (stretching and mismatch footprint). In the manner of [Cervenka, 2013], and with the geometry introduced on the figures 5.1 and 5.2, let's consider two phase centers separated by a baseline b. Contribution of scatterer M_0 does not occur at the same instant of time on signals s_1 and s_2. Considering t_1, the date on which a given scatterer M_0 contributes to the signal sensed at position C_1, this scatterer M_0 will contribute to the signal sensed at position C_2 at a slightly different instant of time t_2 such that $t_2 = t_1 + \delta_t$, δ_t being the footprint mismatch compensation parameter. However, as introduced previously, compensation by the parameter δ_t allows to match contribution of scatterer M_0 on both signals but not to match all the other contributions.

Compensation principle is illustrated in Figure 5.3. In Figure 5.3(a-1) and 5.3(a-2), raw signals (without any compensation) are illustrated. At this stage, contribution of M_0 occurs at at time lag δ_t on signals s_1 and s_2. Contribution of a scatterer M_x also occurs at different instant of time but with a time lag different of δ_t. In Figures 5.3(b-1) and 5.3(b-2), signals after mismatch footprint compensation are

illustrated. After mismatch footprint compensation, contribution of M_0 occurs on the same sample on signals $s_1(t)$ and $s_2(t+\delta_t)$ but it is not the case for the other scatterers. That can be seen in Figure 5.3(b-2) on which one can notice that the signals are well aligned for the first few samples (around the M_0 scattering point), then the signals shift relative to each other as the contributing elements move away from M_0. Stretching compensation deals with this point and consists of expanding signal s_2 by a stretching ratio β. This second compensation is illustrated in Figures 5.3(c-1) and figure 5.3(c-2).

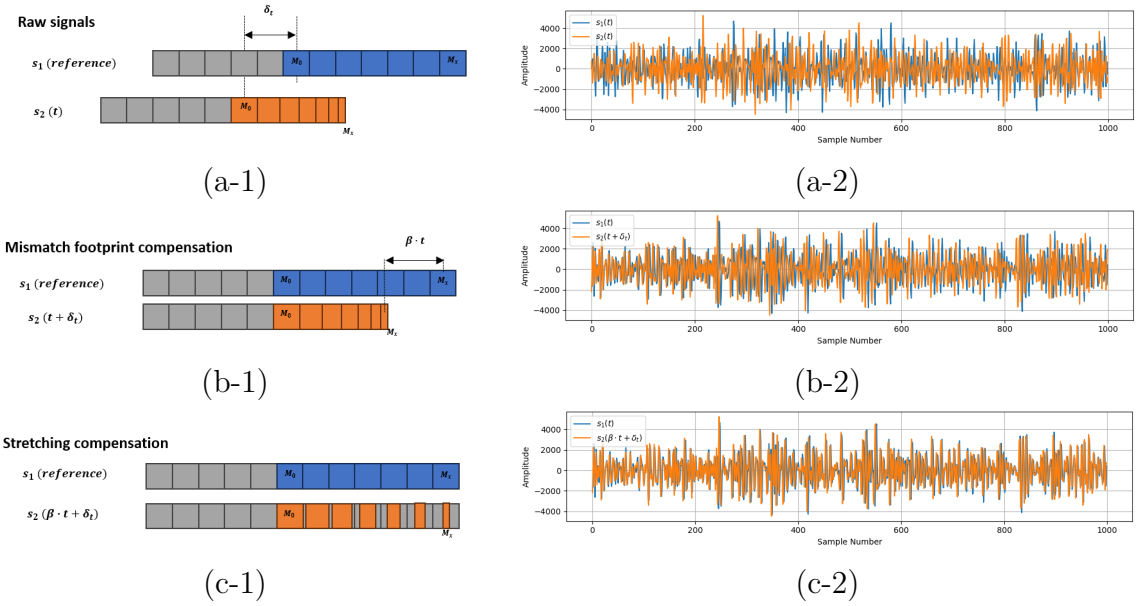

Figure 5.3: Illustration of mismatch footprint and stretching compensation. The first column represents the position of the time samples and column 2 represents the superposition of signals s_1 and s_2. (a-1) and (a-2) without any compensation - (b-1) and (b-2) after mismatch footprint compensation - (c-1) and (c-2) after mismatch footprint and stretching compensation.

5.2 Solving the analytical solution numerically

5.2.1 Principle

First of all, let's recall the two equations modelling spatial coherence as presented in the previous chapter:

- In side down geometry

$$\hat{\rho}(\vec{\Delta},[t_i,t_f]) = A^2 \iint_{x,y} \zeta^2(x,y)\chi_1(x,y)\chi_2(x,y)\sigma(x,y) \Lambda\left(\vec{\Delta},T,[t_i,t_f]\right) e^{j\frac{2\pi}{d\lambda_0}(x\cdot x_0+y\cdot y_0)}dxdy \tag{5.6}$$

- In side looking geometry

$$\hat{\rho}(\vec{\Delta},[t_i,t_f]) = A^2\zeta^2(\bar{r})\sigma^2(\bar{r})\bar{r}^2T\frac{c(t_f-t_i)}{2}\int_\phi \chi_1(\phi)\chi_2(\phi)e^{j(-\alpha\phi^2+2\beta\phi+\gamma)}d\phi \tag{5.7}$$

where:

- $\vec{\Delta}$ is the phase center separation (or baseline)
- $[t_i, t_f]$ is the temporal interval used to estimate spatial coherence
- ζ represents propagation losses
- χ_1 and χ_2 are transmit/receive directivities of the two phase centers
- Λ is the masking function.

The principle of numerical solving is based on computing the various terms of the integrand (described as 'seafloor equivalent source' previously) and computing the integral numerically. This integration is done using the python *dblquad* function from the *scipy.integrate* library in version 1.10. This process is illustrated in figure 5.4 for a gravelly seafloor and linear aperture antenna. Figures 5.4(a), 5.4(b), 5.4(c), 5.4(d) represent respectively layers of:

(a) the masking function Λ. The properties of this function are described in part 4.2.1. It is a function of the time interval $[t_i, t_f]$ over which coherence is assessed and the pulse length T. In this example, pulse length is too short for the transition zones on the masking function to be visible. Moreover, because $t_i > \frac{2d}{c}$ ($d = 50m$ is depth and $c = 1500m \cdot s^{-1}$ is sound speed), masking function corresponds geometrically to a ring and not a disk.

(b) the directivity functions χ_1 and χ_2 projected on seafloor. In this example, Combined transmit/receive directivity at the two points are considered equal and corresponds at that produced by a rectangular aperture transmit source and a ponctual receiver.

(c) the backscattering function σ. It is a function of bottom type, frequency and incident angle. The jackson model [Jackson et al., 1986], valid at frequencies between 10 and 100 kHz, is used here. The result is given here for for a gravelly seafloor.

(d) the transmission loss function ζ. It is a function of range and of an absorption coefficient. This coefficient depends on salinity, depth, frequency and temperature [Francois and Garrison, 1982a][Francois and Garrison, 1982b].

All these layers are combined to form the layer of the seafloor equivalent source represented in Figure 5.4(e). Finally the 2D integration of the seafloor equivalent source is performed and normalized to estimate spatial coherence as represented in Figure 5.4(f). Although the spatial coherence studied is 2D, in this section we have chosen to show only the longitudinal and transverse curves of the spatail 2D coherence. Thus longitudinal coherence is a function of y_0 and corresponds to $x_0 = 0$ and transverse coherence is a function of x_0 and corresponds to $y_0 = 0$. Obviously, given that the assumptions made for the analytical resolution are not verified (for example on the masking function Λ which is no longer a disk but a ring), the seafloor equivalent source is significantly modified (Figure 5.4(f)) and the observed coherences (Figure 5.4(d)) very different from those modelled in the previous chapter.

In order to validate this numerical integration process, we can compare these results with the theoretical results from the previous chapter. Lets first solve the case number 1 of the down looking geometry (see part 4.2.2). Remember that in this case, we assumed omnidirectional sensors ($\chi_1 = \chi_2 = 1$), a constant scattering function ($\sigma = 1$), neglected propagation losses ($\zeta = 1$) and a disk masking function Λ. Perfect matching between analytical modelling (equation (4.44)) and numerical solving can be observed in Figure 5.5(a). Similarly, numerical solving and analytical modelling in the case n°2 for the down looking geometry (see part 4.2.2 equation (4.56)) are compared on 5.5(a). In this illustration a rectangular aperture antenna with dimensions $L_y = 0.5m$ (longitudinal) and $L_x = 1m$ (transversal) is used. Remember that in this case we assumed sensors with similar apertures ($\chi_1 = \chi_2 = \mathcal{F}_{2D}\{\delta_L(X, Y)\}$), a constant scattering function ($\sigma = 1$), neglected propagation losses ($\zeta = 1$) and a disk masking function Λ whose extent was sufficiently large so as not to restrict the influence of

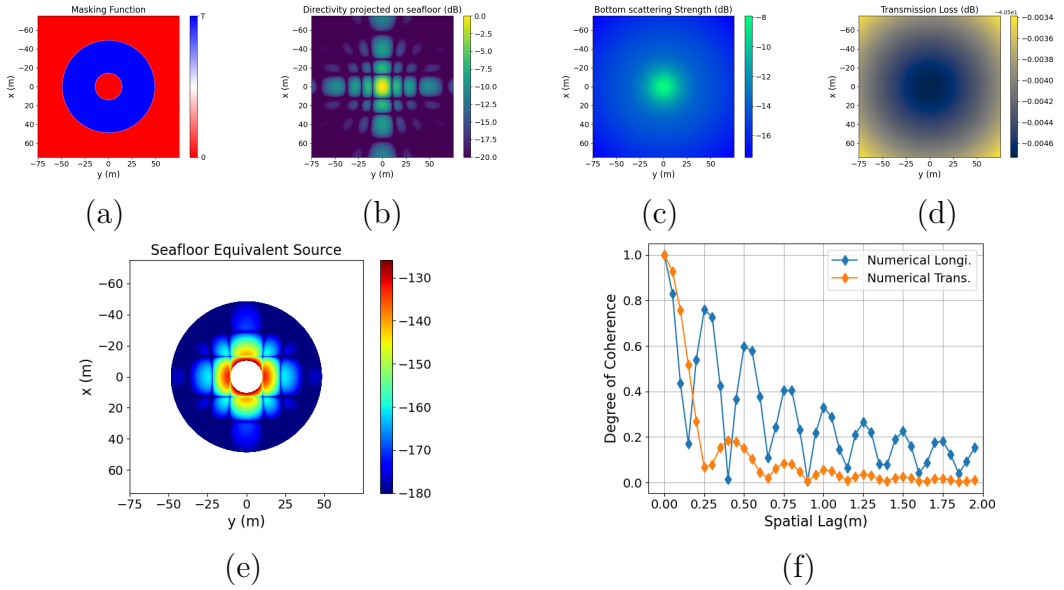

Figure 5.4: Representation of the numerical evaluation process of coherence analytical models (a) Masking function Λ with $t_i = 0.068s$, $t_f = 0.093s$ -(b) Directivity projected on seafloor for a linear aperture with $Lx = 0.4m$ and $Ly = 0.5$ - (c) Bottom scattering strength function σ for a gravelly seafloor - (d) Transmission loss function ζ for an absorption coefficient $\alpha = 0.01db/km$ - (e) Seafloor equivalent source.

the directivity term. As predicted by the analytical model, coherence functions with triangular shapes and sizes proportional to aperture are obtained.

As mentioned above, such a numerical resolution must allow the coherence to be evaluated numerically by varying certain parameters whose complexity of terms does not allow analytical resolution. The influence of the scattering term σ and the time window Γ are presented in the following sections.

5.2.2 Study of the influence of the scattering term σ

Let's studying the influence of the backscattering function σ. It is a function of bottom type and incident angle. Depending on frequency and applications, several description of this term can be found [Lamarche et al., 2011] [Jackson et al., 1986]. The Jackson model, valid at frequencies between 10 and 100 kHz is used here. In Figure 5.6, backscattering function projected onto seafloor are represented for: (a) a muddy sediment, (b) a sandy sediment and (c) a gravelly sediment. Computational

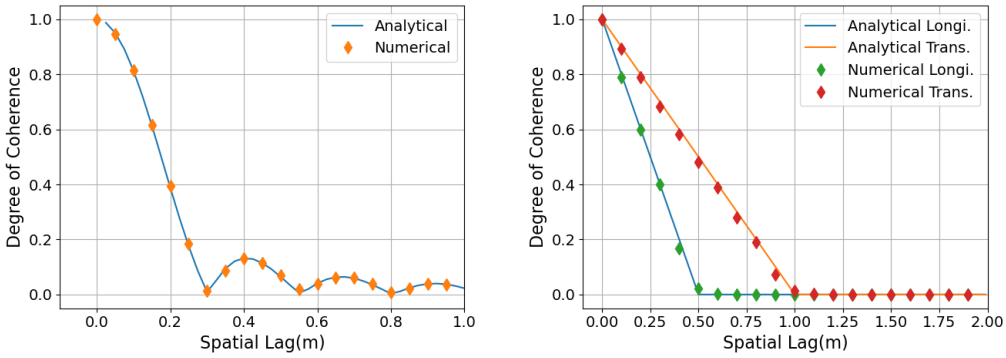

(a) (b)

Figure 5.5: (a) Comparison between analytical modelling solved in case 1 (equation (4.44)) and numerical solving with $t_f = 0.06734ms$ - (b) Comparison between analytical modelling solved in case 2 (equation (4.56)) and numerical solving for rectangular apertures with $L_y = 0.5m$ and $L_x = 1m$.

parameters of the Jackson model for these sediments are given in the legend of the figure.

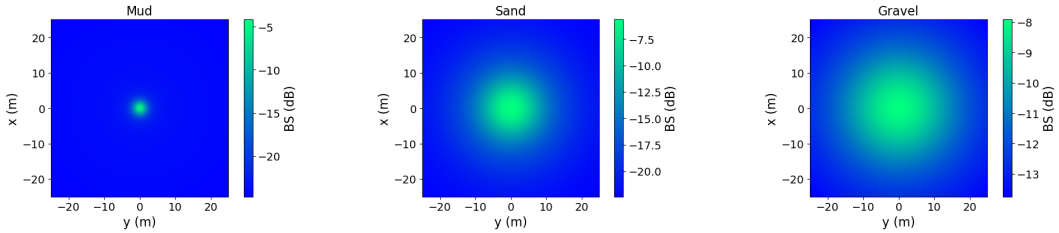

(a) (b) (c)

Figure 5.6: BS functions for (a) muddy seafloor (density: $2500kg \cdot m^{-2}$, sound speed: $2700m \cdot s^{-1}$, attenuation coefficient: $5dB \cdot m^{-1}$, spectral strength: $0.016cm^4$, spectral exponent: 3.25), (b) sandy seafloor (density: $1500kg \cdot m^{-2}$, sound speed: $1767m \cdot s^{-1}$, attenuation coefficient: $9dB \cdot m^{-1}$, spectral strength: $0.004446cm^4$, spectral exponent: 3.25), (c) gravelly seafloor (density: $1146kg \cdot m^{-2}$, sound speed: $1474m \cdot s^{-1}$, attenuation coefficient: $1.1dB \cdot m^{-1}$, spectral strength: $0.000518cm^4$, spectral exponent: 3.25)

For this study, square apertures are considered with three aperture sizes ($a =$

$0.1m$, $a = 1m$ and $a = 5m$). An aperture of $a = 0.1m$ corresponds to an almost omnidirectional transducer. On the contrary, an aperture $a = 5m$ corresponds to a very directive transducer. Directivities projected onto seafloor for such apertures are presented on Figure 5.7. Numerical integration of the analytical model is then performed neglecting propagation losses and defining time interval $[t_i, t_f]$ such as $t_i < \frac{2z}{c}$ and t_f large enough so that the contributing portion of the seafloor is not limited by the masking function. Under these assumptions, seafloor equivalent source characteristics are only dependant on the combination of directivity and backscattering functions projected onto seafloor.

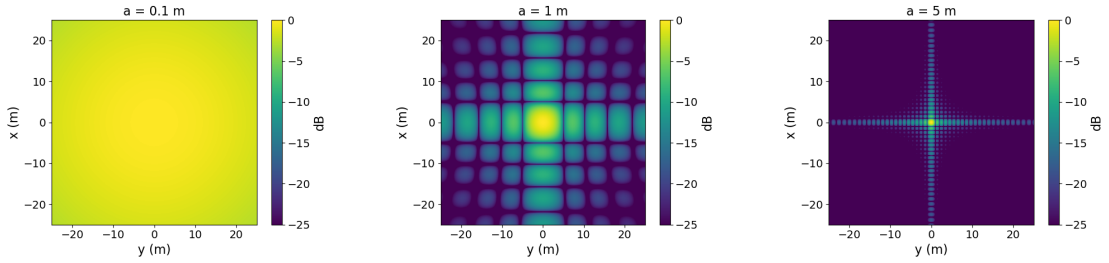

(a) (b) (c)

Figure 5.7: Square aperture transducer directivities projected onto seafloor (a) $a = 0.1m$ - (b) $a = 1m$ - (c) $a = 5m$

Results of the numerical integration of the analytical model for all possible directivity/sediment type combinations are presented on Figure 5.8. Coherences computed with muddy sediment are represented with blue curves, those computed with sandy sediment are represented by red curves and those computed with gravelly sediment are represented by green curves. On the contrary, the curves calculated from the different apertures are plotted with different types of line (dot line curves for $a = 5m$, star line curves for $a = 1m$ and cross line curves for $a = 0.1m$). Analysis of these results highlights the combined effect of directivities and scattering terms. Indeed, in the case of the muddy seafloor (blue curves), whose backscattering function falls very quickly even at small pointing angles, the antenna aperture parameter seems to have very little influence on the coherence length. Unlike the case of the gravelly seafloor (green curves) that shows important variations in coherence as a function of antenna aperture. This can be explained by the fact that in the case of muddy seafloor, the backscattering capacity of the seafloor is limited at near nadir incidence, so a decrease in antenna directivity does not result in an increase in the size of the portion of the seafloor contributing to the backscattered signal. In other words,

whatever the aperture of the antenna studied, the extent of the seafloor equivalent source is limited by the backscattering capacity of the seafloor. On the contrary, in the case of gravelly seafloor, the seafloor retains its ability to backscatter energy, even for incidence far from nadir. In this case, any change in the aperture of the antenna leads to a change in the extent of energy distribution on the seafloor and in the case of very directive antennas it is the aperture of the antenna and no longer the backscattering capacity of the seafloor that will limit the extent of the seafloor equivalent source and therefore increase the coherence length. This point is also illustrated by the coherence curves obtained for sand and gravel sediments for an aperture $a = 5m$ (red and green dot-line curves). In these cases, whatever the type of sediment (sand or gravel), the coherence length appears to be the same. This is because in these cases the antennas are so directional that it is this parameter that restricts the extent of the seafloor equivalent source. Nevertheless, we notice that in the case of a muddy sediment (blue dot-line curve), the coherence length is increased. This is because, in this case, the backscattering capacity of the seafloor for incidences far from nadir is so low that it limits the extent of the seafloor equivalent source even more than the directivity and increases the spatial coherence by the same amount.

We can also see that the shape of the coherence figures is not triangular, as has been suggested so far for linear apertures. This is particularly noticeable for the large apertures on sandy and gravel seafloors (red and green cross-line and star-line curves). Indeed, as we have just said, in such cases the extent of the seafloor equivalent source is limited by the directivity of the sensors (large apertures), but the distribution of intensity re-emitted by the seafloor is apodised by the scattering function, the shape of which for incidences close to nadir can be approximated by a gaussian function.

We have seen in this part that an environmental parameter (the scattering function) or a system parameter (the antenna aperture) modifies the extent and energy distribution of the seafloor equivalent source and therefore has an impact on the spatial coherence observed by the system. The masking function, which is a processing parameter (it depends on the time interval over which coherence is evaluated), can also limit the extent of the seafloor equivalent source and therefore modify coherence. Its influence is highlighted in the following paragraph.

5.2.3 Study of the influence of the masking function

Just as in the previous section we studied the combined influence of the aperture and the nature of the seafloor, we propose here to highlight the influence of the time window $[t_i, t_f]$ over which coherence is estimated with respect to the directivity parameter. To do so, two time windows and three apertures are considered. Time windows are

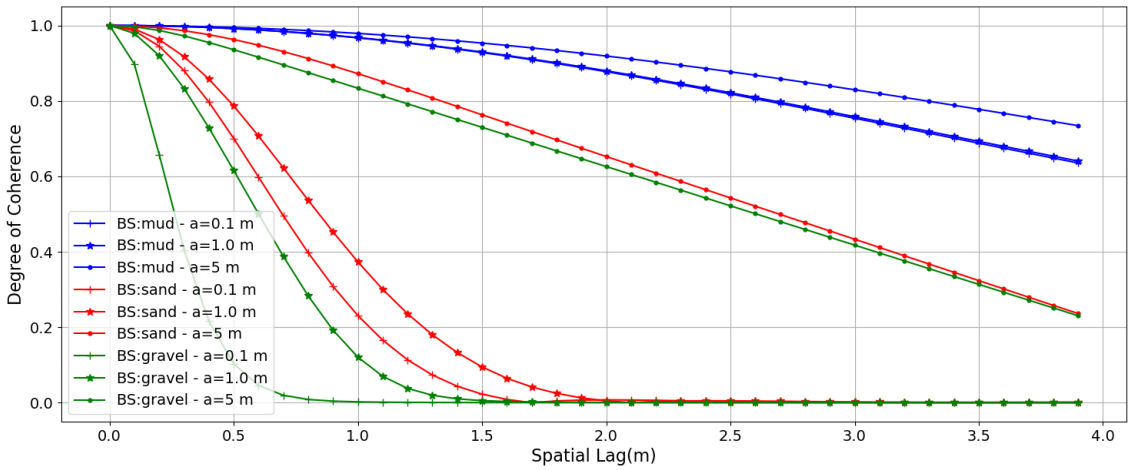

Figure 5.8: Degree of coherence computed by numerical integration of the analytical model for different directivity/sediment type combinations

set so that the masking function projected onto the seafloor is a circle ($t_i < \frac{2z}{c}$) and the diameter of this circle is limited by t_f ($t_f = 0.06734s$ and $t_f = 074s$ are used for this example). Three square apertures resulting in a cardinal sine directivity are used for this example ($a = 0.3m$, $a = 0.6m$ and $a = 1.5m$). Distributions of energy of the seafloor equivalent source are represented on Figure 5.9. The example of a very directive sensor $a = 1.5m$ and a broad masking function ($t_f = 074s$) is given on Figure 5.9(c-2). In such a case, one can see that the cardinal sine directivity projected on seafloor is well developed inside the masking function (at least 5 secondary lobes are visible) and so the result of the numerical integration of this example should be close to the theoretical case 2, in which we made the hypothesis of a masking window large enough so that the contributing portion of the seafloor is limited by the directivity and not by the masking function. The opposite extreme of this example is represented on Figure 5.9(a-1) for which a sensor with low directivity ($a = 0.3m$) and a limited masking window ($t_f = 0.06734s$) are used. In such a case, one can see that the cardinal sine directivity projected on seafloor can not be developed inside the masking function (the entire main lobe is not visible) and so the result of the spatial coherence predicted by numerical integration of the model is expected to be increased compared to that which would have been obtained with a wider time window.

Results of the numerical integration of the analytical model for all possible directivity/time windows combinations are presented on Figure 5.10. Coherences

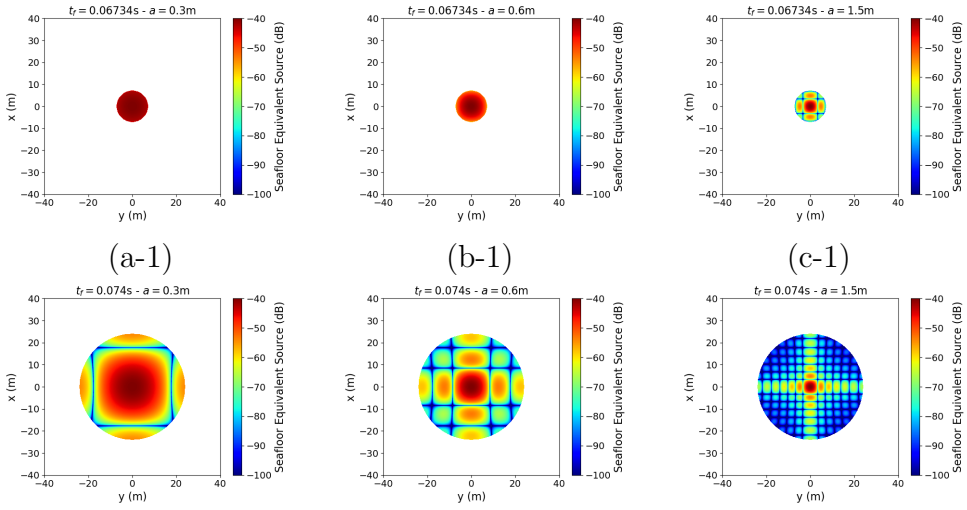

Figure 5.9: Distributions of the energy of the seafloor equivalent source for different apertures a (row-wise) and different time windows $[t_i, t_f]$ (column-wise). Time windows are set so that the masking function projected onto the seafloor is a circle ($t_i < \frac{2z}{c}$) and the diameter of this circle is limited by t_f. (a-1) $t_f = 0.06734s$ and $a = 0.3m$ - (b-1) $t_f = 0.06734s$ and $a = 0.6m$ - (c-1) $t_f = 0.06734s$ and $a = 1.5m$ - (a-2) $t_f = 0.74s$ and $a = 0.3m$ - (b-2) $t_f = 0.74s$ and $a = 0.6m$ - (c-2) $t_f = 0.74s$ and $a = 1.5m$.

computed with wide masking function ($t_f = 0.74s$) are represented with red curves, and those computed with limited masking function ($t_f = 0.06734s$) are represented by blue curves. On the contrary, the curves calculated from the different apertures are differentiated by the type of line (dot line curves for $a = 1.55m$, star line curves for $a = 0.6m$ and cross line curves for $a = 0.3m$). Analysis of these results highlights the combined effect of directivity and time windowing terms. Indeed, let's first have a look of very directive sensor example (dot-line curves - $a = 1.55m$). The temporal windowing does not seem to have a major influence on the observed coherence, and a coherence length of 1.5m as predicted by the VCZ theorem is observed. The triangular shape of the coherence figure predicted by the VCZ theorem is nevertheless better observed in the case of a large masking function (red curve) than in the smaller one (blue curve). Compared with the energy distribution of seafloor equivalent sources shown on Figures 5.9(c-1) and 5.9(c-2), this illustrates the fact that for large apertures, the size of the temporal window (provided that it is not too small either) has little

influence on the observed coherence, since it is rather the directivity projected onto the seafloor that tends to limit the extent of the seafloor equivalent source. We can also see that integration over a cardinal sine developed to its 5th lobe allows us to observe the triangular shape of the coherence figure predicted by the VCZ theorem. Integration on the cardinal sine developed up to its first lobe does not affect the coherence length (we still observe a coherence length proportional to the aperture of the sensors), but modifies the shape of the curve (we no longer obtain a triangle). In the case of the intermediate aperture and large time windowing (red star-line curve - $a = 0.6m$ and $t_f = 0.74s$), coherence length and shape of the figure of coherence are in accordance with the VCZ theorem (triangular shape and $0.6m$ coherence length). Comparison with the energy distribution of the seafloor equivalent source shown in Figure 5.9(b-1) shows that the integration on a cardinal sine developed up to third lobes is sufficient to converge to the VCZ theorem (it seems to be close to the acceptable limit as the form is no longer strictly triangular). However, in the case of the intermediate aperture and small time windowing (blue star-line curve - $a = 0.6m$ and $t_f = 0.06734s$), coherence curve computed by numerical integration of the analytical model is no longer in accordance with the VCZ theorem as the shape of the curve is no longer triangular and the coherence length is increased. This increase, due to the reduction in the time window, is even more marked in the case of a small sensor aperture. Indeed, comparison between coherence curves estimated on wide beam sensors with short time windowing (blue cross-line curve) and long time windowing (red cross-line curve) shows an increase of coherence length of nearly $0.2m$. This increase in coherence length is explained by the reduction in the extent of the seafloor equivalent source by the masking function. Indeed one can see on Figure 5.9(a-1) that the extent of the seafloor equivalent source is non longer limited by the cardinal sine directivity but mostly by the masking function. Contribution of the seafloor to the coherence is limited to only part of the main lobe of the directivity. Moreover, coherence curve estimated on wide beam sensors with short time windowing (blue cross-line curve) shows oscillations for inter-sensor distances at which zero coherence is expected. These oscillations are related to Gibbs phenomenon wich occurs for Fourier representation at discontinuities [Brown, 2017].

In a similar way to the combined effect of antenna aperture and seafloor backscattering capacity on coherence studied in the previous section, this section highlights the combined influence of antenna aperture and the time window used to estimate coherence.

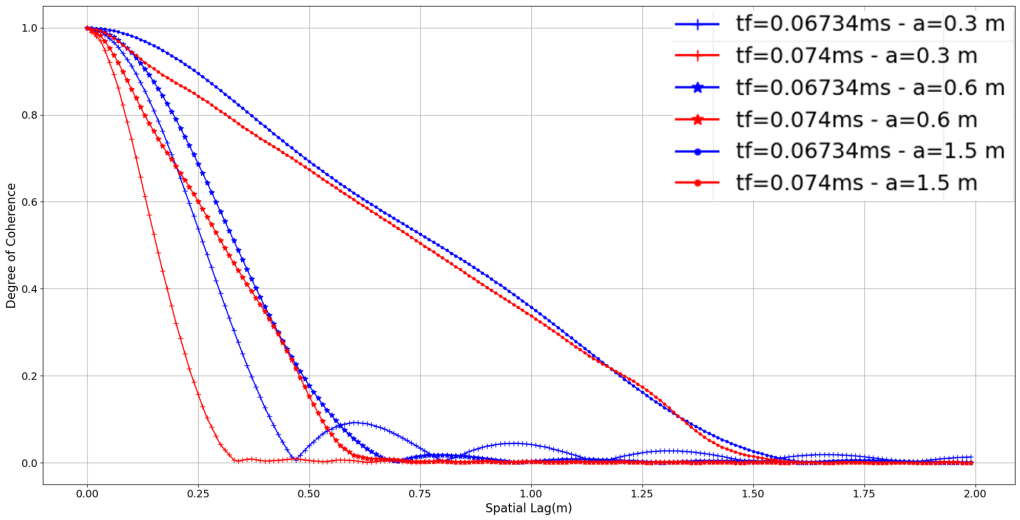

Figure 5.10: Degree of coherence computed by numerical integration of the analytical model for different directivity/time windows combinations.

5.3 Numerical modelling

The numerical resolution of the analytical models was satisfactory in the down-looking geometry. Carrying out the same analysis for side-looking geometry wouldn't make much sense, because in side-looking geometry, coherence remains highly dependent on geometric decorrelations (stretching and mismatch footprint in particular) induced by the observation geometry. In order to introduce these phenomena into the study, the signals are modelled numerically using the point-based scattering model. By using the simulated signals simulated in this way, coherences are estimated before and after compensation for geometric geometric phenomena.

5.3.1 Computation details

Signals computation

The model used for these simulations is the finite scatterer model commonly used in radar field to model target reflexion [Haimovich et al., 2008]. In [Pailhas et al., 2017] a reformulation of the previous model is proposed in order to suit for broadband sonar systems. In [Brown et al., 2017], the finite scatterer model is applied for calculation of the incoherent component of the field scattered from random rough surfaces. To

do so, a rough surface is represented with a fix number of scattering points spatially and randomly distributed. For a narrow band signal, and using the same notations as those used in chapter 4.1.1, the contribution of a scatterer $\bar{X}$ at position (x, y, d), insonified by a transmit device at position Q_T and sensed at position Q_R can be expressed by:

$$s_r\left(\bar{X}, t\right) = \zeta(\bar{X})\chi_R(\bar{X})\chi_T(\bar{X})\sigma(\bar{X})s_0\left(t - \frac{r_t(\bar{X}) + r_r(\bar{X})}{c}\right) \tag{5.8}$$

For broadband signal, such a contribution can be expressed in the frequency domain by:

$$S_r\left(\bar{X}, \omega\right) = \zeta(\bar{X}, \omega)\chi_R(\bar{X}, \omega)\chi_T(\bar{X}, \omega)\sigma(\bar{X}, \omega)S_0\left(\omega\right)e^{-j\omega\frac{r_t(\bar{X})+r_r(\bar{X})}{c}} \tag{5.9}$$

By modelling the seafloor by a number N of scattering elements, signal sensed at position Q_R from the N scattering elements insonified by a narrowband source at position Q_T is obtained by summing all scattering elements:

$$s_r\left(t\right) = \sum_{i=1}^{N} \zeta(\bar{X}_i)\chi_R(\bar{X}_i)\chi_T(\bar{X}_i)\sigma(\bar{X}_i)s_0\left(t - \frac{r_t(\bar{X}_i) + r_r(\bar{X}_i)}{c}\right) \tag{5.10}$$

and for broadband sources, the spectrum of the received signal is given by

$$S_r\left(\omega\right) = \sum_{i=1}^{N} \zeta(\bar{X}_i, \omega)\chi_R(\bar{X}_i, \omega)\chi_T(\bar{X}_i, \omega)\sigma(\bar{X}_i, \omega)S_0\left(\omega\right)e^{-j\omega\frac{r_t(\bar{X}_i)+r_r(\bar{X}_i)}{c}} \tag{5.11}$$

Note the strong similarity between the equation (5.10) and equation (4.5). The first difference is that the equation (4.5) is established for a phase centre, while the equation (5.10) is established for a non-collocated transmitter and receiver. Under PCA approximation, term $r_t(\bar{X}) + r_r(\bar{X})$ of equation (5.10) reduces to $2r(\bar{X})$ as in equation (4.5), and writing χ, the combination of the transmit/receive directivities $\chi = \chi_R \cdot \chi_T$, equation (5.10) becomes:

$$s_r\left(t\right) = \sum_{i=1}^{N} \zeta(\bar{X}_i)\chi(\bar{X}_i)\sigma(\bar{X}_i)s_0\left(t - \frac{2r(\bar{X}_i)}{c}\right) \tag{5.12}$$

Finally, the remaining difference between the equation (5.12) and PCA signal modelling of equation (4.5) is the discrete sum $\sum_{i=1}^{N}$ replacing the integral $\int_{\bar{X}}$. In this sense, finite scatterer modelling can be seen as a discretisation of the scattering surface.

Thanks to its mathematical simplicity, this kind of modelling allows efficient parallel implementation, but the number of scatterers N used remains a critical parameter. In [Brown et al., 2017] a scatterer density of 7.5 scatterers per wavelength is used (in accordance with density given in [Pouliquen et al., 1999]). Thus simulation of the field scattered from large areas at high frequencies can result in very time-consuming simulations.

In addition of the number of scatterers, we also need to consider the size of the surface over which the scattering elements are dispersed. In fact, it is important to spread the scattering elements over a large enough area to take into account all the contributions to the signal. The size of this area depends firstly on the aperture of the antenna (the larger the aperture of the antenna, the smaller the scattering area) and the range at which coherence is estimated (the larger the range, the larger the scattering area). Indeed, at a given range, an antenna with a small aperture will produce a wider beam and will therefore require more extensive meshing of the scattering zone than an antenna with a larger aperture. Similarly, for a given antenna aperture, the beam's footprint on the seafloor will be smaller at short range than at long range, and will therefore require less extensive meshing of the scattering zone. Figure 5.11 shows the influence of the antenna aperture and the range on the extent of the scattering area to be meshed is illustrated. The directivity projected on scatterers is represented by coloured dots for two different gaussian apertures: a 'small' aperture antenna ($\alpha_y = 3°$) on Figure 5.11(a) and a 'large' aperture antenna ($\alpha_y = 5°$) on Figure 5.11(b). One can see that for a 'small' aperture antenna (Figure 5.11(a)), at short range (blue curves delimit ranges between 25 and $30m$), the scatterers furthest from the main direction of insonification contribute very little to the total signal (less than $-10dB$), so the integration can be considered as total. On the contrary, at larger ranges (red curves delimit ranges between 25 and $30m$), the scatterers furthest from the main direction of insonification can contribute significantly to the total signal (around $-4dB$), and the mesh proposed in the figure is not large enough to fully model the various elements contributing to the received signal. Such a reduction in the extent of the scattering surface is similar to a small masking function as studied in section 5.2.3 and would result in a change in the size of the coherence figure, which would be caused by a default in the modelling, which is clearly undesirable. On the contrary, for a sensor with a more narrow directivity beam (Figure 5.11(b)), even at large ranges, the scatterers furthest from the main direction of insonification contribute very little to the total signal (less than $-10dB$), so the integration can be considered as total. To summarize this point, a certain density (with respect to wavelength) of scatterers has to be respected, and in order not to increase the number of scattering elements modelled by too much, it is useful to restrict the mesh space

for the simulation. However, care must be taken not to restrict this space too much, otherwise the coherence observed will be altered. This is why, in the analyses that follow, considered rather low-frequency signals (long wavelength) with rather high directivities, while remaining within moderate ranges.

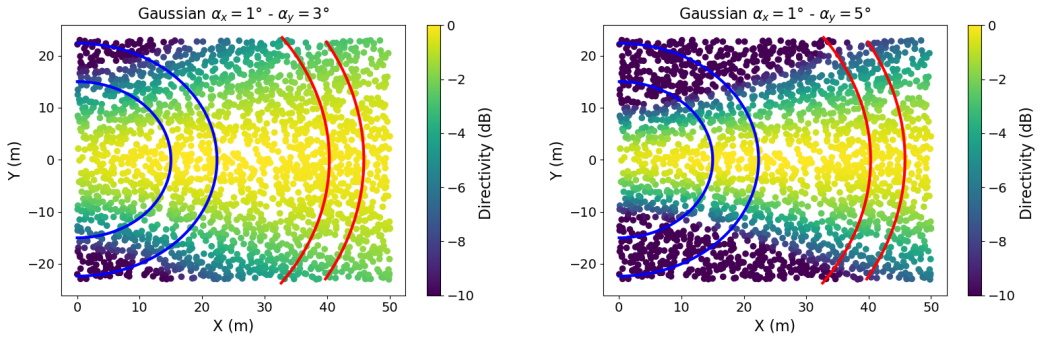

(a) (b)

Figure 5.11: Illustration of the influence of antenna aperture and range on the extent of the scattering area to be meshed. Directivity projected on scatterers is represented by coloured dots. Spatial windowing corresponding to the range interval $[25m, 30m]$ is represented by blue curves. Spatial windowing corresponding to the range interval $[45m, 50m]$ is represented by red curves (a) 'Small' aperture antenna ($\alpha_y = 3°$) - (b) 'Large' aperture antenna ($\alpha_y = 5°$).

Back onto equation (5.12), a word can be said about the numerical modelling of the different terms. This modelling is quite similar to that used in the previous sections:

- **Transmission losses** $\zeta(\bar{X}_i)$: Assuming spherical propagation and writting ζ_0 the absorption coefficient, transmission losses can be expressed by :

$$\zeta(\bar{X}_i) = \frac{e^{-\zeta_0 \cdot r(\bar{X}_i)}}{r^2(\bar{X}_i)} \tag{5.13}$$

- **Combined transmit/receive directivity** $\chi(\bar{X}_i)$: The combined transmit/receive directivity $\chi(\bar{X}_i)$ is function of the directivity of the transmit device χ_T and the directivity of the reception device χ_R. For the ease of interpretation, one will assume small reception elements such as $\forall \bar{X}, \quad \chi_R(\bar{X}) = 1$ and thus combined transmit/receive directivity reduces to the directivity of the transmit

device. This directivity is function of frequency and transmit antenna aperture. For this study, two antenna apertures are used: a gaussian aperture and a rectangular one. Corresponding directivities functions are given in the down looking configuration by equation (4.49) for the rectangular aperture and by equation (4.59) for the gaussian aperture. In side looking observation geometries, acquisition and reception devices are often tilted at a given angle from the vertical direction in order to orientate the directivity lobe.

- **Backscattering term** $\sigma(\bar{X}_i)$: As already expressed previously, the Jackson model [Jackson et al., 1986], valid at frequencies between 10 and 100 kHz, can provide backscattering coefficient σ_0. In order to ensure an incoherent field, a phase factor is added [Brown et al., 2017]. It is given by $\frac{X+iY}{\sqrt{2}}$ where X and Y are independently distributed normal random variables. Moreover, a scale factor $\frac{E}{N}$ where E is the total amount of transmitted energy and N the number of scatterer is used in order to ensure that whatever the number of scatterer used, the same amount of energy is used. Finally, backscattering term $\sigma(\bar{X}_i)$ can be written:
$$\sigma(\bar{X}_i) = \frac{E}{N}\frac{(X+iY)}{\sqrt{2}}\sigma_0(\bar{X}_i) \tag{5.14}$$

- **Pulse signal** s_0: A CW signal is used here. One remind that this signal is defined by a central frequency f_0 and a pulse length T. Such a signal is given by:
$$s_0(t) = \Pi_T(t)e^{j(2\pi f_0 t)} \tag{5.15}$$

To illustrate, a simulation is conducted using a Gaussian aperture transmit antenna tilted at 45°. Transmit directivity projected onto a set of scatterers is represented on Figure 5.12(a). Backscattering coefficient σ_0 of the same set of scatterers is represented on Figure 5.12(b) for a gravelly seafloor. The simulated signal is represented on Figure 5.12(c). For this simulation a CW pulse with parameters $T = 100\mu s$ and $f_0 = 15kHz$ is used. A phase center with gaussian aperture of parameters $\alpha_x = 1°, \quad \alpha_y = 5°$ tilted at 45° is placed $20m$ above of a gravel seafloor. Simulation is based on narrow band assumptions and so directivity and seafloor scattering are assumed to be constant over the signal bandwidth and are computed at f_0. Narrow band sonar equation can provide the expected level of the backscattered field. This level is represented by the orange curve on Figure 5.12(c). One can notice good agreement between expected level provided by the sonar equation and simulated signal level especially with increasing range. That comes from the fact that the term of insonified area in the sonar equation was computed under oblique incidence assumption that was not respected at ranges close to the nadir.

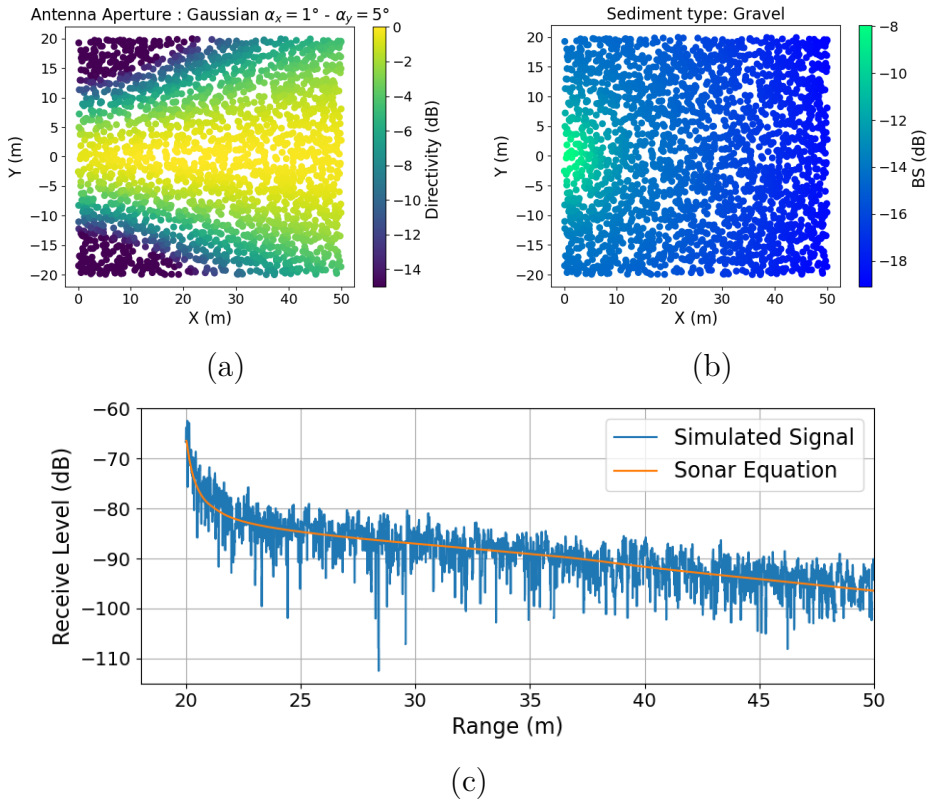

Figure 5.12: Illustration of the signal simulation process based on finite scatterer model - (a) Transmit/ receive directivity projected on scatterers $\chi(\bar{X}_i)$ for a gaussian aperture source with parameters $\alpha_x = 1°$ and $\alpha_y = 5°$ tilted at 45° from the vertical - (b) Scatterers backscattering strength $\sigma(\bar{X}_i)$ (Note that for the ease of illustration, scatterer density is reduced on this illustration) - (c) Narrow band simulated signal (blue curve) compared to the narrow band sonar equation (orange curve)

Coherence computation

In the previous section, we explained how to simulate signals based on the position of a phase centre, its aperture and a set of scattering elements meshing the seafloor. In order to estimate the spatial coherence at a given spatial lag Δ, a pair of signals are simulated for two phase centers positioned on either side of the origin as represented on Figure 4.2. The scattering elements meshing the seafloor are randomly distributed according to a uniform distribution, which makes it possible to generate independent seafloor realisation.

Writing $s^{+}_{rep}(\Delta, t)$ and $s^{-}_{rep}(\Delta, t)$ the two signals simulated respectively at positions $+\Delta/2$ and $-\Delta/2$ with a seafloor realisation rep, coherence estimate is computed by:

$$\hat{\rho}\left(\Delta, [t_i, t_f]\right) = \frac{1}{N_{rep}} \sum_{i_{rep}=1}^{N_{rep}} \int_{t_i}^{t_f} s^{+}_{rep}(\Delta, t) s^{-^*}_{rep}(\Delta, t) dt \tag{5.16}$$

with N_{rep} the number of seafloor realisations and $[t_i, t_f]$ the time interval over which the coherence is estimated.

5.3.2 Along track coherence analysis

In this section, we present the results of simulations demonstrating the influence of the aperture of the transmitting antenna on the along-track coherence, and we provide a comparison with results from a HRLFSAS dataset.

Aperture influence

Let's first consider a set of phase centers distributed in the along track direction and with a Gaussian aperture as defined in part 4.3.5. Signals are modelled and degree of coherence is estimated according to procedure introduced in part 5.3.1. Figure 5.13 shows a comparison between simulated coherence and the analytical coherence modelled by equation (4.83). Three different apertures are compared: $\alpha_y = 15°$, $\alpha_y = 30°$, $\alpha_y = 50°$. Curves show good agreement between simulated and modelled coherence for all the studied apertures. Nevertheless, we note that in the case of large inter-sensor distances, the one for which the expected level of coherence is zero, the bias of the coherence estimator studied in part 3.3.3 shows non-zero simulated coherences as the coherence estimation procedure for modelled signals (part 5.3.1) is the same as the one introduced in part 3.3.1 for real signals. On the contrary, the analytical modelling of coherence does not present this bias. This agreement between the simulated coherence and that modelled analytically confirms the relevance of the simulation and, in particular, that the distribution and density of the scattering elements are sufficient for the study of coherence for the geometry and apertures considered.

Comparison to HRLFSAS

Still in the study of coherence in the along-track direction, we showed in part 3.4.2 that the VCZ theorem predicts well the size and shape of the coherence pattern observed with the horizontal antenna of the HRLFSAS system. We then showed

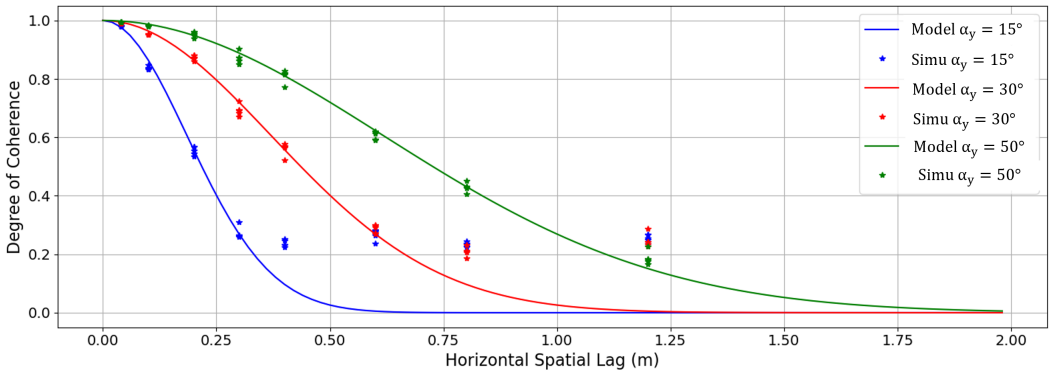

Figure 5.13: Comparison between simulated and modelled degree of coherence for three different Gaussian apertures ($\alpha_y = 15°$, $\alpha_y = 30°$, $\alpha_y = 50°$)

analytically (part 4.3.5) that in the side-looking geometry, under some hypotheses, coherence in the along-track direction is well modelled by an expression equivalent to the VCZ. This result was confirmed by simulation in the previous section for Gaussian apertures. In this section, we compare the simulated coherences with the along-track coherence observed by the HRLFSAS horizontal antenna. To do this, we have considered a linear emission aperture of length $L = 25cm$ and point receivers. We also considered narrow-band signals with a centre frequency of $f_0 = 15kHz$. Simulated and observed along track coherence are represented on Figure 5.14. Curves show good agreement between simulated and observed coherence. The size and triangular shape of the figure are consistent with those predicted by the VCZ theorem. We note that the same bias is observed for large inter-sensor distances for which the expected coherence is zero (for spatial lags greater than 25 cm). We can also see that for a zero inter-sensor distance, the coherence is not equal to 1, due to the influence of a degraded signal-to-noise ratio as presented in the section 3.3.4.

5.3.3 Across track coherence analysis

In this section, we present the results of simulations relating to the study of coherence in the across-track direction. Let's first consider a set of phase centers distributed in the across track direction. These sensors have a Gaussian aperture (along track aperture) as defined in part 4.3.5. Signals and the degree of coherence are estimated according to procedure introduced in part 5.3.1. As we saw in the introduction of this chapter (see part 5.1), when the sensors are separated in the across-track direction,

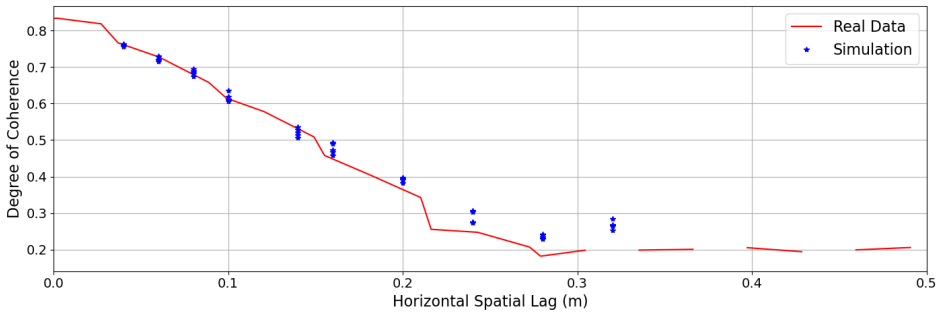

Figure 5.14: Comparison between along-track coherence observed thanks to the horizontal antenna of the HRLFSAS system and simulated coherence with antenna and signal parameters as defined in part 3.4.2 (linear antenna of length $L = 25cm$ and central frequency of $f_0 = 12kHz$).

the difference in points of view leads to geometric decorrelations which reduce the length of coherence. This point is highlighted on Figure 5.15. On this figure, the coherence as a function spatial lag x_0 for different focusing points x_{min} is represented in three cases: without any geometric compensation (left), with mismatch footprint compensation (middle) and with mismatch footprint and stretching compensation (right). This simulation was conducted with very directive sensors ($\alpha_y = 20°$) and so all the contributing scatterers are concentrated around the across track axis $\vec{x}$. One can note that in the absence of any compensation for geometric decorrelations (left), the coherence lengths are the same whatever the focus point x_{min}. Moreover, these coherence lengths are much lower than those predicted by the analytical model (see Figure 4.11). We can see that after compensation for the mismatch footprint (as presented in part 5.1.3), coherence levels are significantly enhanced. However, we can see that for small values of x_{min}, i.e. large incident angles, the coherence levels are not enhanced to the same level as those for the large x_{min} values. This can be explained by the fact that for large values of incident angles, the decorrelation induced by stretching is significant, whereas for smaller values of incidence, the decorrelation produced by the mismatch footprint predominates. It is important to note that this result is in accordance to the observation made in [Synnes et al., 2021]. Finally, after stretching compensation (in addition of mismatch footprint compensation as introduced in part 5.1), the level of coherence is almost 1 for all values of x_0.

Another simulation has been conducted using sensors with wider directivity lobes ($\alpha_y = 5°$) and so in this case, the contributing scatterers are no longer concentrated

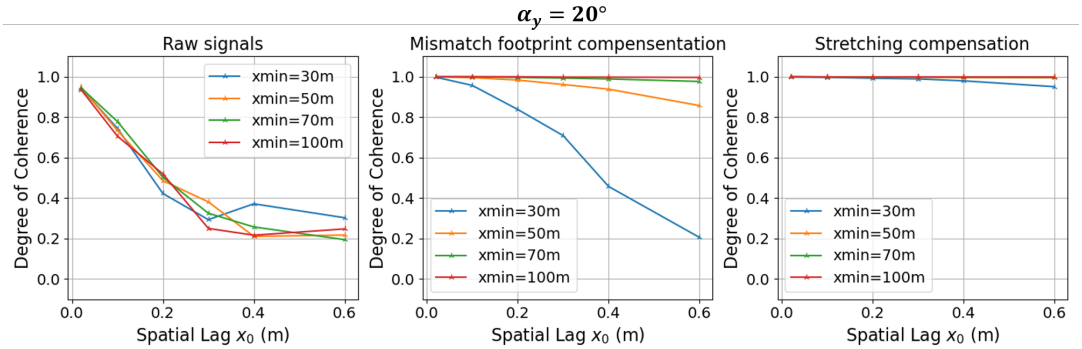

Figure 5.15: Coherence as a function spatial lag x_0 for different focusing points x_{min} without any geometric compensation (left), with mismatch footprint compensation (middle) and with mismatch footprint and stretching compensation (right). Along track aperture was set to 20°.

around the axis $\vec{x}$ but are spread over a much wider area. Across track spatial coherence is represented on Figure 5.16 for different focusing points x_{min} without any geometric compensation (left), with mismatch footprint compensation (middle) and with mismatch footprint and stretching compensation (right). Similarly to what was observed in the case of highly directional sensors, without geometric correction, coherence is strongly reduced by geometric decorrelations, in the same proportions for the two studied apertures. Similarly, after compensating for the mismatch footprint, coherence is kept for larger spatial lags but we still observe the dominant influence of stretching at high incidence. Finally, it is after compensation for mismatch footprint and stretching that significant differences appear between the coherences observed for different apertures. By comparing the figures 5.16 and 5.15, we observe that after compensation for stretching, whatever the focus point x_{min}, the coherence observed is greater in the case of the directional sensor. This is in line with the observation made in the analysis of the analytical model (see part 4.3.5), where we linked coherence losses in the across-track direction to the difference in curvature of the wavefronts in the directivity lobe of the transducer.

5.4 Chapter summary

In this chapter, we have carried out a numerical study of spatial coherence. This numerical study is based on two methods. First, a numerical integration of the

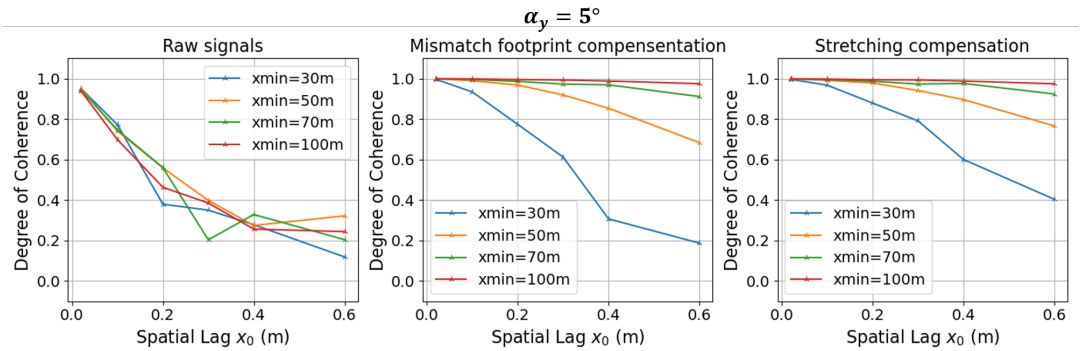

Figure 5.16: Coherence as a function spatial lag x_0 for different focusing points x_{min} without any geometric compensation (left), with mismatch footprint compensation (middle) and with mismatch footprint and stretching compensation (right). Along track aperture was set to 5°.

equation 4.31 for the down-looking geometry. In particular, modelling the scattering term using the Jackson model for muddy, sandy and gravelly sediment allowed us to show combined effect of directivity and seafloor scattering capacity (see part 5.2.2). Similarly, we highlighted the combined influence of the time window $[t_i, t_f]$ over which coherence is estimated with respect to the directivity parameter (see part 5.2.3). The conclusion of these two analyses is common and is well described by the VCZ theorem in its 'optical formulation', insofar as the time window, the scattering term and the directivity all contribute to define the size and intensity distribution of the seafloor equivalent source and therefore the coherence. So if one of these three parameters is more restrictive than the others (for example, a highly directional sensor) then it is this parameter that will determine the coherence length. On the other hand, a parameter that does not limit the extent and does not modulate the energy distribution of the seafloor equivalent source (e.g. a large time window) will have no impact on the observed coherence.

The numerical resolution of the analytical model was satisfactory in the down-looking geometry, but in the side looking geometry the geometric decorrelation phenomena not taken into account in the analytical model led us to propose a numerical modelling of the temporal signals from which the coherences are estimated. This numerical modelling of the signals, which is closer to the actual acquisition geometry, is the second point in the numerical study of coherence and was presented

in the section 5.3. In the along-track direction, the coherence calculated on signals simulated with several Gaussian apertures confirmed the results of the analytical modelling, namely that coherence in the along-track direction is well described by the VCZ theorem. In the across track direction, we studied the evolution of coherence as a function of the position of the focal point and the sensor along-track aperture. This analysis on spatial coherence in the across-track direction showed that:

- in the absence of geometric corrections, coherence in the across-track direction is severely limited, whatever the position of the focal point and whatever the aperture of the sensors;
- after correcting for the footprint mismatch, the coherence levels are significantly improved whatever the aperture of the sensors, and especially when the angle of incidence is low. This highlights the importance of stretching at high incidence angles.
- after correcting for the footprint mismatch and stretching, we observe that, whatever the focal point, the coherence observed is greater in the case of the directional sensor. This is in line with the observation made in the analysis of the analytical model, where coherence losses in the across-track direction has been linked to the difference in curvature of the wavefronts in the directivity lobe of the transducer.

Chapter 6

Conclusion and Future works

6.1 Summary of results

This document presents a study of spatial coherence of an acoustic field scattered by the seafloor. In the field of sonar, the notion of spatial coherence is crucial. Spatial coherence is exploited by Correlation Velocity Logs (CVL) and SAS systems to estimate antenna displacement between successive sonar recursions, respectively to estimate carrier velocity or to focus SAS images. This notion is also necessary for interferometric systems to estimate the direction of arrival (DoA) of an acoustic wave on a receiving device. So it appears that spatial coherence plays a fundamental role in the sonar's ability to detect, locate and characterise underwater objects in a wide variety of maritime and underwater applications, and first and foremost mine countermeasures.

SAS systems are increasingly used in the mine countermeasure domain as they can produce images of the seabed with range-independent and frequency-independent resolution. With conventional sidescan sonars, the choice of sonar frequency depends mainly on the range and resolution required. This raised the question of what frequency to use for SAS mine warfare systems. Market research shows that the solution has been to use frequencies that are rather high compared with the size of the objects sought (>150kHz, generally around 300kHz), mainly for reasons of interpretability of the sonar images produced. In addition to resolution, high-frequency SAS systems enable images to be obtained with a very high contrast between target echoes, projected shadows and the surrounding seabed. These image characteristics are used by mine countermeasures operators or by automatic recognition algorithms to distinguish a threat (a mine, for example) from a rock on the seabed. However, these HF SAS

systems suffer from two major limitations: firstly, they are completely ineffective on buried objects, and secondly, their performance drops when the objects are partially buried or when the seabed is studded with rocks of a size and shape compatible with a mine (cluttered environment). To deal with this issue low-frequency SAS systems are currently being developed. Because it penetrates the sediment, the use of low-frequency waves should enable buried objects to be detected. In addition, the use of low-frequency waves should also make it possible to exploit the elastic scattering of a target and thus discriminate between objects of the same shape but with different internal compositions.

The fundamental bases of the concept of spatial coherence are presented in chapter 3 and consists of the Van Cittert Zernike (VCZ) theorem. Originally defined in the field of statistical optics, this theorem states that in the far field of an incoherent surface, spatial coherence is proportional to the 2D Fourier transform of the intensity distribution of the surface. This formulation of the VCZ theorem, referred to as the 'Optical formulation' in this document, tells us that a broad intensity distribution will produce a wavefield with narrow spatial coherence, and conversely, a narrow intensity distribution will produce a wavefield with broad spatial coherence. However, despite of the clear interest of the VCZ in its 'optic formulation', its application to the sonar domain is not straight forward given that acoustic sources produce coherent acoustic field. However, under some assumptions, it is applicable to an acoustic field scattered by an incoherent medium. That leads to another formulation of the VCZ theorem, referred to as the 'acoustic formulation' in this document, that states that in the far field of an incoherent scattering medium insonified by an acoustic source, spatial coherence is proportional to the autocorrelation of the source aperture. Established under strong assumptions, these two forms of the theorem VCZ provide an intuitive view of spatial coherence. In this thesis, analytical modelling and numerical simulations have been conducted in order to provide rigourous illustrations of the spatial coherence and discuss the theory of the VCZ theorem for active sonar and to take into account physical processes (absorption, seafloor scattering capacity), hardware and computational parameters (sonar aperture, transmit signal and temporal windowing).

The development of an analytical model of spatial coherence is presented in chapter 4. For this purpose, the study has been separated into two acquisition geometries:

- **Down-looking geometry:** Receivers are assumed to laid on the same plan parallel to the seafloor. The depth is considered to be greater than the other dimensions of the problem, in particular the size of the observation zone (i.e. the distance between the receivers) and the extent of the scattering area (i.e.

high directivity beams).

- **Side-looking geometry:** In such a case, sensors are assumed to be fully opened in the vertical plane. Moreover, scattering and transmission losses terms are assumed not vary greatly over the portion of the seafloor covered during the time interval $[t_i, t_f]$ over which coherence is estimated.

The model expression obtained in the down-looking geometry is presented in part 4.2, equation (4.33). This expression is very similar to the VCZ in its optical formulation in that it relates the coherence factor to the 2D Fourier transform of the intensity distribution across an incoherent source. It being understood that in the present case this incoherent source is the insonified seafloor (called 'seafloor equivalent source' in this document). Spatial coherence is therefore a function of the extent and distribution of intensity within the equivalent seafloor source. Extent and distribution of intensity within the equivalent seafloor source is a combination of seafloor scattering, sound absorption, sonar aperture, transmit signals and temporal windowing effects. It is difficult to extract general rules for the evolution of coherence as a function of these parameters, insofar as coherence is the result of multiple interactions between these parameters. By simplifying the model through the addition of hypotheses, it is nevertheless possible to highlight some influences:

- **First Case**: Assuming omnidirectionnal sensors, homogeneous flat bottom with constant index, and constant propagation losses, spatial coherence depends only on the size of the temporal window $[t_i, t_f]$ used to compute it and if $t_i < \frac{2d}{z}$ (d is depth, c is sound speed), coherence curve has a Bessel cardinal form (equation (4.45)).

- **Second Case**: Considering directional sensors (i.e. with a finite aperture) and, assuming homogeneous flat bottom with constant index, constant propagation losses, temporal window $[t_i, t_f]$ such as $t_i < \frac{2d}{z}$ and t_f large enough so that the contributing portion of the seafloor is limited by the directivity and not by the masking function, coherence is proportional to the autocorrelation of the sensor aperture, as predicted by the VCZ in its 'acoustic formulation' (equation (4.46)).

The model expression obtained in the side-looking geometry is presented in part 4.3, equation (4.79). In a way, the modelling equation obtained in the side-looking geometry (equation (4.79)) is equivalent to that obtained in the down-looking geometry (equation (4.45)), in that they both relate spatial coherence to a sum of intensity contributions on the seafloor. However, in the case of modelling in the

side-looking geometry, coherence and intensity distribution are no longer linked by a Fourier transform relationship as stated by the VCZ theorem. Using additional simplifying assumptions, it has been shown that:

- **Along-track coherence**: Assuming a null across-track spatial lag, directional sensors in the along-track direction (i.e. with a finite aperture), it has been shown that, along-track coherence follows the VCZ theorem in its 'acoustical formulation'. Thus a linear aperture would produce a triangular coherence function whose base is twice as large as the aperture.

- **Across-track coherence**: Assuming a null along-track spatial lag, it has been shown that across-track coherence depends on along-track aperture: the longer the aperture the wider the coherence. This is because, in the case of across-track displacement, it is the curvature of the wavefront within the directivity of the sensors that reduces coherence. Thus small physical apertures will produce very wide directivity lobes in which the differences in curvature of the wavefronts will reduce the level of coherence. On the contrary, large physical apertures will produce very narrow directivity lobes in which the differences in curvature of the wavefronts remain low and so maintain a high level of coherence. We also note that the coherence length in this direction tends to be greater than in the along-track direction.

- **Bi-dimensional coherence**: In the case of a Gaussian aperture, it was possible to compute the form of the 2D coherence, i.e. in the presence of an along-track and an across-track spatial lag (see equation (4.88)). The expression thus obtained is compatible with the results obtained in just one of the two dimensions (i.e. evaluating the expression at an along-track or across-track spatial lag equal to 0). However, there is one point in this model that we are unable to explain. Indeed, we noticed that in the presence of spatial lag in both dimensions, if across-track spatial lag increases, coherence decreases but tolerance to an along-track spatial lag seems to increase. This point will have to be studied in greater details.

In chapter 4, an analytical model of spatial coherence for down-looking and side looking geometries has been introduced and solved under very restrictive hypotheses. In chapter 5, a numerical analysis of coherence is proposed in order to relax some of these hypothesis. This numerical study is based on two methods. First, a numerical integration of the equations 4.31 was achieved for the down-looking geometry. In particular, modelling the scattering term using the Jackson model for muddy, sandy and gravelly sediment allowed us to show combined effect of directivity and seafloor

scattering capacity (see part 5.2.2). Similarly, we highlighted the combined influence of the time window $[t_i, t_f]$ over which coherence is estimated with respect to the directivity parameter (see part 5.2.3). The conclusion of these two analysis is common and is well described by the VCZ theorem in its 'optical formulation'. Insofar, as the time window, the scattering term and the directivity all contribute to define the size and intensity distribution of the seafloor equivalent source and therefore the coherence. So if one of these three parameters is more restrictive than the others (for example, a highly directional sensor) then it is this parameter that will determine the coherence length. On the other hand, a parameter that does not constrain the extent and does not modulate the energy distribution of the seafloor equivalent source (e.g. a large time window) will have no impact on the observed coherence.

The numerical resolution of the analytical model was satisfactory in the down-looking geometry, but in the side looking geometry, the geometric decorrelation phenomena not taken into account in the analytical model led us to propose a numerical modelling of the temporal signals from which the coherences are estimated. This numerical modelling of the signals, which is closer to the actual acquisition geometry, is the second point in the numerical study of coherence and was presented in the section 5.3. In the along-track direction, the coherence calculated on signals simulated for several Gaussian apertures confirmed the results of the analytical modelling, namely that coherence in the along-track direction is well described by the VCZ theorem. In the across track direction, we studied the evolution of coherence as a function of the position of the focal point and the sensor along-track aperture. This analysis showed that:

- in the absence of geometric corrections, coherence in the across-track direction is severely limited, whatever the position of the focal point and whatever the aperture of the sensors;
- after correcting for the footprint mismatch, the coherence levels are significantly improved whatever the aperture of the sensors, and especially when the angle of incidence is low. This highlights the importance of stretching at high incidence angles.
- after correcting for the footprint mismatch and stretching, we observe that, whatever the focal point, the coherence observed is greater in the case of the directional sensor. This is in line with the observation made in the analysis of the analytical model, where coherence losses in the across-track direction has been linked to the difference in curvature of the wavefronts in the directivity lobe of the transducer .

6.2 Future works

It is often said that a thesis leads to more questions than answers, and this was certainly the case for this work. There are different aspects of the development presented in this document that could be analysed in details in future works. We have grouped them into three categories: those relating to the improvement of the simulation tool, those relating to additional analyses and those dealing with the application to real data.

6.2.1 Improvement of the simulation tool

Simulation tool developed in this work suffers from a strong limitation: computation time. This calculation time is particularly affected by the number of scattering elements used to mesh the seafloor. In accordance with the literature, we have set the number of scatterers by an average scatterer density of 7.5 scatterers per wavelength. At a fixed density of scatterers, simulation at high frequencies can require large numbers of scatterers which is one of the reasons why signals were simulated at a fairly low frequency. Another parameter that can drastically increase the number of scatterers and therefore the calculation time is the aperture of the sensors. In the case of sensors with low directivity, the scattering elements that significantly contribute to the received signal are spread over a large area, which in turn increases the number of scatterers required for the simulation, leading us to limit ourselves to the simulation in the case of sensors with high directivity. Two areas of work can be pursued with the aim of reducing computation time. First, a study could be conducted to determine what minimum scatterer density is needed to produce fields with the appropriate properties depending on seafloor roughness and texture. It is possible that a density of 7.5 scatterers per wavelength is overestimated. The second concerns the computation method. The modelling of signals by the finite scatterer model lends itself well to parallel computing and GPU computing, which can drastically reduce the computing time required.

6.2.2 Additional analyses

First of all, additional support for the validity of the model developed in Chapter 4 could be provided by further analysis. That could be achieved using the simulation tool presented in Chapter 5. This independent numerical modelling should allow to make a comparison to the model. It as been done in the along track direction (see part 5.3.2) and a good matching was noticed but this work still has to be conducted

in the across-track direction. In addition, comparison with real data, provided we are able of correct geometric decorrelation (discussed in the next paragraph) should also provide additional support for the validity of the model.

A second step would be to extend the analysis to low-frequency SAS data. Indeed, broadband low frequency systems give rise to specific features whose impact on spatial coherence merits study. First of all, the broadband nature of the systems means that the directivity lobe varies as a function of frequency. Throughout this document, we have emphasised the close link between spatial coherence and the aperture of the directivity lobe. The impact of the bandwidth of the signal deserves to be studied. Still in connection with low-frequency systems, one point that should be studied is the impact of the penetration of the acoustic beam into the sediment and therefore the effect of volume reverberation on spatial coherence. In this work, we have assumed only a surface contribution to the acoustic field backscattered by the seabed (2D integral for the model in this Chapter 4, and horizontal distribution of scatterers for the simulation in this Chapter 5). However, low frequency signals can penetrate into the sediment and in such a case, the seafloor equivalent source and the reverberation are no longer surface-based but volume-based. Taking into account the volume of sediment requires an integration over the insonified volume with an absorption coefficient in the sediment. This point has been modelled and studied in [Brown, 2017] for the down looking geometry, which highlighted the influence of the time window and the attenuation coefficient in the sediment. Another assumption that has been made, and which is probably incorrect in the case of low-frequency sonar, is that the scattering elements do not interact with each other. It could be interesting to be able to model or to simulate this kind of interaction to evaluate its influence on spatial coherence. In the same way as is done to simulate the elastic response of objects [Williams et al., 2010], such a model would probably require Finite Element Method (FEM) or Boundary Element Method (BEM), to correctly simulate the complex interactions that the various diffusing elements may have with each other.

6.2.3 Application to real data

In this document, we have carried out a theoretical study of spatial coherence. Some concepts have been illustrated using real data acquired by CMRE's HRLFSAS system. However, these illustrations are limited to some concepts and, in particular, the study of spatial coherence after correction of geometric decorrelations has only been carried out on simulated signals for which the acquisition geometry is perfectly controlled.

The procedure for compensating for geometric decorrelations used in this work consists of: firstly to compensate for misregistration in order to match footprints around the focal point and then to compensate for stretching by expanding one of the two time signals in order to match this contributions within the resolution cell. The simplicity of such a procedure should not hide the difficulties of the implementation on real data. Indeed, these compensations depends on the a priori knowledge of the bathymetry. However, depending on the situation, this a priori information is not necessarily available or easy to obtain. In [Synnes et al., 2021], depending on the available information to compensate for geometric decorrelations, three situations that can be encountered in a repeat-pass context are defined:

- **Known baseline and common terrain model:** This is the case, for example, with SAR systems whose very precise navigation makes it possible to control the interferometric baseline and thus obtain a terrain model shared by both trajectories. This is also the case for sonar systems such as HRLFSAS, which have a vertical multi-element antenna that enables it to measure bathymetry.

- **Unknown baseline and individual terrain model:** This is the case, for example, with interferometric SAS systems which are able to generate a terrain model during each successive pass over a seafloor [Saebo et al., 2007]. The unknown factor in this situation is the difference in trajectories followed during successive pass that results on different estimates of the terrain model. To deal with its case, its necessary to match these estimates of the terrain model and then to map slant-range sonar data onto the bathymetry.

- **Unknown baseline and unknwon terrain model:** This is the case, for example, for non-interferometric repeat-pass SAS systems. In such a case, baseline and terrain model are unknown. A method for searching baseline and stretching parameters is proposed in [Cervenka, 2013] and consists of selecting from each signal the part of the frequency spectrum that shares common information about the seafloor.

Bibliography

[Inn, a] Innomar "quattro" sbp. https://www.innomar.com/products/multi-transducer/quattro-sbp. Accessed: 2024-02-05.

[Inn, b] Innomar "sixpack" sbp. https://www.innomar.com/products/multi-transducer/sixpack-sbp. Accessed: 2024-02-05.

[map,] Mappem-3d electromagnetic acquisition system. https://www.mappem-geophysics.com/technologies/tmappem3d. Accessed: 2024-02-05.

[Amate et al., 2005] Amate, M., Hétet, A., Guyonic, S., Legris, M., Bellec, R., Maussang, F., Chanussot, J., Cervenka, P., and Marchal, J. (2005). Buried mines detection and classification: advanced technologies and signal processing. *Europe Oceans 2005*, 1:153–159 Vol. 1.

[Andrews et al., 1999] Andrews, A., Ralston, J., and Tuley, M. (1999). Research of ground-penetrating radar for detection of mines and unexploded ordnance: Current status and research strategy. page 102.

[Barngrover et al., 2014] Barngrover, C., Kastner, R., and Belongie, S. (2014). Semisynthetic versus real-world sonar training data for the classification of mine-like objects. *IEEE Journal of Oceanic Engineering*, 40(1):48–56.

[Born et al., 1999] Born, M., Wolf, E., Bhatia, A. B., Clemmow, P. C., Gabor, D., Stokes, A. R., Taylor, A. M., Wayman, P. A., and Wilcock, W. L. (1999). *Principles of Optics: Electromagnetic Theory of Propagation, Interference and Diffraction of Light*. Cambridge University Press, 7 edition.

[Brown, 2017] Brown, D. C. (2017). *Modeling and Measurement of Spatial Coherence for Normal Incidence Seafloor Scattering*. PhD thesis, The Pennsylvania State University.

[Brown et al., 2020] Brown, D. C., Gerg, I. D., and Blanford, T. E. (2020). Interpolation kernels for synthetic aperture sonar along-track motion estimation. *IEEE Journal of Oceanic Engineering*, 45(4):1497–1505.

[Brown et al., 2017] Brown, D. C., Johnson, S. F., and Olson, D. R. (2017). A point-based scattering model for the incoherent component of the scattered field. *The Journal of the Acoustical Society of America*, 141(3):EL210–EL215.

[Bucaro et al., 2007] Bucaro, J., Houston, B., Saniga, M., Nelson, H., Yoder, T., Kraus, L., and Carin, L. (2007). Wide area detection and identification of underwater uxo using structural acoustic sensors. page 16.

[Callow, 2010] Callow, H. (2010). Comparison of sas processing strategies for crabbing collection geometries. pages 1 – 9.

[Carrara et al., 1995] Carrara, W. G., Goodman, R. S., and Majewski, R. M. (1995). Spotlight synthetic aperture radar : signal processing algorithms.

[Cervenka, 2013] Cervenka, P. (2013). Baseline decorrelation in acoustic tools for surveying the seafloor. *Proceedings of Meetings on Acoustics*, 17(1):070073.

[Coiras et al., 2008] Coiras, E., Groen, J., Evans, B., and Pinto, M. (2008). Automatic change detection for the monitoring of cluttered underwater areas.

[Cook and Brown, 2009] Cook, D. A. and Brown, D. C. (2009). Analysis of phase error effects on stripmap sas. *IEEE Journal of Oceanic Engineering*, 34(3):250–261.

[Cutrona, 1975] Cutrona, L. J. (1975). Comparison of sonar system performance achievable using synthetic-aperture techniques with the performance achievable by more conventional means. *The Journal of the Acoustical Society of America*, 58(2):336–348.

[Cutrona, 1977] Cutrona, L. J. (1977). Additional characteristics of synthetic-aperture sonar systems and a further comparison with nonsynthetic-aperture sonar systems. *The Journal of the Acoustical Society of America*, 61(5):1213–1217.

[Czipott and Iwanowski, 1997] Czipott, P. V. and Iwanowski, M. D. (1997). Magnetic sensor technology for detecting mines, UXO, and other concealed security threats. In Ishimoto, W., editor, *Terrorism and Counter-Terrorism Methods and Technologies*, volume 2933, pages 67 – 76. International Society for Optics and Photonics, SPIE.

[Déculot et al., 1994] Déculot, D., Lecroq, F., and Gérard, M. (1994). Diffusion acoustique par des coques cylindriques. etude des ondes axiales. *http://dx.doi.org/10.1051/jp4:19945182*, 04.

[Fediuk et al., 2022] Fediuk, A., Wunderlich, T., Wilken, D., and Rabbel, W. (2022). Ground penetrating radar measurements in shallow water environment; a case study. *Remote Sensing*, 14(15).

[Fink and Cardoso, 1984] Fink, M. and Cardoso, J. (1984). Diffraction effects in pulse-echo measurement. *IEEE Transactions on Sonics and Ultrasonics*, 31(4):313–329.

[Fioravanti et al., 2019] Fioravanti, S., Sapienza, A., Aglietti, F., Carta, A., Galletti, D., and Pailhas, Y. (2019). Modular design of a 2d transmitting array for an advanced low frequency synthetic aperture sonar. In *OCEANS 2019 - Marseille*, pages 1–8.

[Florin et al., 2003] Florin, F., Zeebroeck, F. V., Quidu, I., and Bouffant, N. L. (2003). Classification performances of mine hunting sonar : Theory, practical results and operational applications.

[Foulon et al., 2011] Foulon, M., Amate, M., Burlet, N., Penven, P., Cervenka, P., and Marchal, J. (2011). Experimentations and sonar development for buried objects detection and classification.

[Francois and Garrison, 1982a] Francois, R. E. and Garrison, G. R. (1982a). Sound absorption based on ocean measurements: Part I: Pure water and magnesium sulfate contributions. *The Journal of the Acoustical Society of America*, 72(3):896–907.

[Francois and Garrison, 1982b] Francois, R. E. and Garrison, G. R. (1982b). Sound absorption based on ocean measurements. Part II: Boric acid contribution and equation for total absorption. *The Journal of the Acoustical Society of America*, 72(6):1879–1890.

[Geiman et al., 2000] Geiman, B., Gauss, R., and Trahey, G. (2000). In vivo comparison of fundamental and harmonic lateral transmit beam shapes. In *2000 IEEE Ultrasonics Symposium. Proceedings. An International Symposium (Cat. No.00CH37121)*, volume 2, pages 1669–1675 vol.2.

[Gendron et al., 2009] Gendron, M., Lohrenz, M., and Dubberley, J. (2009). Automated change detection using synthetic aperture sonar imagery. In *OCEANS 2009*, pages 1–4.

[Gerry and Knight, 2004] Gerry, C. and Knight, P. (2004). *Introductory Quantum Optics*. Cambridge University Press.

[Gespa, 1987] Gespa, N. (1987). *La diffusion acoustique par des cibles élastiques de forme géométrique simple : théories et expériences*. CEDOCAR.

[Gilmour, 1978] Gilmour, G. (1978). Synthetic aperture side-looking sonar system. US patent n° 4088978.

[GmbH, 2009] GmbH, I. T. (2009). Parametric technology for high resolution sub-bottom profilingt. Technical report.

[Goodman, 1985] Goodman, J. W. (1985). *Statistical Optics*. John Wiley and Sons.

[Gradshteyn and Ryzhik, 2007] Gradshteyn, I. S. and Ryzhik, I. M. (2007). *Table of integrals, series, and products*. Elsevier/Academic Press, Amsterdam, seventh edition. Translated from the Russian, Translation edited and with a preface by Alan Jeffrey and Daniel Zwillinger, With one CD-ROM (Windows, Macintosh and UNIX).

[Guerrero et al., 2021] Guerrero, Q., Salabarnada, A., Deu, A., and Devincenzi, M. J. (2021). Marine geophysical investigations for offshore wind farms and submarine interconnection cables.

[Haimovich et al., 2008] Haimovich, A. M., Blum, R. S., and Cimini, L. J. (2008). Mimo radar with widely separated antennas. *IEEE Signal Processing Magazine*, 25(1):116–129.

[Han et al., 2019] Han, S., Rong, X., Bian, L., Zhong, M., and Zhang, L. (2019). The application of magnetometers and electromagnetic induction sensors in uxo detection. *E3S Web of Conferences*, 131:01045.

[Hansen, 2011] Hansen, R. E. (2011). Introduction to synthetic aperture sonar. In Kolev, N. Z., editor, *Sonar Systems*, chapter 1. IntechOpen, Rijeka.

[Hansen et al., 2007] Hansen, R. E., Callow, H. J., and Sæbø, T. O. (2007). The effect of sound velocity variations on synthetic aperture sonar. *Proceedings of Underwater Acoustic Measurments 2007*.

[Hansen et al., 2014] Hansen, R. E., Lyons, A. P., Sæbø, T. O., Callow, H. J., and Cook, D. A. (2014). The effect of internal wave-related features on synthetic aperture sonar. *IEEE Journal of Oceanic Engineering*, 40(3):621–631.

[Hetet, 2003] Hetet, A. (2003). *Contribution à la detection de mines enfouies dans le sediment marin par synthèse d'ouverture basse fréquence*. PhD thesis, Université Paris 6.

[Hetet et al., 2004] Hetet, A., Amate, M., Zerr, B., Legris, M., Bellec, R., Sabel, J., and Groen, J. (2004). Sas processing results for the detection of buried objects with a ship mounted sonar. *ECUA*.

[Hunter et al.,] Hunter, A., Rymansaib, Z., Thomas, B., Burt, A., and Brothers, R. solation of resonant wave features in low-frequency wideband sas data products from cylindrical shell. In *synthetic aperture in sonar and radar conference*. Institute of Acoustics.

[Hunter et al., 2012] Hunter, A., Vossen, R., Quesson, B., Colin, M., Zampolli, M., and Beckers, A. (2012). Low frequency synthetic aperture sonar for detecting and classifying buried objects. *Proceedings of the 11th European Conference on Underwater Acoustics-ECUA 2012, 2-6 July 2012, Edinburgh, UK*, 34.

[Jackson et al., 1986] Jackson, D. R., Winebrenner, D. P., and Ishimaru, A. (1986). Application of the composite roughness model to high-frequency bottom backscattering. *The Journal of the Acoustical Society of America*, 79(5):1410–1422.

[Ji et al., 2019] Ji, X., Zhou, L., and Cong, W. (2019). Effect of incorrect sound velocity on synthetic aperture sonar resolution. *MATEC Web of Conferences*, 283:04013.

[Knox et al., 2010] Knox, W. H., Alonso, M., and Wolf, E. (2010). Spatial coherence from ducks. *Physics Today*, 63(3):11–11.

[Kopp, 2004] Kopp, L. (2004). Arrays trilogy: adaptive-parametric-synthetic. In *Processing Workshop Proceedings, 2004 Sensor Array and Multichannel Signal*, pages 59–67.

[Lamarche et al., 2011] Lamarche, G., Lurton, X., Verdier, A. L., and Augustin, J. M. (2011). Quantitative characterisation of seafloor substrate and bedforms using advanced processing of multibeam backscatter—application to cook strait, new zealand. *Continental Shelf Research*, 31.

[Leasko, 2012] Leasko, R. A. (2012). Munitions detection using unmanned underwater vehicles equipped with advances sensors - interim report. Technical report, Panama City.

[Lurton, 2002] Lurton, X. (2002). *An Introduction to Underwater Acoustics: Principles and Applications*. Geophysical Sciences Series. Springer.

[Mallart and Fink, 1991] Mallart, R. and Fink, M. (1991). The van cittert–zernike theorem in pulse echo measurements. *The Journal of the Acoustical Society of America*, 90(5):2718–2727.

[Mari et al., 2022] Mari, Z., Monteux, E., Hellouvry, Y.-H., Pibre, L., and Pasquet, J. (2022). Improving the realistic rendering of artificial sonar images using Cycle Generative Adversarial Networks. *Proceedings of Meetings on Acoustics*, 47(1):070010.

[Merlin et al., 2011] Merlin, W., Mouland, D., Markuske, W., King, P., Lewis, R., Walker, D., and Dinn, G. (2011). High resolution seabed sub-bottom profiler for auv. volume 6.

[Midtgaard et al., 2011] Midtgaard, O., Hansen, R. E., Sæbø, T. O., Myers, V., Dubberley, J. R., and Quidu, I. (2011). Change detection using synthetic aperture sonar: Preliminary results from the larvik trial. In *OCEANS'11 MTS/IEEE KONA*, pages 1–8.

[Miranda de Sá et al., 2009] Miranda de Sá, A. M. F., Ferreira, D. D., Dias, E. W., Mendes, E. M., and Felix, L. B. (2009). Coherence estimate between a random and a periodic signal: Bias, variance, analytical critical values, and normalizing transforms. *Journal of the Franklin Institute*, 346(9):841–853.

[Mopin et al., 2016] Mopin, I., Demoulin, X., Legris, M., Zerr, B., and Bourdon, R. (2016). Inversion géoacoustique des premiers mètres du sous-sol sous-marin et détection d'objets enfouis par AUV. In *13e Congrès Français d'Acoustique*, Le Mans, France.

[Munschy et al., 2007] Munschy, M., Boulanger, D., Ulrich, P., and Bouiflane, M. (2007). Magnetic mapping for the detection and characterization of uxo: Use of multi-sensor fluxgate 3-axis magnetometers and methods of interpretation. *Journal of Applied Geophysics*, 61(3):168–183. State-of-the-Art UXO Detection and Characterization.

[Myers et al., 2017] Myers, V., Groen, J., Schmaljohann, H., Quidu, I., and Zerr, B. (2017). Multi-look processing for coherent change detection with synthetic aperture sonar.

[Myers and Pinto, 2007] Myers, V. and Pinto, M. (2007). Bounding the performance of sidescan sonar automatic target recognition algorithms using information theory. *IET Radar, Sonar and Navigation*, 1:266 – 273.

[Myers et al., 2013] Myers, V., Quidu, I., Saebo, T., and Hansen, R. (2013). Results and analysis of coherent change detection experiments using repeat-pass synthetic aperture sonar images.

[Nakamura et al., 2004] Nakamura, Y., Yamaguchi, I., Tanaka, T., and Hama, Y. (2004). Buried object detection with synthetic aperture sonar. *Proceedings of the 2004 International Symposium on Underwater Technology (IEEE Cat. No.04EX869)*, pages 27–31.

[Neupane and Seok, 2020] Neupane, D. and Seok, J. (2020). A review on deep learning-based approaches for automatic sonar target recognition. *Electronics*, 9(11).

[Nicolas et al., 2019] Nicolas, F., Arnold-Bos, A., Quidu, I., and Zerr, B. (2019). Symbolic simultaneous registration and change detection between two detection sets in the mine warfare context. In *OCEANS 2019 - Marseille*, pages 1–10.

[Nicq, 1998] Nicq, G. (1998). *Contribution à l'étude des critères de classification acoustique basse fréquence des cibles sous marines déposées sur le fond marin ou enfouies dans le sédiment*. PhD thesis, Université de Bretagne Occidentale.

[Nicq and Brussieux, 1998] Nicq, G. and Brussieux, M. (1998). A time-frequency method for classifying objects at low frequencies. In *IEEE Oceanic Engineering Society. OCEANS'98. Conference Proceedings (Cat. No.98CH36259)*, volume 1, pages 148–152 vol.1.

[Pailhas et al., 2017] Pailhas, Y., Petillot, Y., Brown, K., and Mulgrew, B. (2017). Spatially distributed mimo sonar systems: Principles and capabilities. *IEEE Journal of Oceanic Engineering*, 42(3):738–751.

[Pinto et al., 2002] Pinto, M., Bellettini, A., Hollett, R., and Tesei, A. (2002). Real- and synthetic-array signal processing of buried targets. *Oceanic Engineering, IEEE Journal of*, 27:484 – 494.

[Pinto et al., 2004] Pinto, M., Bellettini, A., Wang, L., Monk, P., Myers, V., and Pautet, L. (2004). A new synthetic aperture sonar design with multipath mitigation. volume 728, pages 489–496.

[Pinto et al., 1997] Pinto, M., Fohanno, F., Tremois, O., and Guyonnic, S. (1997). Autofocusing of synthetic aperture sonar using temporal and spatial coherence of seafloor reverberation. *SACLANTCEN Conference Proceeding Series*, CP-45.

[Plantevin, 2017] Plantevin, P. (2017). The seachirp3d -presentation. *Soacsy*.

[Pouliquen et al., 1999] Pouliquen, E., Bergem, O., and Pace, N. G. (1999). Time-evolution modeling of seafloor scatter. I. Concept. *The Journal of the Acoustical Society of America*, 105(6):3136–3141.

[Quidu, 2012] Quidu, I. (2012). Incoherent change detection using amplitude sidescan sonar images. *Proceedings of Meetings on Acoustics*, 17(1):070020.

[Quidu et al., 2012] Quidu, I., Myers, V., Midtgaard, O., and Hansen, R. (2012). Sub-pixel image registration for coherent change detection between two high resolution sonar passes.

[Richard, 2022] Richard, G. J. (2022). *Explicabilité des algorithmes de classification des images SAS en guerre des mines*. PhD thesis, Ecole nationale supérieure Mines-Télécom Atlantique Bretagne Pays de la Loire.

[Roed et al., 2020] Roed, E. S., Andersen, K. K., Bring, M., Tichy, F., Åsjord, E.-M., and Hoff, L. (2020). Increased usable frequency band for underwater transducers with single crystal. In *2020 IEEE International Ultrasonics Symposium (IUS)*, pages 1–4.

[Sabatini et al., 2022] Sabatini, R., Pailhas, Y., Cristini, P., and Xenaki, A. (2022). Numerical modeling of low-frequency scattering from targets buried under rough seafloors. *The Journal of the Acoustical Society of America*, 152(4 Supplement):A119–A119.

[Saebo et al., 2007] Saebo, T. O., Hansen, R. E., and Hanssen, A. (2007). Relative height estimation by cross-correlating ground-range synthetic aperture sonar images. *IEEE Journal of Oceanic Engineering*, 32(4):971–982.

[Salem et al., 2005] Salem, A., Hamada, T., Kiyoshi, J., and K., U. (2005). Detection of unexploded ordnance (uxo) using marine magnetic gradiometer data. *Exploration Geophysics*, 36(1):97–103.

[Schreiber et al., 2016] Schreiber, E., Peichl, M., Heinzel, A., Dill, S., Bischeltsrieder, F., Anger, S., Kempf, T., and Jirousek, M. (2016). Challenges for operational use of

ground-based high-resolution sar for landmines and uxo detection. In *Proceedings of EUSAR 2016: 11th European Conference on Synthetic Aperture Radar*, pages 1–4.

[Sessarego et al., 1997] Sessarego, J.-P., Sageloli, J., Gazanhes, C., and Uberall, H. (1997). Two Scholte–Stoneley waves on doubly fluid-loaded plates and shells. *The Journal of the Acoustical Society of America*, 101(1):135–142.

[Spiess and Anderson, 1983] Spiess, F. and Anderson, V. (1983). Wide swath precision echo sounder. US patent n° 4400803.

[Synnes et al., 2021] Synnes, S. A. V., Hansen, R. E., and Sæbø, T. O. (2021). Spatial coherence of speckle for repeat-pass synthetic aperture sonar micronavigation. *IEEE Journal of Oceanic Engineering*, 46(4):1330–1345.

[Talmant et al., 1988] Talmant, M., Quentin, G., Rousselot, J. L., Subrahmanyam, J. V., and Überall, H. (1988). Acoustic resonances of thin cylindrical shells and the resonance scattering theory. *The Journal of the Acoustical Society of America*, 84(2):681–688.

[Tanaka et al., 2003] Tanaka, T., Hama, Y., Shiba, H., and Yamaguchi, I. (2003). Low-frequency synthetic aperture sonar system. *Japanese Journal of Applied Physics*, 42(5S):3225.

[Tesei et al., 2002] Tesei, A., Maguer, A., Fox, W., Lim, R., and Schmidt, H. (2002). Measurements and modeling of acoustic scattering from partially and completely buried spherical shells. *The Journal of the Acoustical Society of America*, 112:1817–30.

[Thomas and Hunter, 2022] Thomas, B. and Hunter, A. (2022). Coherence-induced bias reduction in synthetic aperture sonar along-track micronavigation. *IEEE Journal of Oceanic Engineering*, 47(1):162–178.

[Van Cittert, 1934] Van Cittert, P. A. (1934). "die wahrscheinliche schwingungsverteilung in einer von einer lichtquelle direkt oder mittels einer linse beleuchteten ebene" ("the probability distribution of vibrations in a plane illuminated by a light source directly or through a lens"). *Physics*, 1(1):201–2010.

[Walsh, 1969] Walsh, G. (1969). Acoustic mapping apparatus. US patent n° 3484737.

[Williams, 2016] Williams, D. P. (2016). Underwater target classification in synthetic aperture sonar imagery using deep convolutional neural networks. In *2016 23rd International Conference on Pattern Recognition (ICPR)*, pages 2497–2502.

[Williams et al., 2010] Williams, K. L., Kargl, S. G., Thorsos, E. I., Burnett, D. S., Lopes, J. L., Zampolli, M., and Marston, P. L. (2010). Acoustic scattering from a solid aluminum cylinder in contact with a sand sediment: Measurements, modeling, and interpretation. *The Journal of the Acoustical Society of America*, 127(6):3356–3371.

[Winter et al., 2020] Winter, R. G., Steinberg, A. M., and Attwood, D. (2020). Coherence. *AccessScience*.

[Winton, 2023] Winton, T. (2023). Application of parametric sub-bottom profilers for responsible in situ management of underwater shallow-buried archaeological materials. pages 188–208.

[Wolf and Born, 1955] Wolf, E. and Born, M. (1955). A macroscopic theory of interference and diffraction of light from finite sources ii. fields with a spectral range of arbitrary width. *Proceedings of the Royal Society of London. Series A. Mathematical and Physical Sciences*, 230(1181):246–265.

[Xenaki et al., 2022] Xenaki, A., Gips, B., and Pailhas, Y. (2022). Unsupervised learning of platform motion in synthetic aperture sonar. *The Journal of the Acoustical Society of America*, 151(2):1104–1114.

[Zampolli et al., 2007] Zampolli, M., Tesei, A., Jensen, F. B., Malm, N., and Blottman, J. B. (2007). A computationally efficient finite element model with perfectly matched layers applied to scattering from axially symmetric objects. *The Journal of the Acoustical Society of America*, 122(3):1472–1485.

[Zernike, 1938] Zernike, F. (1938). The concept of degree of coherence and its application to optical problems. *Physics*, 5(8):785–795.

[Zerr et al., 1999] Zerr, B., Tesei, A., Maguer, A., Fox, W. L. J., and Fawcett, J. A. (1999). A classification technique combining aspect dependence and elastic properties of target scattering. *SACLANTCEN Report*, SR-310.

Titre : Contributions à l'étude de la cohérence spatiale bi-dimensionnelle dans le cadre du développement d'un sonar à ouverture synthétique basse fréquence.

Mots clés : Réverbération – Cohérence Spatiale – Sonar à ouverture synthétique basses fréquences.

Résumé : Appliquée pour la première fois à la lumière, la notion de cohérence spatiale exprime le degré de corrélation entre deux signaux acquis en deux points de l'espace. Dans le domaine sonar, la cohérence spatiale est un concept central qui affecte la résolution spatiale des systèmes ainsi que les performances de procédés tels que l'interférométrie et la synthèse d'ouverture. La configuration du système sonar, les paramètres de traitement du signal, et les perturbations externes telles que des conditions environnementales changeantes affectent la cohérence spatiale. Dans le domaine de la lutte contre les mines, des sonars à ouverture synthétique basse fréquence sont en cours de développement en particulier afin de permettre la détection d'objets enfouis. L'objectif de cette thèse est de développer une modélisation analytique de la cohérence spatiale de tels systèmes. Pour cela, des modèles existants développés pour la géométrie d'acquisition verticale ont été étendus pour être compatibles d'une acquisition latérale. Cependant, en géométrie latérale, des décorrélations géométriques non prises en compte dans le modèle réduisent le niveau de cohérence. Pour cela, une modélisation numérique des signaux est proposée afin d'étudier l'influence de ces dernières et d'estimer les niveaux de cohérence après compensation des phénomènes de décorrélation géométriques.

Title: Contributions to the study of two-dimensional spatial coherence as part of the development of a low-frequency synthetic aperture sonar.

Keywords: Reverberation – Spatial Coherence – Low Frequency Synthetic Aperture Sonar.

Abstract: First applied to light, the notion of spatial coherence is related to the degree of correlation between two signals acquired at two points in space. In the field of sonar, spatial coherence is a central concept that affects the spatial resolution of systems as well as the performance of processes such as interferometry and aperture synthesis. The configuration of the sonar system, the signal processing parameters, and external disturbances such as changing environmental conditions all affect spatial coherence. In the field of mine countermeasures, low-frequency synthetic aperture sonars are currently being developed, in particular to detect buried objects. The aim of this thesis is to develop an analytical model of the spatial coherence of such systems. To this end, existing models developed for vertical acquisition geometry have been extended to be compatible with lateral acquisition. However, in lateral geometry, geometric decorrelations not taken into account in the model reduce the level of coherence. For this reason, numerical modelling of the signals is proposed in order to study the influence of these decorrelations and to estimate the coherence levels after compensation for the geometric decorrelation phenomena.